UNIVERSITY OF SOUTHAMPTON

SCHOOL OF ELECTRONICS AND COMPUTER SCIENCE

Integration of spintronics into silicon microelectronics

Michail E. Kiziroglou

Thesis for the degree of Doctor of Philosophy

October 2006

To my parents Triantafyllia and Efthimis
and to my sister Venia

UNIVERSITY OF SOUTHAMPTON

ABSTRACT

SCHOOL OF ELECTRONICS AND COMPUTER SCIENCE

Doctor of Philosophy

INTEGRATION OF SPINTRONICS INTO SILICON MICROELECTRONICS

by Michail Kiziroglou

Thesis Abstract

Practical application of spin-electronics and nanotechnology depends largely on compatibility with conventional technology. The work presented in this thesis is on the integration of spintronic devices and nano-fabrication with silicon. A review of spintronics is presented and the importance of semiconductors to this field is highlighted. A metallisation technique for silicon of different resistivities is developed using electrodeposition. No seed layer is required and a back-contact is not essential. Selective electrodeposition on patterned Si/SiO_2 is achieved demonstrating compatibility with microelectronics processes. The film growth modes are studied and a correlation among the electrochemical conditions, the roughness and the magnetic properties of the film is established.

Latex sphere self-assembly is used for the fabrication of inverse sphere magnetic arrays electrodeposited directly on Si. Lithographic patterns on Si guide the self-assembly along particular directions and improve the long-range order. Size commensurability between the pattern and the spheres is critical for the long range ordering of the spheres. Non-commensurate guiding results in reproducible periodic triangular distortion of the close packed self-assembly. The alignment of self-assembly arrays on both sides of a guiding line is achieved. This technique is promising for applications such as patterned recording media and Si-integrated magnetoresistance devices but also for photonic applications such as waveguides and photonic crystals.

The Schottky Barrier (SB) at magnetic metal - semiconductor interfaces are of particular importance for spin injection and detection and for suppressing substrate leakage currents at magnetoresistance devices grown directly on semiconductors. Physical and electrical characterisation of the SB at electrodeposited Ni - lowly doped Si contacts is performed. A high quality rectifying behaviour is observed. The results are explained using modern SB models. The Ni-Si SB is used to suppress leakage currents and allow anisotropic magnetoresistance measurements in self-assembled magnetic anti-sphere arrays directly on Si.

Highly doped Si is used to enable tunnelling currents in SBs. The characterisation results are interpreted using tunnelling theory for SB. It is shown that under certain bias conditions tunnelling is the dominant mechanism for both forward and reverse bias. An exponential reverse bias $I - V$ behaviour with negative temperature coefficient is reported. An explanation can be found in the rapid decrease of the reverse bias $I - V$ slope with temperature predicted by Padovani and Stratton for thermionic field emission in conjunction with the increase of the SB height with temperature suggested for spatially distributed barrier heights. These results reveal the high potential of SBs for spin-injection and detection in active spintronic devices.

Contents

List of Publications

Journal Papers

Electrodeposition of Ni-Si Schottky barriers

M. E. Kiziroglou, A. A. Zhukov, M. Abdelsalam, X. Li, P. A. J. de Groot, P. N. Bartlett, and C. H. de Groot. IEEE Trans. Magn. 41, no. 10, 2639-2641, 2005.

Shape induced anisotropy in anti-dot arrays from self-assembled templates.

A. A. Zhukov, M. E. Kiziroglou, A. V. Goncharov, R. Boardman, M. A. Ghanem, M.Abdelsalam, V. Novosad, G. Karapetrov, X. Li, H. Fangohr, C. H. de Groot, P. N. Bartlett, P. A. J. de Groot. IEEE Trans. Magn. 71, no. 10, 3598-3600, 2005.

Catalyst free low temperature carbon nanotube growth on SiGe islands

T. Uchino, K. N. Bourdakos, C. H. de Groot, P. Ashburn, M. E. Kiziroglou, G. D. Dilliway, and D. C. Smith. App. Phys. Lett. 86, 233110, 2005.

Analysis of thermionic emission from electrodeposited Ni-Si Schottky barriers.

M. E. Kiziroglou, A. A. Zhukov, X. Li, D. C. Gonzalez, P. A. J. de Groot, P. N. Bartlett and C. H. de Groot. Sol. St. Comm. 140, 508-513, 2006

Orientation and symmetry control of inverse sphere magnetic nano arrays by guided self-assembly.

M. E. Kiziroglou, A. A. Zhukov, X. Li, D. C. Gonzalez, P. A. J. de Groot, P. N. Bartlett and C. H. de Groot. J. Appl. Phys. 100, 113720, 2006

Long range ordering in self-assembled Ni arrays on patterned Si.

D. C. Gonzalez, M. E. Kiziroglou, X. Li, A. A. Zhukov, H. Fangohr, P. A. J. de Groot, P. N. Bartlett and C. H. de Groot. J. of Magn. Magn. Mat. Accepted.

Germanium catalyst for growth of high quality single walled carbon nanotubes. T. Uchino, K. N. Bourdakos, S. Wang, C. H. de Groot, P. Ashburn, M. E. Kiziroglou and D. C. Smith., J. of Nanotechnology. Submitted.

Thermionic field emission at Ni-Si contacts for spin injection
M. E. Kiziroglou, X. Li, M. K. Husain, A. A. Zhukov, P. A. J. de Groot and C. H. de Groot. To be submitted to Phys. Rev. B.

Oral Presentations At Conferences

Electrodeposition of Ni-Si Schottky barriers
M. E. Kiziroglou, A. A. Zhukov, M. Abdelsalam, X. Li, P. A. J. de Groot, P. N. Bartlett, and C. H. de Groot. IEEE International Magnetics Conference (INTERMAG) 2005.

Transport mechanisms at Ni-Si Schottky barriers for spin injection
M. E. Kiziroglou. Film Deposition and the Control of Interfaces for Spintronics. Institute of Physics, London, 2006.

Transport mechanisms at Ni-Si Schottky barriers for spin injection
M. E. Kiziroglou, A. A. Zhukov, X. Li, D. C. Gonzalez, P. N. Bartlett, P. A. J. de Groot and C. H. de Groot. IEEE International Magnetics Conference (INTERMAG) 2006.

Preface

The work presented in this Ph.D. thesis is the outcome of adventurous research carried out in the inspiring working environment of the Nanoscale System Integration (NSI) research group, School of Electronics and Computer Science (ECS), University of Southampton.

A real shadow in this Ph.D. study was a destructive fire at the cleanroom facilities of ECS, in October 2005. All the fabricated devices and prepared substrates were destroyed, apart from a few samples. Books, notes and half of the hard-drive stored data were restored and made available no sooner than 2 and a half months after the fire. Although a scholastic organisation of the Ph.D. work made the retrieval of all the research results possible (redundant data copies, consistent recording and regular reports), the personal time wasted due to the fire is estimated to have been more than 3 months.

I would like to thank the School of Electronics and Computer Science of the University of Southampton for the full financial support throughout my Ph.D. studies.

I would like to express my deepest gratitude to my supervisor Dr. Kees de Groot for his excellent guidance. His encouragement and trust enabled me to give my best to this Ph.D. Despite his busy schedule he always had time to discuss my questions and he was very patient with my weaknesses and my, sometimes over-the-top research ideas. He managed to keep me highly motivated even after disheartening events such as the fire. Besides the excellent research opportunities, he taught me to look at science with ambition, reason and method. I would like to thank Dr. Kees de Groot for all the above and also for his full support regarding my post doctorate plans.

I owe a big thanks to all the staff and students of NSI for the excellent working atmosphere, the support and the social activities we shared and the personnel of the cleanroom facility for the training and advices they provided. Special thanks to my close colleagues Xiaoli Li and David Gonzalez and to Prof. Peter de Groot and Prof. Philip Bartlett for all their help and contribution to the publications related to this Ph.D. work. Also, special thanks to Dr. Takashi Uchino for invaluable suggestions and guidance and to Prof. Peter Ashburn for his positive assessments through this Ph.D.

I would especially like to thank Dr. Alexander Zhukov for his teaching and guidance and for the fruitful discussions and educative disagreements.

Huge thanks to my beloved parents and sister for their unreserved support, encouragement, patience and understanding during these three years. I am also grateful to the new friends I have made here and to my girlfriend Korina Katsaliaki for the fantastic nights-out, the unforgettable trips and the great, unspeakable times we shared. I wouldn't be able to carry out this work without their support and I deeply believe that they are the most precious outcome of my stay in Southampton.

List of Symbols

Symbol	Description	Unit
A	Richardson constant	$A\ m^{-2}\ K^{-2}$
C	Capacitance	F
D	Diffusion Coefficient	m^2/s
d	Density	Kg/m^3
F	Faraday constant	$C/mole$
H	Magnetic field	A/m
I	Current	A
J	Current density	A/m^2
k	Boltzmann constant	J/K
M	Magnetisation	$A\ m^2$
N	Doping concentration	m^{-3}
Q	Charge	C
q	Elementary charge	C
R	Resistance	Ω
r	Sphere radius	m
T	Absolute temperature	L
V	Voltage	V
W	Depletion region width	m
ϵ	Permitivity	F/m
η	Electrochemical overpotential	V
ρ	Resistivity	$\Omega\ m$
ϕ	Potential	V

Chapter 1

Introduction

As information becomes more and more important in modern times, Information Technology (IT) continues to play the primal role in the worldwide economic and social development. The demand for larger information processing, transport and storage capability dictated by the Information Society, drives an enormous scale research and development on the optimisation of the fundamental processing unit (transistor) and storage unit (memory bit).

It has been recognised that as transistors and memory cells go down in size to allow higher density of information processing and storage, quantum mechanical effects emerge, requiring the revision of their working principle and architecture. Therefore, the actual challenge in assuring the continuation of IT development can be split into two separate questions. Firstly, a flexible and commercially viable technique of fabrication on the scale of a nanometre needs to be developed. Secondly, the function of transistors and memory cells/media must be re-designed in a quantum fashion in order to use quantum effects for functional benefit instead of suppressing them.

1.1 Spintronics

The study and exploitation of the spin degree of freedom of electrons along with their charge to build useful devices constitutes the field of spintronics. By convention, traditional magnetic devices such as hard disc drives may also be considered as part of spintronics. Spin-dependent electronic transport through magnetic metals, called

magnetoresistance, has attracted a vast amount of attention leading to a variety of spin devices. Such devices are already been used as magnetic sensors and magnetic recording heads with great commercial success [1].

The introduction of semiconductors in spintronics is of particular interest as it would imply compatibility with conventional electronics and introduction of non-linear effects which are essential for active devices. The generation, preservation, modulation and detection of spin polarised current in non-magnetic semiconductors are very important milestones towards this goal.

1.2 Objective and outline

In the above context, this Ph.D. work focuses on two main objectives:

- To combine self-assembly and conventional lithography techniques for the fabrication of patterned magnetic recording media.
- To develop and characterise magnetic metal-semiconductor contacts for spin injection and detection.

To set a foundation in achieving these goals, the literature in spintronics was studied with a special view on recording media, magnetic random access memories and spin transistors. A general review of spintronics is presented in chapter 2, marking the advantages of introducing silicon to spintronics.

A Ni electrodeposition process was developed for Si of low and high resistivity. Electrodeposition was chosen because, in contrast with sputtering or evaporation, it is not a line of sight technique, allowing the fabrication of 3-D structured inverse sphere arrays (see chapter 4). A manual setup was built, the growth modes were investigated and the process was optimised for minimum film surface roughness. Moreover, the magnetic properties of the Ni film were studied. The results of this work are presented in chapter 3.

The combination of conventional lithography with latex sphere self-assembly was studied. The significance of the shape and size of the guiding patterns was recognized and a special purpose lithographic mask was designed. Size commensurability

between the patterns and the spheres and long-range effects were investigated. Ni electrodeposition through the latex sphere assembly was performed leading to inverse sphere magnetic arrays on Si. The results of this work are presented in chapter 4.

Electrodeposited Ni-Si contacts with lowly doped Si were fabricated and the Schottky barrier was characterised using modern models of the thermionic emission theory. The results were compared with, evaporated Ni-Si contacts prepared at the same time. Physical characterisation of the Ni layer was performed to complement the electrical results. The rectifying behaviour of Ni-Si contacts with lowly doped Si was used to suppress substrate leakage currents and perform magnetoresistance measurements on Ni inverse sphere arrays fabricated by guided self assembly as described above. The results of this work are presented in chapter 5.

Electrodeposited Ni-Si Schottky barriers using highly doped Si were also fabricated to enable tunnelling effects and study their potential for spin injection and detection applications. The results were analysed using the theory of tunnelling for Schottky barriers, taking into account the results of the thermionic emission characterisation for Ni-Si contacts with lowly doped Si. This work is presented in chapter 6.

A summary of the results that are presented in this Ph.D. thesis is given in Chapter 7. Appendix A presents a detailed theoretical analysis of the uniformity of the potential in Si electrodes during electrodeposition. Appendix B gives a general description of the lithography masks used.

The work outlined above is novel and as such, most of it has or is in the process of being published in highly reputable peer-reviewed journal papers and presented at international conferences. A list of publications that came out of this Ph.D. work is given at the beginning of this manuscript.

Chapter 2

Spintronics

2.1 Introduction

Magnetism as a property of matter has been recognised to be one of the two fundamental principles in building systems for transmitting, processing and storing information and also for energy transformation. Along with electricity, it has been used for most of the modern technology achievements: from television to cellular phones and from sensors to high density data storage media.

Early processing systems in particular used mainly electrical and electronic circuits rather than magnetic ones. After the invention of the first transistor in 1947, electronics dominated completely in the field of information processing while magnetism started to consolidate its principal role in information storage systems. A revolution of scaling in dimensions followed, feeding the increasing demands of the information community. Ultra high information storage densities ($\sim$1Gbit/inch^2) have been achieved on magnetic materials and extremely high clock frequencies ($\sim$3GHz) are used in modern information processors.

Lately, the traditional discrete roles of electronics and magnetism for information processing and storage have started to fade away. Magnetic devices as potential alternatives to conventional transistors have been proposed while magnetic floppy disks have already been replaced by chip-memories (e.g. EPROM). Optoelectronic applications, which were restricted in the past to power transformation (solar cells) and

information storage (compact discs) applications, have been expanded to information transmission and processing.

While electronic devices take advantage of the electron charge, spintronic devices exploit the electron spin along with its charge, introducing non-volatility and the potential for more speed, larger space density and less power consumption. Spintronics has increasingly been attracting the interest of the scientific community. The most reputable universities and research and development companies in Europe, USA and Japan have created individual research groups for spintronics and large investments have been made in this new field [2]. Reviews of the advances in spintronics can be found in the literature [1–6].

As with any alternative technology in electronics, the viability of spintronic devices depends on scalability and compatibility with the current technology. Therefore, the integration of spintronic devices with silicon is of special interest and constitutes the main motivation of this research work. Before proceeding to the original research results, the effect of magnetoresistance and the main spintronic applications with their associated working principles are reviewed.

2.2 Magnetoresistance

Modern spintronics research work is focused on the spin dependence of electron transport through magnetic and non-magnetic materials and multilayers. A suitable combination of ferromagnetic metals can drastically affect the electron current transported through them. This effect is known in the literature as spin-dependent electron transport or as magnetoresistance. Depending on the particular medium and physical orientation of the conducting materials there are several different types of magnetoresistance including Anisotropic MagnetoResistance (AMR), Giant MagnetoResistance (GMR), Tunnel MagnetoResistance (TMR) and Domain Wall MagnetoResistance (DW-MR).

2.2.1 Anisotropic Magnetoresistance

The earliest observed magnetoresistance effect is AMR [7]. The resistance in ferromagnets varies with $cos^2\theta$ where θ is the angle between the direction of the magnetic moment of the ferromagnet and the direction of the current flow. By changing the magnetisation by an external magnetic field, one can control its resistance. If $R_{\parallel}$ and $R_{\perp}$ are the saturation resistances for magnetisation parallel and perpendicular to the current flow respectively, the AMR ratio can be defined as:

$$AMR = 2 \cdot \frac{R_{\parallel} - R_{\perp}}{R_{\parallel} + R_{\perp}} \tag{2.1}$$

AMR is a consequence of bulk scattering of conduction electrons by spin-orbit interactions. As a result, it decreases with the ferromagnetic film thickness because of the increasing significance of surface scattering [8]. This is one of the most important drawbacks for AMR as it prevents large AMR phenomena from appearing in very small structures. The largest AMR has been achieved using Co, Ni and Fe alloys (7%) [7].

The main applications of AMR are magnetic read heads and sensors. Most of modern tape storage devices use AMR read sensors [9]. AMR read heads for hard disk drives have also been used in the past, but now this area is dominated by giant magnetoresistance.

Recent work on AMR is focused on isolating and observing this phenomenon in metal alloys [10, 11]. AMR has also been used in the investigation of magnetisation reversal processes of materials [12]. Advances in AMR sensors have been reported, but they are on the system level [13–15]. Lastly, some theoretical work towards modelling of specific, optimised AMR structures has been published recently [16].

2.2.2 Giant Magnetoresistance

Giant magnetoresistance was experimentally observed and explained in terms of spin-dependent scattering in 1988 [17, 18]. It is a quantum mechanical effect observed in layered magnetic thin-film structures that are composed of alternating layers of ferromagnetic and nonmagnetic layers. When the magnetic moments of the ferromagnetic

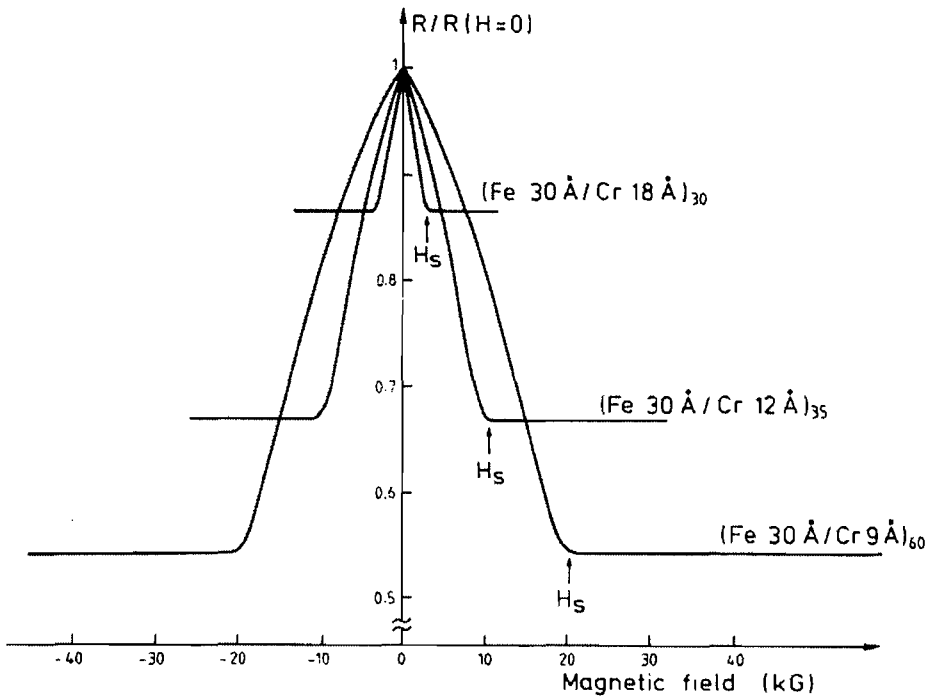

Figure 2.1: *Giant magnetoresistance of three Fe/Cr multilayers with different Cr thicknesses at 4.2 K (Baibich et al. [17]).*

layers are parallel, the spin-dependent scattering of the carriers is minimised and the material resistance is at its minimum. When the ferromagnetic layers are antiparallel, the spin-dependent scattering of the carriers is maximised and the resistance is at its maximum. The direction of the magnetic moment can be manipulated by an external magnetic field [19]. The change of the resistance between these two states is very big compared to AMR, justifying the term "Giant". An example of experimental magnetoresistance observation in Fe/Cr multilayers as published by Baibich et al [17] is shown in Fig. 2.1.

A simplified description of the GMR effect is illustrated in Fig. 2.2. When the two ferromagnetic layers are magnetized in parallel, half the electrons (in the case of Fig. 2.2 those with spin to the right) can flow through without much scattering. In the antiparallel case, all the electrons are scattered, either at the first or at the second layer, giving a high resistance. It is noted that the electron scattering is not as simple as shown in Fig. 2.2. It can be interfacial or bulk and theoretical studies on these effects can be found in the literature [20–22].

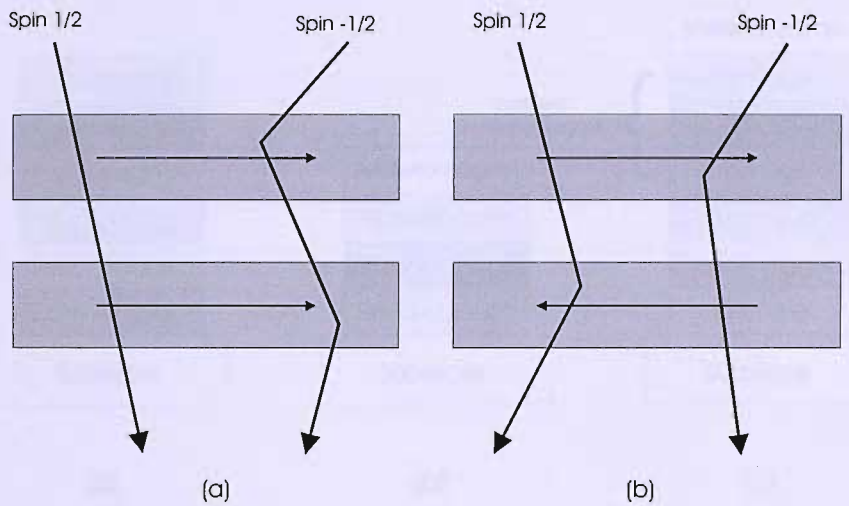

Figure 2.2: *Simplified description of the giant magnetoresistance effect: (a) parallel ferromagnetic layers. (b) antiparallel ferromagnetic layers.*

Giant magnetoresistance is measured as the ratio of the resistance change divided by the structure's resistance. If R_P and R_A are the resistances of a GMR structure in the parallel and the antiparallel states respectively, then the GMR ratio for that structure will be given by:

$$GMR = \frac{R_A - R_P}{R_A} \tag{2.2}$$

Several different architectures have being developed to build devices which would take advantage of GMR. The various structures can be categorised according to whether the current is flowing in parallel or perpendicular to the interface between the layers. In the Current In Plane (CIP) geometry, the most commonly used structures are shown in Fig. 2.3.

The simple layer stack shown in Fig. 2.3a has been widely used, giving magnetoresistance ratios of 10% to 70% for applied fields of 100 to 1000 Oe [2, 23, 24]. The spin valve structure of 2.3b gives GMR ratios of 5% to 10% for much lower magnetic fields (10-30 Oe) [25]. The antiferromagnetic layer is pinning the neighbouring magnetic layer so that its magnetisation is relatively insensitive to external magnetic fields. Hence, one can change the relative magnetisation of the two ferromagnetic layers by applying a moderate magnetic field. An improved version of the spin valve

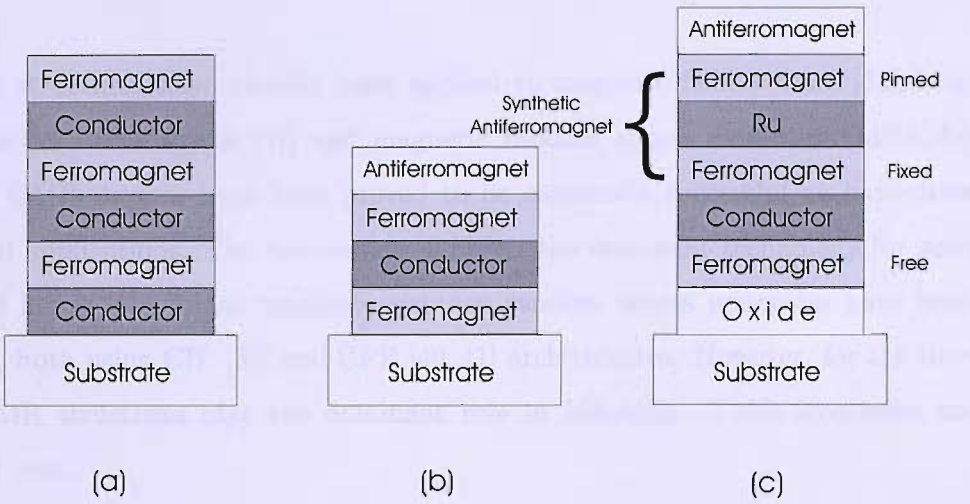

Figure 2.3: *Giant magnetoresistance structures: (a) simple multilayer, (b) spin valve, (c) spin valve with synthetic antiferromagnet and a nano oxide layer.*

introducing a synthetic antiferromagnetic layer (SAF) [26] and a nano-oxide layer [27] is illustrated in Fig. 2.3c. The upper ferromagnetic layer is pinned by the antiferromagnet. The ferromagnetic layers separated by the Ru layer are strongly antiparallel coupled and hence the middle ferromagnet is fixed. This improves the stability and the operation temperature of the device [2]. The nano-oxide layer is a specular layer made of an antiferromagnet such as NiO [27, 28]. It causes elastic scattering of the carriers at the interface, increasing the difference between the mean free paths of the up and down spin electrons. Devices implementing synthetic antiferromagnets and specular layers give double GMR ratios compared to the simple spin valve, for almost the same applied field (10-40 Oe) [2].

High GMR values have also being achieved by structures where the current flow is normal to the plane of the layers. This architecture is called Current Perpendicular to the Plane (CPP) [29, 30]. The theoretical analysis of these structures is simpler than the CIP ones [31] and they give higher GMR ratios. GMR improving techniques have also been applied in the CPP architectures [32, 33]. Today, the research on GMR optimization in general is focused on enlarging the GMR ratios with simultaneous reduction of the switching fields [34]. A large variety of techniques is used with GMR ratio achievements exceeding 110% at room temperature, under fields exceeding 20

kOe. [35].

GMR structures have already been applied to magnetic field sensors [36], read heads for hard disk drives [37] and magnetic random access memories (MRAMs) [19, 38]. GMR devices have been proved to be extremely successful as hard-drive read head applications. The last decade, GMR is the dominant technology for hard disc read heads [8]. Giant magnetoresistance random access memories have been reported, both using CIP [39] and CPP [40, 41] architectures. However, for the time being TMR structures play the dominant role in MRAMs. TMR structures are reviewed next.

2.2.3 Tunnel Magnetoresistance

Tunnel magnetoresistance is the magnetoresistance observed in structures where two ferromagnetic (FM) layers are separated by a thin insulator (I) [42–44]. The tunnelling of the electrons in such structures is spin dependent [45] leading to tunnel magnetoresistance [46]. A first approach to explain this phenomenon and estimate the TMR ratio was given in 1975 by Julliere [42] followed Slonczewski's studies in 1989 [47]. By analogy with GMR, if R_P and R_A are the resistances of a GMR structure in the parallel and the antiparallel states, respectively, the TMR ratio can be defined by the following equation:

$$TMR = \frac{R_A - R_P}{R_A} \tag{2.3}$$

According to Julliere's theory [42, 45], TMR can be written in terms of the spin polarisations P of the two ferromagnets:

$$TMR = \frac{2P_1 \cdot P_2}{1 + P_1 \cdot P_2} \tag{2.4}$$

The general layer structure that takes advantage of TMR is the magnetic tunnel junction (MTJ) illustrated in Fig. 2.4a. The material stack is formed by a pinned and a free ferromagnetic layer separated by a thin insulating barrier. Pinning is applied through a SAF layer as in the conventional spin valve. The MTJ's properties are

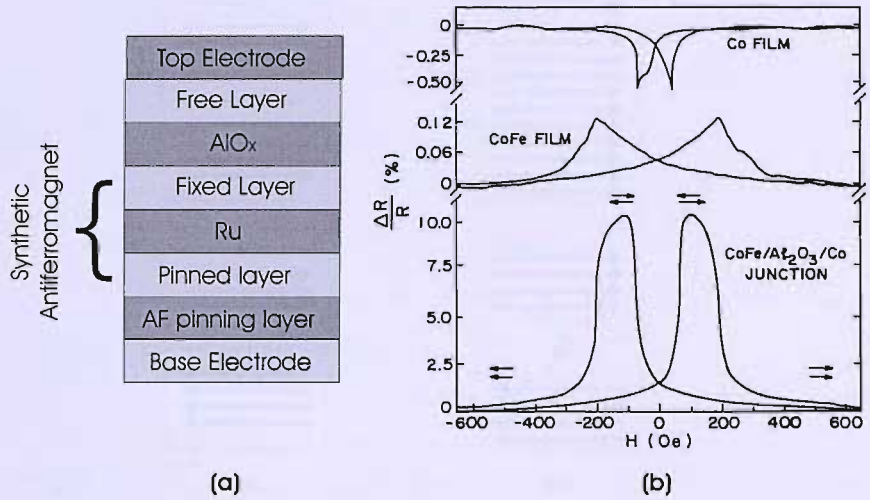

Figure 2.4: *(a) General structure of a magnetic tunnel junction (MTJ). (b) TMR at a $CoFe/Al_2O_3/CoFe$ junction at 296 K. The resistance increases by about 10% in the antiparallel states. The resistance variation of the films are also shown for reference. Moodera et al. [43]*

mostly determined by the thickness and the quality of the insulating layer. Common insulating materials used in MTJs are aluminium and magnesium oxides [45, 48] but other materials have also been used showing promising performances [49–51]. The tunnelling current is usually small leading to large magnetoresistances. The typical TMR ratios achieved by the MTJ structures is in the range of 20 to 40% using magnetic fields smaller than those required for GMR. An example of magnetoresistance measurements at a $CoFe/Al_2O_3/CoFe$ multilayer showing TMR of about 10% at 295 K is given in Fig. 2.4b (Moodera et al. [43]).

Techniques increasing spin polarisation have been used to boost the TMR ratios to values greater than 100% [52, 53]. Moreover, half-metallic materials such as CrO_2 [54], Fe_3O_4 [55] and $La_{0.7}Sr_{0.3}MnO_3$ [56] have almost 100% polarisation and have been used to achieve high TMR ratios. In recent years, Magnesium oxide is becoming very popular giving TMR values as high as 350% at 290 K [48, 57].

Current research on TMR focuses on theoretical studies of the spin dependent tunnelling phenomena and on the effective use of spin polarisation and other techniques to increase the TMR ratios. The main applications of TMR devices are hard-disc read-heads and MRAM.

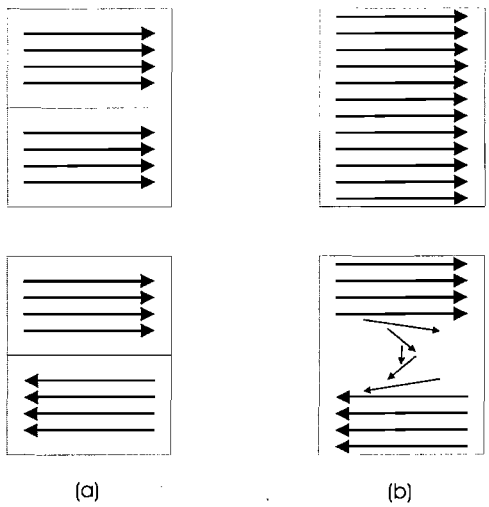

Figure 2.5: *Analogy between GMR and DW-MR. Parallel and antiparallel states of (a) two ferromagnetic layers and (b) one uniform ferromagnet with two domains. The arrows represent the direction of the magnetic moment.*

2.2.4 Domain Wall Magnetoresistance

Domain wall magnetoresistance (DW-MR) refers to magnetoresistance effects in a homogeneous magnetic system caused by spin dependent electron scattering at the domain walls. The application of an external field moves the domain walls causing the resistance of the system to change. This is analogous to the ferromagnetic multilayers of the GMR case. The presence of a domain wall corresponds to antiferromagnetically aligned layers. The absence of domain walls corresponds to ferromagnetically aligned layers. This analogy is illustrated in Fig. 2.5.

Early observations of the DW-MR were reported in 1995 [58, 59] and 1996 [60] and theoretical studies to formulate the phenomenon have been published [61, 62]. The inverse effect of domain magnetisation changes caused by a flowing current has also been observed [63]. One of the most severe problems in DW-MR research is that the anisotropic magnetoresistance effect (AMR) has to be suppressed in order to observe domain wall magnetoresistance phenomena. Thus, special techniques have to be used to extract the contribution of DW-MR from the total measured magnetoresistance [64, 65].

In the literature, both positive [60, 65] and negative [66, 67] DW-MRs have been

reported. Recent advances in theory [68–70] have partially explained the experimental results but the electron scattering at domain walls effect is still under investigation.

All these issues have restricted the possibility of using the DW-MR in spintronic devices or for other applications. However, some work on DW-MR logic devices has already been done [71]. The potential of using DW-MR for quantum measurements has recently been exploited [72]. Finally, promising results on using alloy nanostructures to achieve large DW-MR have been published [73, 74].

2.3 Magnetic Recording

Despite the rapidly growing solid-state electronic memory, magnetic recording is still the dominant information storage technology. The Hard Disc Drive (HDD) has been the flagship of magnetic recording since the 1980s and it is the most wide-spread application of spintronics. A simplified description of the HDD working principle is shown in Fig. 2.6. A magnetic Reading/Writing head flies over a rotating magnetic disc. Applying a magnetic field with an inductive head, it magnetises small portions of the disc surface to a certain direction, thus storing bits of information. These bits can then be read by sensing the magnetic field over each bit cell.

Non-volatility, low cost and scalability are the main advantages of HDDs. Low-speed and the presence of moving parts (introducing sensitivity, power-consumption, reduced reliability and noise) are some of their disadvantages. A magnetic media roadmap is shown in Fig. 2.7 [75]. The impressive increase of storage density in the last decade (over 100% per annum during the late 1990s) was mainly due to the radical advancements of the recording/reading head technology. These advancements were based on the exploitation of spin-dependent transport of electrons through magnetic/non-magnetic/magnetic multilayers (giant magnetoresistance). Magnetoresistance devices are the main elements in Magnetic Random Access Memory (MRAM) and hence they are discussed in the corresponding section (section 2.4).

Currently, storage density is limited by thermal fluctuations on the recording medium [76]. After a density limit known as the super-paramagnetic limit [77], interactions between the stored bits cause loss of information. Such effects become

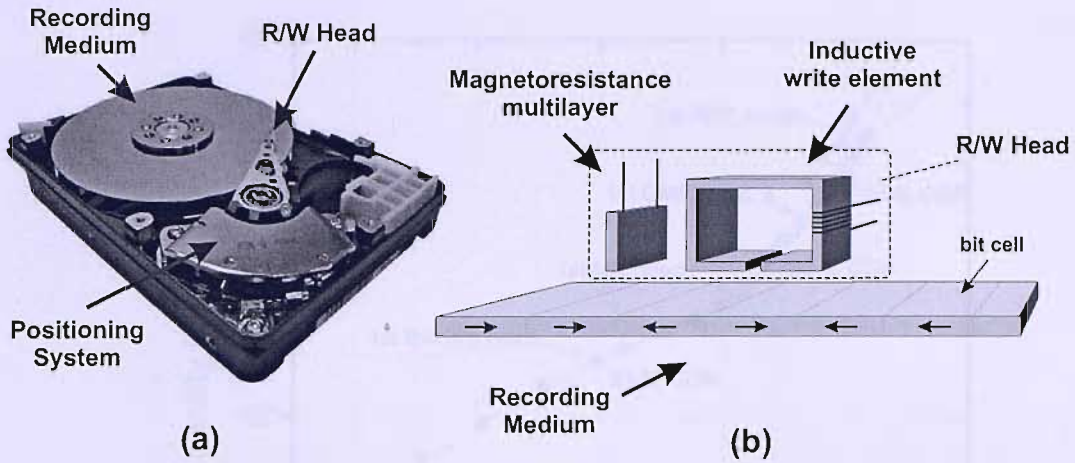

Figure 2.6: *(a) Illustration of the main parts of a hard disc drive (photo by Robert Jacek Tomczak under creative commons copyright). (b) Simplified schematic description of the basic magnetic recording principle.*

significant at densities of around 16 Gb/cm^2 (around 100 Gb/in^2) corresponding to a bit cell size of 80 nm [76]. A variety of alternative storage media technologies have been proposed.

Perpendicular recording is another approach for further increasing the storage density. In contrast with the longitudinal HDD system described in Fig. 2.6, the magnetisation direction can be perpendicular to the surface of the recording medium. Perpendicular recording has been shown to increase the magnetic stability of the bit cells [78] and is very promising for increasing the storage density limits beyond 200 Gbit/in^2 [79].

Patterned recording media [80] have also been considered as a possible way to overcome the superparamagnetic limit. Instead of writing/reading each bit on an ensemble of magnetic grains in a physically continuous medium, each bit is written on an individual island resulting in higher thermal stability [81]. However, high storage densities require patterning in very low dimensions. For example, a density of 0.5 Tbit/in^2 corresponds to an island size of around 36 nm.

Optical lithography cannot reach such low dimensions due to the large wavelength of light [82, 83]. The limits of photolithography (on the scale of 1 μm) have been ex-

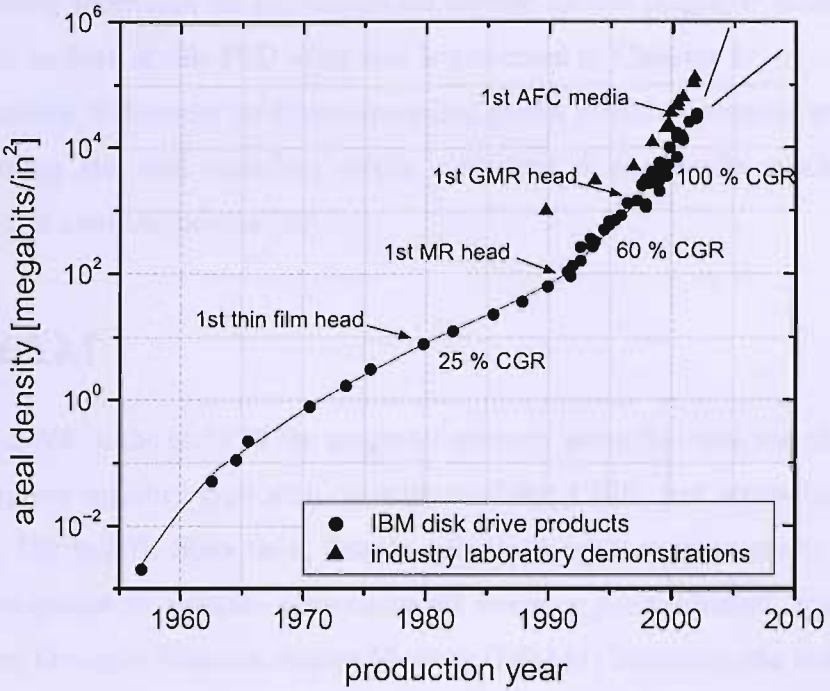

Figure 2.7: *Areal density progress in magnetic recording. The radical increase after 1990 was enabled by magnetoresistance (MR) and giant magnetoresistance (GMR) heads. Novel recording media technologies such as anti-ferromagnetically Coupled (AFC) media would allow further increase of the areal storage density. The annual Compound Growth Rate (CGR) is also shown for 3 different time regions (Moser et al [75])*

tended using X-rays (X-ray lithography). A major drawback of this technology is the high expense of producing X-Rays [84, 85]. Nano-structures down to a few nm can be fabricated by electron beam (e-beam) lithography [86]. However, it is slow and expensive and hence, it is unsuitable for commercial storage media production. Another promising technique is nano-imprinting which involves fabrication of a high-resolution mold and mechanical pattern transfer. The above are all top-bottom nano-fabrication methods. An alternative, bottom-up approach is the exploitation of properties of nature to create ordered structures. This approach is called self-assembly. A variety of self-assembly techniques have been reported as candidates for patterned recording media [80, 87]. A common characteristic of such techniques is the lack of long-range order and guiding has been proposed as a possible solution. In this context, a silicon

integrated guiding technique for self-assembled inverse sphere magnetic arrays has been developed as part of this PhD work and is presented in Chapter 4.

Other promising techniques for future recording media include thermally assisted (hybrid) recording [88] and recording media consisting of chemically synthesised nanoparticles and nanocomposites [89].

2.4 MRAM

From the mid-1950s to the early 1970s, magnetic memory using Fe cores was the predominant computer memory type with capacity reaching 4 Kbit and access times of approximately 120 ns [57]. Since then, despite significant advance in magnetic memories, the development of volatile, semiconductor memory predominated, with the transistor-based Dynamic Random Access Memory (DRAM) becoming the standard chip memory. The reason was that DRAM exhibited high storage density, high speed and low power consumption, overcoming the disadvantage of volatility. Magnetic memory chips were restricted to special-purpose applications in which non-volatility and radiation hardness were of particular importance. Reviews of the development of solid-state memories can be found in the literature [90].

The discovery and exploitation of spin-dependent electron transport (see section 2.2) lead to magnetic devices that used magnetoresistance rather than magnetic induction for reading data. This advance proved to be revolutionary for magnetic reading heads in hard drives and a landmark in the evolution of solid-state magnetic memories, leading to the so-called Magnetic Random Access Memory (MRAM). The basic cell of modern MRAMs is the Magnetic Tunnel Junction as described in Fig. 2.4. The main advantages of MTJs as memory cells are [57]:

- High TMR value
- High resistance (compatibility with CMOS devices)
- Controllable resistance
- Weak TMR temperature dependence

- Scalability while maintaining large TMR

A simplified description of the basic MRAM architecture is given in Fig. 2.8a. A rectangular net of in-plane wires addresses an array of MTJs. The MTJs are located at the cross points of the wires in a via-like fashion. The lower wires are called word lines while the upper are called bit lines. The selection of a particular MTJ can be made by picking the appropriate pair of word and bit lines. The reading process is described in Fig. 2.8b. Supporting circuitry (not shown) forces a current to flow through the selected word and bit lines via the corresponding MTJ. Depending on the state of the MTJ, a low or a large current is detected, corresponding to logical 0 or 1. The writing process is described in Fig. 2.8c. A current is forced to flow across the appropriate word line. This current creates a cylindrical magnetic field H_1 around the wire that flows through all the MTJs of this word line. Then, a current of appropriate direction is passed through the appropriate bit line, imposing another magnetic field H_2 that flows through all MTJs of this bit line. The MTJs are designed such as to switch only when the resultant of H_1 and H_2 is applied. Hence, only the selected MTJ is switched.

The above MRAM architecture uses one MTJ per cell without any supporting devices. In practice, Field Effect Transistors (FETs) are used in series with the MTJs to block sneak currents during the reading process and hence allow more flexibility to the line biasing. Diodes instead of FETs could also be used for this purpose, however it is hard to achieve the required high rectification ratio and large forward currents using the high-conductivity metals of the lines.

An important advancement was the toggle MRAM in which anti-ferromagnetic coupling of the free layer was introduced [91]. This method solved the issue of half-selected cells during the writing process [92]. IBM has demonstrated a 16 Mbit MRAM with read/write time cycle of 30 ns, using toggle technology. A 180 nm CMOS technology was used with the cell size being 1.42 μm^2 [57]. Demonstrations of 16 Mbit MRAMs by Toshiba and NEC have also been reported with similar characteristics [93]. The first commercial MRAM chip was announced in July 2006 by Freescale Semiconductor. It is a 4 Mbit MRAM, including toggle switching, with

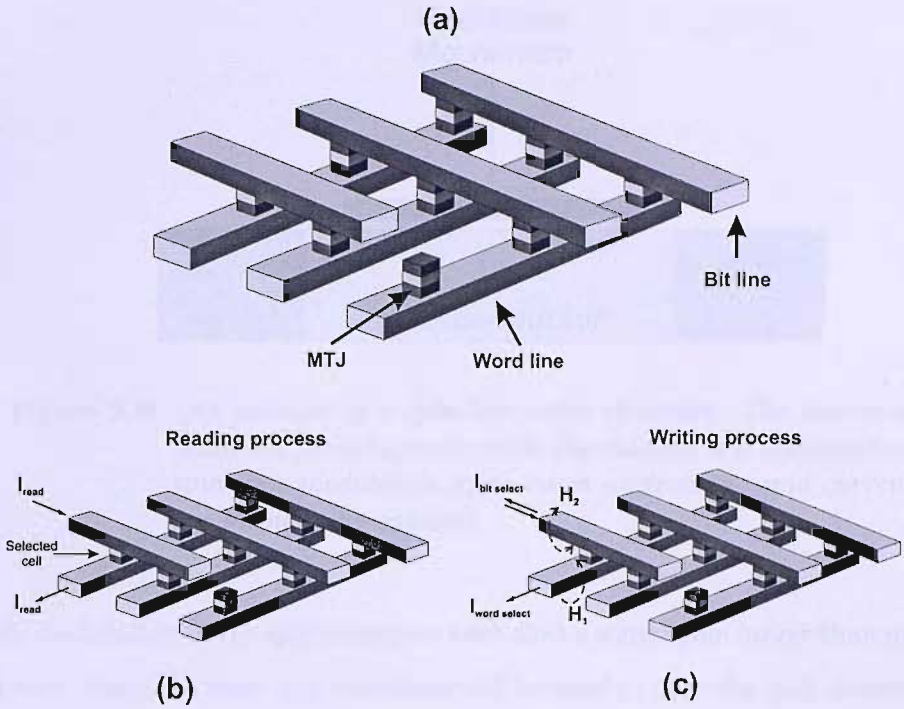

Figure 2.8: *(a) Basic architecture of MRAMs. (b)Reading process. (c) Writing process.*

read and write cycle times of 35 ns [94, 95].

An important issue of MRAM scalability is the increase of the switching magnetic field with decreasing MTJ size. Thermally assisted writing has been proposed as a possible solution [96]. Furthermore, the possibility of replacing the inductive writing method by spin transfer has been considered. Instead of applying an external magnetic field, a spin-polarised current passing through the magnetic material can be used to switch its magnetisation. This reversal originates from the exchange of angular momentum between spin polarised current and the magnetisation of the medium. A study of the potential of spin transfer applications can be found in [97].

2.5 Spin Transistors

The magnetoresistance devices discussed in the previous sections have two terminals and allow or prevent current to pass depending on the relative magnetic orientation in their ferromagnetic parts. This function is passive. An active spin device would

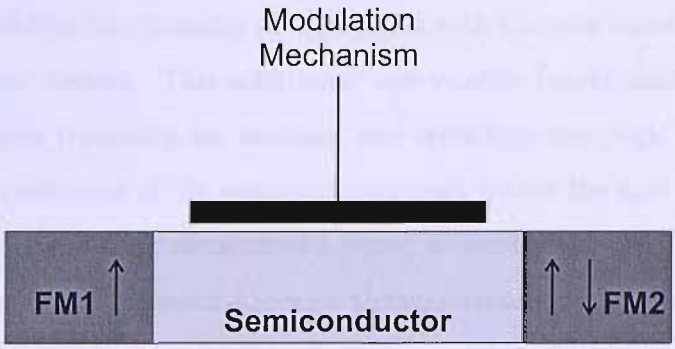

Figure 2.9: *An example of a spin-transistor structure. The source and the drain are ferromagnetic while the channel is a semiconductor. A spin-wise modulation mechanism controls the spin current flowing through the channel.*

imply modulation of the spin transport such that a signal gain larger than unity can be achieved. Here, the term spin transistor will be used to describe such devices. In order to achieve gain, non-linear characteristics are desirable and therefore the introduction of semiconductors in spin transistors is of particular interest. A general example of such a device is shown in Fig. 2.9. A current passes through a ferromagnetic region and becomes spin polarised. This current is then injected into a semiconductor through a tunnelling or a Schottky contact. The current flow is modulated as it passes through the semiconductor. Finally the spin polarised current is collected at a second ferromagnetic region through another tunnelling or Schottky contact.

The above device demonstrates some very important spintronics issues. Firstly, the injection of spin polarised current (so-called spin-injection) into a semiconductor and its detection require non-ohmic contacts due to the conductivity mismatch between metals and semiconductors [98]. Secondly, the spin current in the semiconductor can either be driven conventionally by charge diffusion or by novel effects such as spin diffusion [99]. Thirdly, modulation of the spin-polarised current in the semiconductor can be achieved either by conventional means (e.g. control of the carrier concentration in the semiconductor channel) or by spin effects such as spin-orbit interaction [100].

While these matters make the spin transistor very attractive for the exploration of the associated physical effects, it is also potentially beneficial as a device. Firstly, it

combines the modulation functionality of transistors with the spin valve functionality of magnetoresistance devices. This additional non-volatile functionality is a direct advantage of the spin transistor for memory and reconfigurable logic applications. Secondly, the high resistance of the semiconductor part makes the spin transistor an excellent candidate as the basic element of 1 (spin) transistor per cell MRAM.

On the other hand, it is interesting to view the spin transistor as a potential alternative to the conventional Bipolar Junction Transistor and the Field Effect Transistor. High transconductance gain and speed, low power consumption and viable scalability are essential requirements for such applications. The short spin-flip time (1 ns) and the low associated energy (ΔE(spin) $\sim 8.6 \cdot 10^{-8}$ eV) [101] give a potential advantage to the spin-transistor for speed and power consumption. In addition, studies on spin and orbit diffusion and propagation in semiconductors have shown that nearly dissipationless spin - currents could be possible [102]. A wide variety of architectures have been proposed with very different approaches on the working principles and the implementation [5, 99, 100, 103–107]. However, electrical spin generation and detection still remains to be demonstrated and spin transistors with significant gain have not yet been reported.

2.6 Silicon Spintronics

Silicon is the dominant semiconductor in conventional electronics and its use in future devices is beneficial for compatibility reasons and also because of the unparalleled existing knowledge and processing ability for Si. The use of Si in magnetic recording media for instance may allow integration of the additional electronic circuitry with the recording disk. Moreover, in the case of patterned recording media, Si technology could actively assist the micro-fabrication process. Similarly, the use of Si in MRAMS could lead to integrated microchips incorporating magnetic memory and CMOS technology.

In addition, semiconductors may play a very important role as active parts of spin transistors for the following reasons:

- Active devices require non-linear characteristics which appear in semiconduc-

tors.

- Working devices must have substantial resistance to be compatible with conventional electronics.
- Spin applications such as quantum computers require semiconductors.

Low spin-orbit coupling makes Si unsuitable for devices with modulation based on the Rashba effect [102]. Moreover, it has weak optical properties which prevent the generation or detection of spin currents by optical means. These two reasons have discouraged research on Si-spintronics. Nevertheless, some key advantages of Si over other semiconductors should be recognised. First, the long spin relaxation time of Si is a benefit for spin transport. Second, Si is ideal for another potential application of spin-transport in semiconductors, namely the detection of nuclear states in quantum computers, for which III/V compounds are not suitable [108].

The aforementioned facts, along with the unmatched Si processing ability and the dominance of Si in conventional electronics make Si spintronics a very promising field.

Chapter 3

Electrodeposition of Ni on Si

In this chapter an introduction to electrodeposition is presented. The advantages of electrodeposition over other metallisation techniques for spintronics are highlighted. A description of a manually built electrodeposition setup is given and original results on electrodeposition of Ni on n-type Si with different resistivities, without seed layers are reported. Cyclic voltammetry results are fitted with a model of the voltage drop in the Si electrode revealing that a back-contact is not essential. Selective electrodeposition on patterned Si/SiO_2 is achieved demonstrating compatibility of the technique with other microelectronics processes. The film growth modes are studied by electron microscopy and a correlation among the electrochemical conditions, the roughness and the magnetic properties of the film is demonstrated.

This chapter is partly published in IEEE Trans. Magn. **41**, 2639, 2005.

3.1 Introduction

In microelectronics, metallisation is conventionally performed by Physical-Vapour Deposition methods like evaporation and sputtering and, less often, by Chemical-Vapour Deposition (CVD). Evaporation occurs when a source material is heated above its melting point in vacuum. The evaporated atoms then travel at high velocity in straight-line trajectories. The source can be melted by resistance heating, rf heating or with an electron beam (e-beam evaporation). In sputtering, ions are accelerated toward the target. The sputtered material deposits on a wafer that is placed facing

the target [109].

Electrodeposition as a metallisation method, is very attractive because it is simple, mature and cost effective. Moreover, it does not need vacuum or high temperatures and results in high quality metal layers. In contrast with evaporation and sputtering, it has the unique ability of building structures in three dimensions and therefore it is suitable for a particular patterning technique involving self-assembly of latex spheres (see chapter 4). Due to the low energy involved with electrodeposition, it is also expected to minimise intermixing at the Ni-Si interface and potentially give a high quality Schottky barrier (see chapter 5). For these reasons, electrodeposition is chosen as the metallisation technique for the work presented in this thesis.

3.1.1 Previous Work

Direct electrodeposition of metals onto silicon has attracted a lot of interest [110]. In particular for magnetic metals and multilayers most of the research is focused on electrodeposition on n-type silicon [111–113] and only a few successful experiments using p-type substrates have been reported [114]. The reason is that, in the second case, the Schottky barrier formed between the p-type Si and the solution and between the p-type Si and the first electrodeposited metallic layer is reverse biased during electrodeposition, reducing the current flow and hence disturbing the film growth.

The great majority of published work on electrodeposition on Si refers to alloys or multilayers of Cu with magnetic materials. The possibility of controlling the composition of Cu/Ni alloys on silicon by the electrodeposition potential has been demonstrated [115]. Giant magnetoresistance has been observed on Cu/Co alloys [116] and NiFe/Cu and Co-Ni-Cu/Cu multilayers [111, 117], all electrodeposited on n - type Si. Formation of rod-like Ni clusters on (111) Si substrates has been reported [118]. Lastly, Cobalt/Nickel alloys have successfully been electrodeposited on Si [119].

In almost all studies, Si substrates were treated with etchant agents (typically baths containing hydrofluoric acid) to remove all the dioxide from the Si surface. In contrast, for electroless deposition, increase of magnetic layer uniformity and increased deposition speed are reported, using substrates covered by a very thin silicon

dioxide layer [120]. Very promising results have been published on electroless deposition of magnetic materials on Si [121] and the mechanisms of this method have been recently investigated [122].

Typically, in the work summarised above, a back contact is used to enhance the conductivity of the semiconducting substrate. Moreover, in most cases, a seed layer is deposited on the semiconductor prior to electrodeposition. The work presented in this chapter involves electrodeposition directly on Si without a seed layer and without a back contact.

3.1.2 Outline

In the rest of this chapter a brief introduction to electrodeposition is given. The non-uniformity of the potential along a semiconducting electrode is expected to affect the interface and thickness uniformity of the depositing film. For this reason, a theoretical analysis of the voltage drop in a Si electrode during electrodeposition is presented revealing the necessary conditions for uniform deposition. A simple way to control the film thickness is also demonstrated and a description of the experimental setup that was developed as part of this PhD work is given. Then, experimental results are presented and compared with theoretical predictions for the electrodeposition process. Results of electrodeposition on patterned Si are presented and the film growth modes are studied. The roughness and the magnetic properties of the film are characterised and associated with the electrodeposition conditions.

3.2 Electrodeposition

Electrochemical deposition of a metal on a substrate involves the reduction of metal ions X^{z+} from an electrolyte:

$$X^{z+}_{electrolyte} + z \cdot e^{-} \longrightarrow X_{lattice} \tag{3.1}$$

Depending on whether the electrons are provided by an external power supply or by a reducing agent in the solution, this process is called electrodeposition or

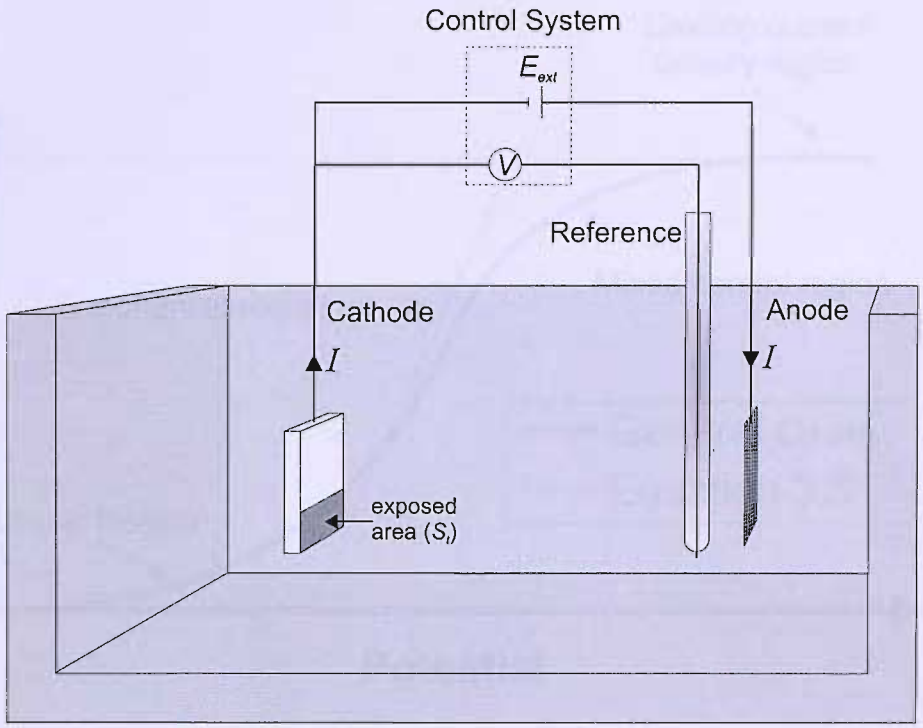

Figure 3.1: *Illustration of a simple, 3-electrode electrodeposition setup.*

electroless deposition, respectively. As electrodeposition is the process used for all the experiments presented in this work, electroless deposition will not be discussed here.

A typical electrodeposition setup is illustrated in Fig. 3.1. Three electrodes are used: the cathode, the anode and the reference electrode. Current flows through the cathode and the anode while the potential of the cathode is measured against the reference electrode.

When an electrode is immersed in an electrochemical solution and no current is flowing through it, it obtains a potential E that is called equilibrium potential. This potential is standard for the particular electrode and solution. If an external voltage is applied to the system, a current (I) will flow. Then, the voltage drop $\grave{E}$ across the electrochemical system will in general be different from the equilibrium potential E. The difference $\eta = \grave{E} - E$ is called the overpotential. The overpotential is given by the Tafel equation:

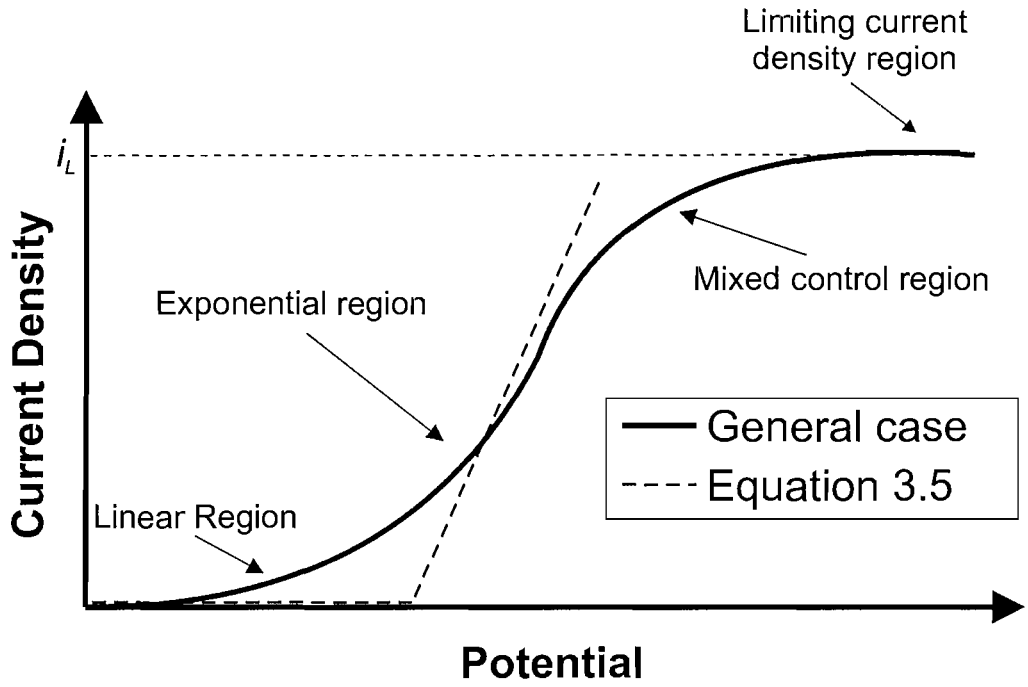

Figure 3.2: *Four regions in the general current potential relationship of electrodeposition. The dashed line represents the approximation used in the theoretical considerations of this chapter, as implied by equation 3.5.*

$$\eta = a \pm b \cdot log|J| \tag{3.2}$$

where J is the current density and a and b are constants. A more general description of the current-potential $(I - V)$ relationship during electrodeposition is the Butler-Volmer equation [123], which is graphically illustrated as the exponential region in Fig. 3.2.

At high enough potentials, mass transport limits the current to a maximum value:

$$I_L = \frac{z \cdot F \cdot D}{\delta} \tag{3.3}$$

where F is the Faraday constant, D is the diffusion coefficient of the depositing species X^{z+} and δ is the diffusion layer thickness. The Faraday constant represents one mole of electrons and it is given by:

$$F = N_A \cdot q \tag{3.4}$$

where N_A is Avogadro's number and q is the elementary charge. For the theoretical considerations presented in this work, the relation between the current density and the electrochemical potential will be approximated by the following linear equation:

$$J = \begin{cases} \kappa \cdot (\phi - \phi_T) & : \quad \phi > \phi_T \\ 0 & : \quad \phi \leq \phi_T \end{cases} \tag{3.5}$$

where κ and ϕ_T are fitting parameters measured in $\Omega^{-1} \cdot \text{cm}^{-2}$ and Volts respectively. This approximation is graphically illustrated in Fig. 3.2. The charge Q_M collected at the cathode as a result of the metal ions reduction at it during electrodeposition is given by:

$$Q_M = N_M \cdot F \cdot z \tag{3.6}$$

where N_M is the electrodeposited metal in moles. In electrochemical experiments, other reactions like hydrogen reduction contribute to the total charge Q_t accumulated at the cathode. The current efficiency α of the metal reduction is defined as:

$$\alpha = \frac{Q_M}{Q_{total}} \tag{3.7}$$

Moreover, from equation 3.6, the film thickness as a function of Q_{total} can be derived:

$$\tau = \frac{\alpha \cdot A_M \cdot Q_{total}}{z \cdot F \cdot d_M \cdot A} \tag{3.8}$$

where A, A_M and d_M are the electrodeposition area and the atomic weight and density of the material respectively. The considerations above are very useful for estimating the metal ion concentration reduction due to electrodeposition in the solution from charge measurements. Furthermore, the film thickness can be monitored during electrodeposition by measuring the charge accumulation at the cathode.

Several different electrodeposition methods exist, depending on the way the volt-

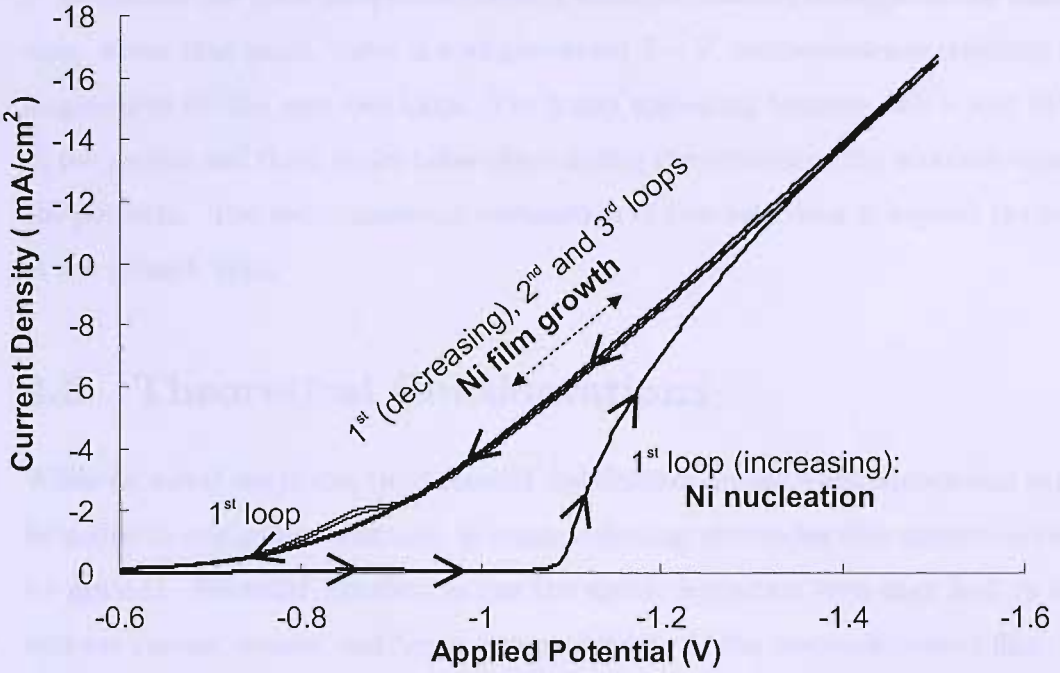

Figure 3.3: *Cyclic voltametry measurement of electrodeposition of Ni on Si. During the first loop, nucleation takes place for voltages between about 1.1 V and 1.3 V. The reducing voltage part of the first loop and the next two loops overlap, indicating film growth.*

age (or current) is applied. DC amperometry refers to the application of constant voltage, while current is measured during electrodeposition. DC Voltametry refers to the application of a constant current, while the voltage is measured. Cyclic voltametry refers to the application of a voltage ramp from a low to a high value and back while the current is measured. Cyclic voltametry is a very useful electrochemistry tool as it allows the investigation of different electrodeposition modes. As an example, a cyclic voltametry measurement of electrodeposition of Ni on Si performed as part of this PhD work is illustrated in Fig. 3.3.

Three voltage ramps were applied, from -0.6 V to -1.5 V. During the first loop, there is no electrodeposition current until a certain threshold potential near -1.1 V. Above that threshold the potential is high enough to cause Ni nucleation and subsequently Ni film growth. As nucleation goes on, more and more sites of the substrate become active and the current increases rapidly. At approximately -1.3

V nucleation has been completed allowing electrodeposition throughout the exposed area. From that point, there is a single-valued $I - V$ correspondence resulting in a single curve for the next two loops. The bump appearing between -0.8 V and -0.9 V at the second and third cycles takes place during the increase of the absolute value of the potential. The electrochemical explanation of this behaviour is beyond the scope of the present work.

3.3 Theoretical Considerations

While on metal electrodes the potential distribution during electrodeposition is uniform due to negligible resistance, in semiconducting electrodes this cannot be taken for granted. Potential variation across the electrodeposition area may lead to non-uniform current density and hence, non-uniformity of the electrodeposited film. For this reason, the potential distribution on semiconducting electrodes was studied and is presented in this section. Also, a method for film thickness control using charge measurements at the cathode is presented. These theoretical consideration were of particular importance for the successful performance of the electrodeposition experiments and interpretation of the results which are discussed in section 3.5.

3.3.1 Voltage drop along Si electrodes

In electrodeposition experiments, it is sometimes the case that the cathode (the electrode on which the electrodeposition is taking place) is connected to the power supply using a "crocodile clip". Part of the substrate is immersed into the electrolyte for deposition and the rest is exposed to air. Moreover, the immersed part is covered by an isolation layer leaving only a small window of a particular size to be exposed to the electrolyte, as in Fig. 3.1. In this setup, the potential on the electrodeposition surface (shadowed area in Fig.3.1, S_t) will not be uniform, because of the voltage drop caused by the flowing current. For electrodeposition on metals this voltage drop may be neglected but in lowly doped semiconductors it should be considered as it could result in non-uniform material deposition. The potential distribution and the current along a Si electrode was calculated under the following assumptions:

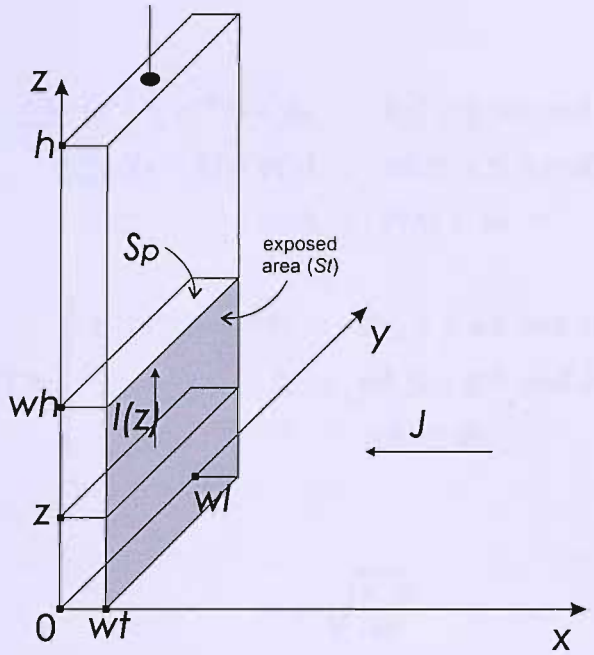

Figure 3.4: *Geometry of the Si electrode. The shaded area (S_t) is exposed to the solution while the rest of the electrode surface is isolated.*

- The potential will vary only with the distance from the top of the cathode. This means that the horizontal surfaces in the cathode will be considered as constant potential surfaces.

- The reference potential is that of the anode: $\phi_{anode} = 0\ V$.

- The ϕ (potential)-J (current density) characteristic of the electrolysis phenomenon is the same for all points on S_t, and can be modelled by equation 3.5.

- Without affecting the universality of the calculations it will be assumed that the width of S_t is equal to the width of the whole cathode.

In Fig. 3.4 the geometric parameters of the electrode are illustrated.

The general expressions for the potential and the current along the electrode are calculated to be:

$$\phi(z) = \begin{cases} \frac{\lambda \cdot c}{\kappa \cdot wl} \cdot (e^{\lambda \cdot z} + e^{-\lambda \cdot z}) + \phi_T & : \quad 0 \leq z \leq wh \text{ and } \phi(h) > \phi_T \\ \frac{\rho \cdot I_t}{wt \cdot wl} \cdot (z - h) + \phi(h) & : \quad wh \leq z \leq h \text{ and } \phi(h) > \phi_T \\ \phi(h) & : \quad \phi(h) \leq \phi_T \end{cases} \tag{3.9}$$

$$I(z) = \begin{cases} c \cdot (e^{\lambda \cdot z} - e^{-\lambda \cdot z}) & : \quad 0 \leq z \leq wh \text{ and } \phi(h) > \phi_T \\ I_t & : \quad wh \leq z \leq h \text{ and } \phi(h) > \phi_T \\ 0 & : \quad \phi(h) \leq \phi_T \end{cases} \tag{3.10}$$

where:

$$\lambda = \sqrt{\frac{\kappa \cdot \rho}{wt}} \tag{3.11}$$

$$c = \frac{\kappa \cdot wl \cdot wt \cdot (\phi(h) - \phi_T)}{\lambda \cdot wt \cdot (e^{\lambda \cdot wh} + e^{-\lambda \cdot wh}) - \kappa \cdot \rho \cdot (wh - h) \cdot (e^{\lambda \cdot wh} - e^{-\lambda \cdot wh})} \tag{3.12}$$

$$I_t = \frac{\kappa \cdot wl \cdot wt \cdot (e^{\lambda \cdot wh} - e^{-\lambda \cdot wh}) \cdot (\phi(h) - \phi_T)}{\lambda \cdot wt \cdot (e^{\lambda \cdot wh} + e^{-\lambda \cdot wh}) - \kappa \cdot \rho \cdot (wh - h) \cdot (e^{\lambda \cdot wh} - e^{-\lambda \cdot wh})} \tag{3.13}$$

In the above equations, ρ is the Si resistivity and $\phi(h)$ is the applied potential. From these equations, all quantities of the system can be calculated. I_t reflects the total current running through the electrode and hence, equation 3.13 gives the $I - V$ characteristic (I_t versus $\phi(h)$) of the electrodeposition setup. The detailed derivation of these equations is described in Appendix A, along with some numerical examples.

Simplified model

In this section the possibility of neglecting the voltage drop along the exposed area will be examined. The simplified electrical equivalent of the system is shown in Fig. 3.5.

By analogy with equation 3.5 the electrical behaviour of the electrochemical junction can be described to a first approximation by the following expression for the

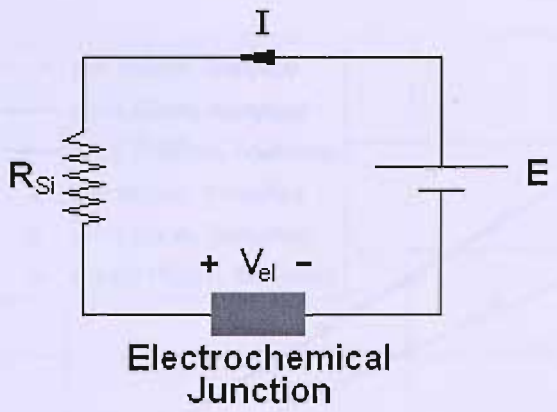

Figure 3.5: *Simplified electrical model of an electrodeposition setup.*

current:

$$I = \kappa \cdot S \cdot (V_{el} - \phi_T) \tag{3.14}$$

where κ and ϕ_T are constants defined in the previous subsection and S is the area of the electrode exposed to the electrochemical solution. Neglecting the contribution of the exposed Si area, the ohmic resistance of the electrode will be:

$$R_{Si} = \rho \cdot \frac{h - wh}{wl \cdot wt} \tag{3.15}$$

After simple circuit analysis it is found that the current is given by:

$$I = \frac{E - \phi_T}{\frac{1}{\kappa \cdot S} + \rho \cdot \frac{h - wh}{wl \cdot wt}} \tag{3.16}$$

Equation 3.16 is a limiting case of equation 3.13. Finally, the current density on the exposed area will be:

$$J = \frac{E - \phi_T}{\frac{1}{\kappa} + \rho \cdot \frac{wh}{wt} \cdot (h - wh)} \tag{3.17}$$

This model gives a very good approximation of the $J - V$ characteristic. A numerical example is shown in Fig. 3.6 corresponding to typical geometrical values used in the experiments. The curves from the analytical model match those given by

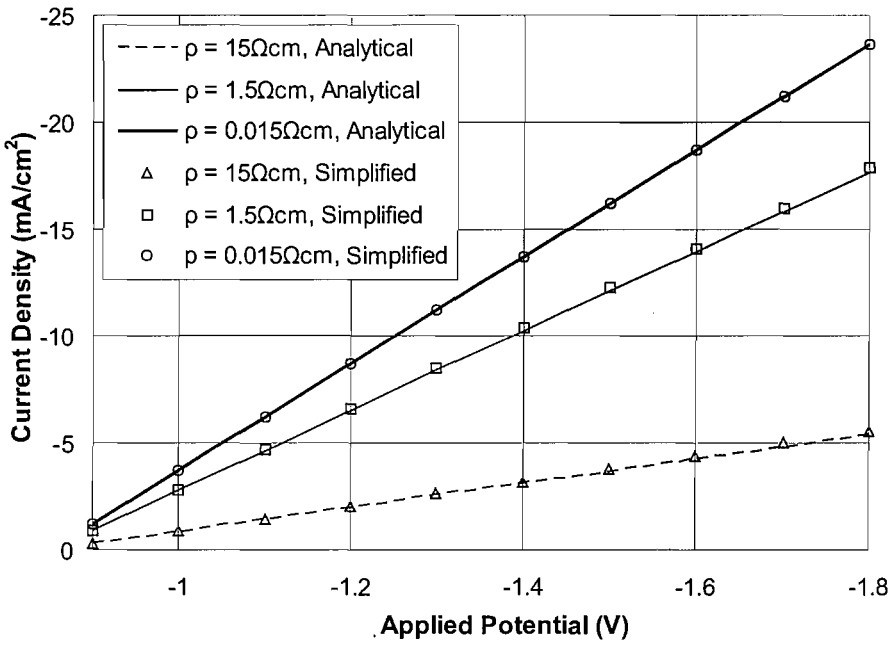

Figure 3.6: *Comparison between J - V curves obtained from the analytical (equation 3.13) and the simplified (equation 3.17) models.*

the simplified model.

Contribution of the electrodeposited metal

During electrodeposition of metals on Si substrates the growing film adds its conductivity to that of the Silicon electrode and contributes to the transport of current through it. In this brief analysis, this effect will be discussed. The general case is illustrated in Fig. 3.7a. The current is flowing vertically, along the dimension h. The two parts are connected in parallel and the equivalent electrical circuit is shown in Fig. 3.7b.

If ρ_{Si} and ρ_{metal} are the resistivities of Si and the metal respectively the total resistivity will be:

$$\rho_{tot} = \frac{b_{Si} + b_{metal}}{\frac{b_{Si}}{\rho_{Si}} + \frac{b_{metal}}{\rho_{metal}}} \tag{3.18}$$

where b_{Si} and b_{metal} are the thicknesses of the Si and the metal respectively. A nu-

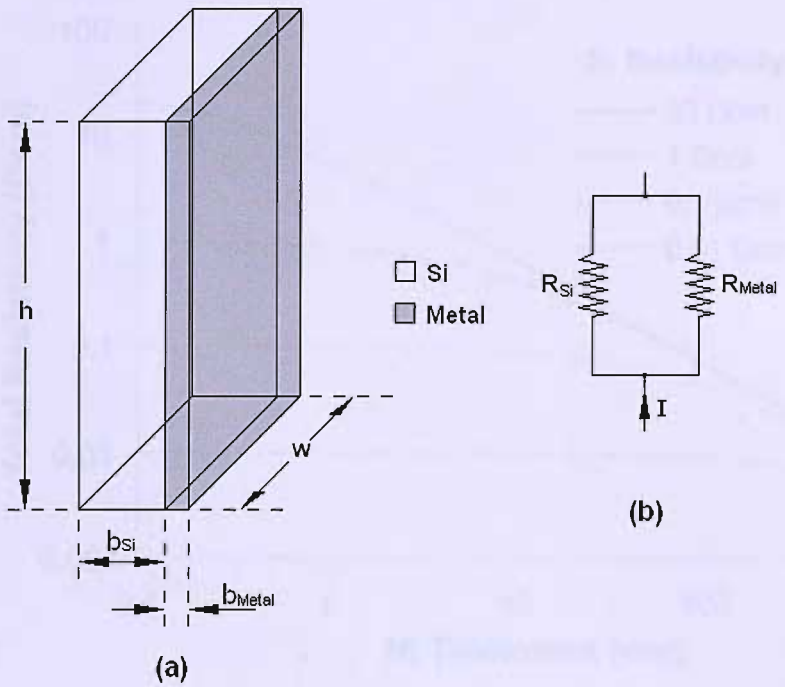

Figure 3.7: *(a) General Geometry of metal electrodeposited on Si and (b) equivalent electrical circuit.*

merical example is illustrated in Fig. 3.8, for Ni ($\rho_{Ni} = 7 \cdot 10^{-6}\Omega \cdot cm$) and a typical value of the Si wafer thicknesses: $d_{Si} = 0.5mm$. In this figure, the total resistivity versus Nickel layer thickness has been plotted for Si substrates with different resistivities. During the early stages of electrodeposition (Ni layer thickness $< 1nm$) the impact of the Ni film on the total electrode resistivity is minor and can be completely neglected for Si resistivities up to $1\Omega \cdot cm$. For higher resistivities or higher Ni film thicknesses, the total resistance starts decreasing. Therefore, a current increase with increasing film thickness is expected to appear. The significance of this effect will be determined by the relative size of the electrodeposition area as compared with the total size of the Si electrode. Similar conclusions can be extracted for other metals (e.g. Cobalt, $\rho_{Co} = 6 \cdot 10^{-6}\Omega \cdot cm$).

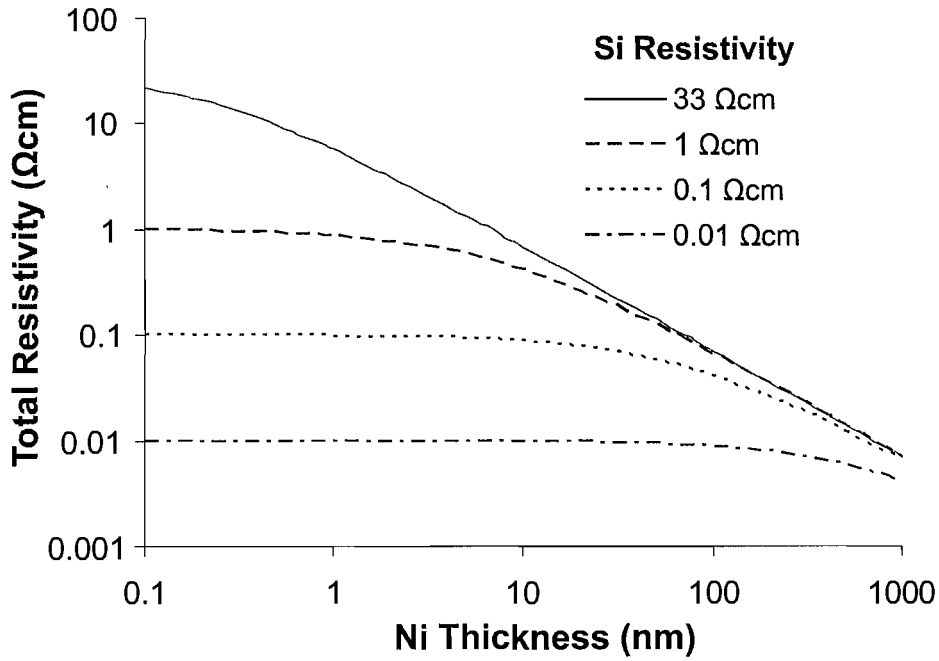

Figure 3.8: *Effect of film growth on the total electrode resistivity in the geometry illustrated in Fig. 3.7.*

3.3.2 Film Thickness Control

Equation 3.8 gives a direct relationship between the charge measured at the cathode during electrodeposition and the film thickness. Therefore it offers a way of real-time film thickness control. However, the current efficiency α has to be determined. Measuring the film thickness after electrodeposition would result in an estimate of α directly from equation 3.8. Moreover it would give valuable feedback for the determination of the accuracy of this method.

The film thickness can be measured by many different means. A very popular technique is using cross section Scanning Electron Microscopy (SEM). The substrate is cleaved in such a way as to reveal a cross section of the electrodeposited film and then it is examined by SEM. Atomic Force Microscopy (AFM) could also be used to scan the deposited area and measure the step height at the edges. Particularly for magnetic materials, another way would be to measure the saturation magnetisation M_s of the film. Then, if $\widehat{M}_{material}$ is the magnetisation per unit mass of the material,

the total mass of the film will be given by:

$$m = \frac{M_s}{\widehat{M}_{material}} \tag{3.19}$$

If d_M and A are the density and the area of the film respectively, the film thickness can be calculated from the following equation:

$$\tau = \frac{M_s}{\widehat{M}_{material} \cdot d_M \cdot A} \tag{3.20}$$

3.4 Experimental Conditions

An electrodeposition setup was build in the INNOS Ltd cleanrooms as part of this PhD work, using an Autolab AUT72032 potentiostat three electrode system with a Pt counter electrode and a saturated calomel reference electrode (SCE). A Ni sulphate aqueous solution was manually prepared using a recipe from the literature [124]. Its composition is given in table 3.1.

Table 3.1: *Composition of the solution used for Ni electrodeposition[124].*

Ingredient Name	Chemical Formula	Quantity (mol dm^{-3})
Ni Sulphate	$NiSO_4{\cdot}6H_2O$	0.1
Boric Acid	H_3BO_3	0.1
Sodium Dodecyl Sulphate (SDS)	$CH_3(CH_2)_{11}OSO_3Na$	0.005

The volume of the beaker used for electrodeposition was 6 cm^3. Electrodeposition of Ni on plain Si wafers and on Si wafers with SiO_2 patterns was performed. All wafers were n-type with (100) crystal orientation. Three different resistivities were used: 0.01-0.02 Ω cm, 1-2 Ω and 10-20 Ω cm. The patterns were defined by conventional photolithography on a thermally grown 250 nm thick SiO_2 layer such as to expose Si at certain areas. A test mask containing squares, triangles, circles and stripes of different sizes was used. A brief description of this mask can be found in Appendix B. All wafers were sawed in pieces and RCA cleaned. A 20:1 buffered HF (BHF) dip just before electrodeposition was used to remove the native oxide from the exposed

Si surface.

The Ni film thickness was controlled by measuring the charge accumulating at the cathode during electrodeposition and using the equations presented in section 3.2. The current efficiency was estimated by film thickness measurements as explained in section 3.3.2. A typical value of the cathode charge for each electrodeposition run was 0.5 C. From equation 3.6 it was found that the metal ion consumption was small enough to maintain the 6 cm^3 solution concentration for up to 20 runs.

Characterisation of the electrodeposited films was performed using an optical microscope, a Topometrix $100\mu\ 10-Z$, linearised Accurex Atomic Force Microscopy (AFM) Explorer and a Hitachi S-4800 FESEM Field Emission Scanning Electron Microscope (FESEM). Magnetic Measurements were performed at room temperature using an Oxford Instruments 3001 Vibrating Sample Magnetometer.

3.5 Results and Discussion

3.5.1 Electrodeposition on Resistive Si

Cyclic voltametry was applied to explore the electrochemical, current density (J) versus applied potential (V) characteristic of Ni electrodeposition on n-type, 0.01-0.02 Ω cm Si without using a back contact. The measurements are shown in Fig. 3.9

As the applied potential is increased, there is no electrodeposition current until a certain threshold potential near -1.1 V. Beyond that threshold the potential is high enough to cause Ni nucleation and electrodeposition on top. As nucleation continues, more and more sites of the substrate become active and the current increases. After nucleation is completed, the $J-V$ characteristic follows a straight line which can be fitted by equation 3.17 from the model developed in section 3.3.1. The geometrical parameters used were those of the actual Si electrode used in the experiment, while κ and ϕ_T were used as fitting parameters. The mean value of the Si resistivity specification was used (0.015 Ω cm for 0.01-0.02 Ω cm Si). This fit is shown as a bold solid line in Fig. 3.9. The parameter values used are summarised in table 3.2.

In addition, cyclic voltametry measurements were performed for electrodeposition

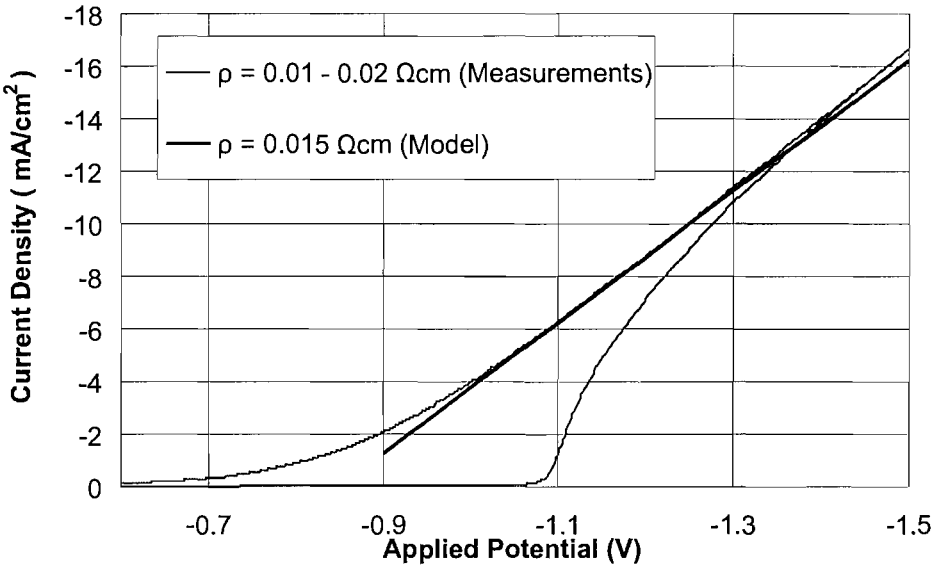

Figure 3.9: *Cyclic voltametry measurements of Ni electrodeposition on 0.01-0.02 Ω cm Si. The measurements are fitted with the theoretical model for Si electrodes presented in section 3.3.1.*

Parameter	Unit	Value
wh	cm	0.25
wt	cm	0.05
h	cm	2
κ	Ω^{-1} cm^{-2}	0.025
ϕ_T	V	-0.85
ρ	Ω cm	0.015

Table 3.2: *Fitting parameters for the Ni electrodeposition on Si shown in Fig. 3.9.*

of Ni on n-type Si with resistivities 1-2 Ω cm and 10-20 Ω cm, again without a back contact. The measurements for all three resistivities (including 0.01-0.02 Ω cm) are shown in Fig. 3.10. As expected from the analysis of section 3.3.1, the increased substrate resistivity reduces the electrodeposition current. Thus, electrodeposition is taking place at a lower rate on high resistivity substrates. However, the threshold potential after which nucleation starts is near -1.1 V and does not depend on the substrate resistivity. This is because at lower voltages, before nucleation begins there is practically no current flowing and hence, there is no voltage drop along the electrode.

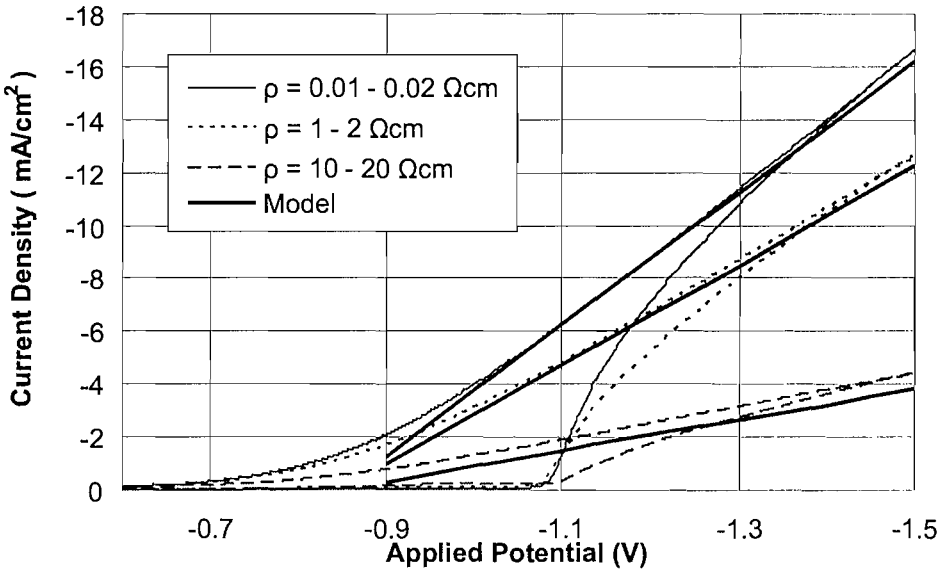

Figure 3.10: *Cyclic voltametry curves of Ni electrodeposition on Si with different resistivities. The thick solid lines correspond to the simple model presented in section 3.3.1 with the nominal Si resistivity of 0.015 Ω cm, 1.5 Ω cm and 15 Ω cm respectively.*

By using the resistivity of the specifications of the respective Si substrates, an accurate fit of the measurements is obtained for all three resistivities. The values of all other parameters were kept the same as given in table 3.2. The fitting curves are shown as bold solid lines in Fig. 3.10. The deviation observed for the high resistivity case is within the resistivity specification limits of the Si substrate used (10-20 Ω cm).

The above results reveal that direct electrodeposition on resistive Si substrates is possible without the need of back contact. The only visible effect of high resistivity Si is the voltage drop in the substrate which imposes higher potentials to achieve electrodeposition.

3.5.2 Electrodeposition on Patterned Si

Electrodeposition on patterned Si-SiO_2 electrodes was performed using a solution and samples prepared as described in section 3.4. Ni was deposited selectively on the exposed Si, as shown in the 3D AFM image of Fig. 3.11. It is apparent that the deposited film is very rough. This roughness has been found to be independent of whether a patterned substrate is used or not. In contrast, by changing the electrode-

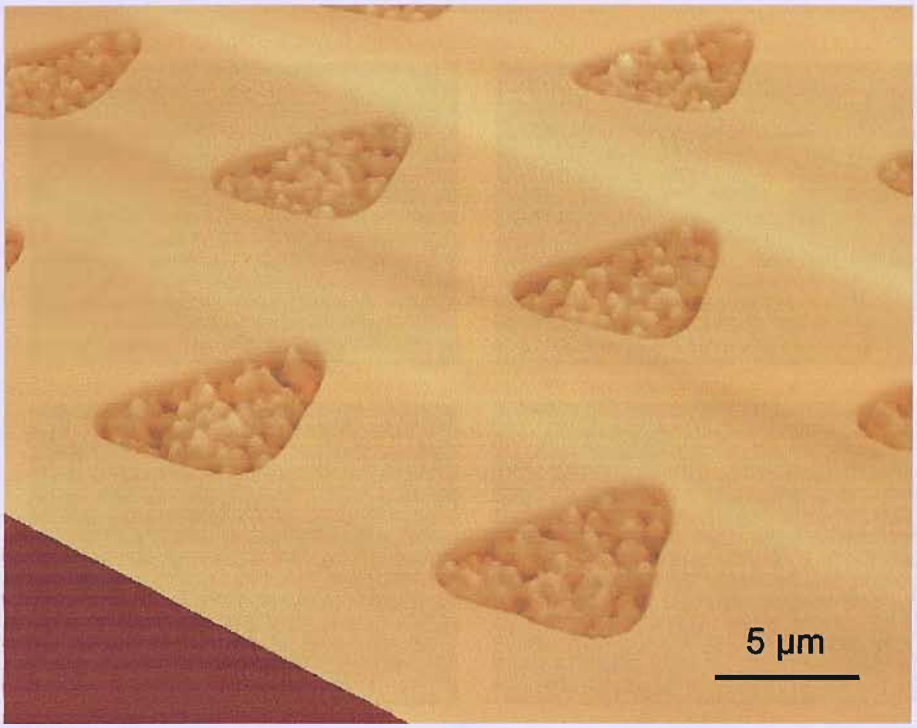

Figure 3.11: *3D AFM images of Ni electrodeposited on patterned Si, by applying a pre-treatment electrochemical pulse of -1.5 V for 0.2 s and cyclic voltametry from -0.5 V to -2.1 V and back.*

position conditions, modification of the roughness can be achieved. In order to study this effect and achieve smoother electrodeposition the mechanisms of the film growth is discussed next.

3.5.3 Film Growth

Nucleation

In the early stages of electrodeposition, nucleation of the metal on Si is taking place. The nuclei are "starting points" that attract further Ni atoms and grow bigger until a film is formed. The nucleation stage has been experimentally studied by applying short pulses of different durations and voltages and taking SEM images. A step-by-step description of the nucleation process is shown in Fig. 3.12.

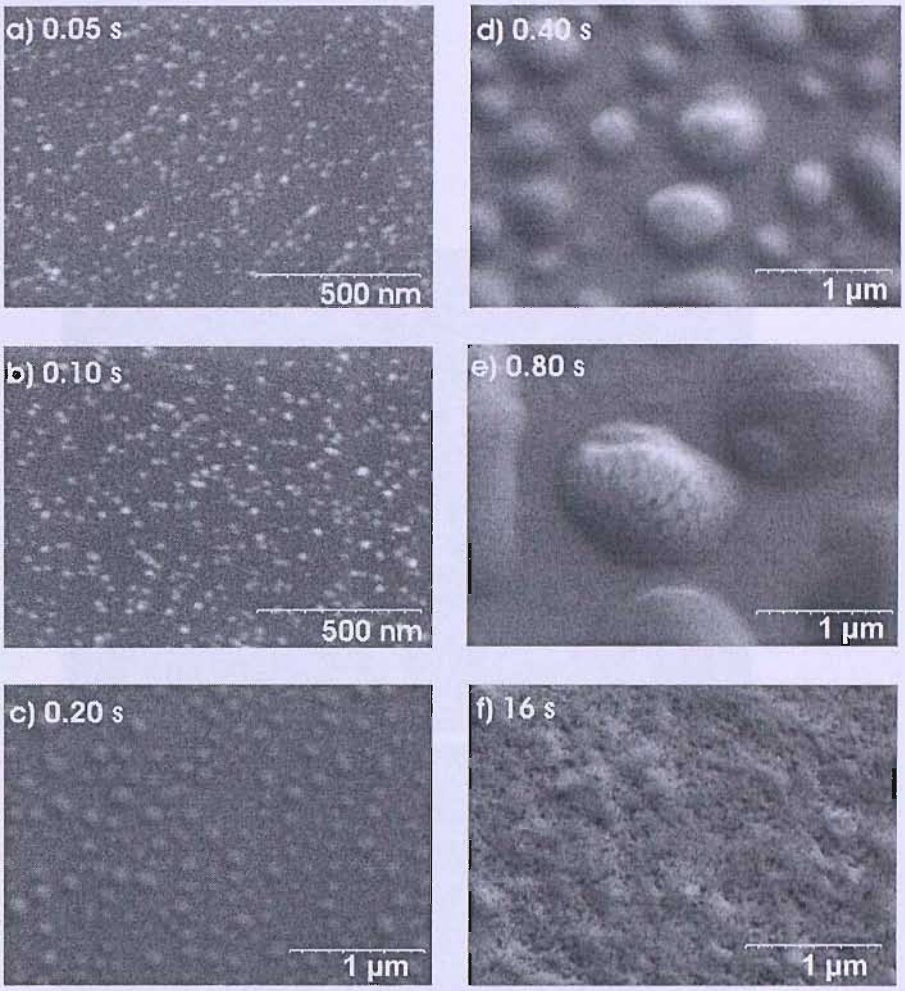

Figure 3.12: *SEM images of step-by-step Ni nucleation and growth on Si.*

Dendritic Growth

After nucleation is finished and a seed Ni layer has been formed, the Ni film growth takes place in a dendritic fashion. SEM images demonstrate this behaviour as shown in Fig. 3.13. Studies on the explanation of this growth mode can be found in the literature [125].

Roughness Control

Control of the roughness of the metallic films was achieved by varying the electrodeposition potential. Non-patterned Si samples were used for the electrodeposition of Ni films using constant electrochemical potentials from -1.1 V to -1.8 V which led to

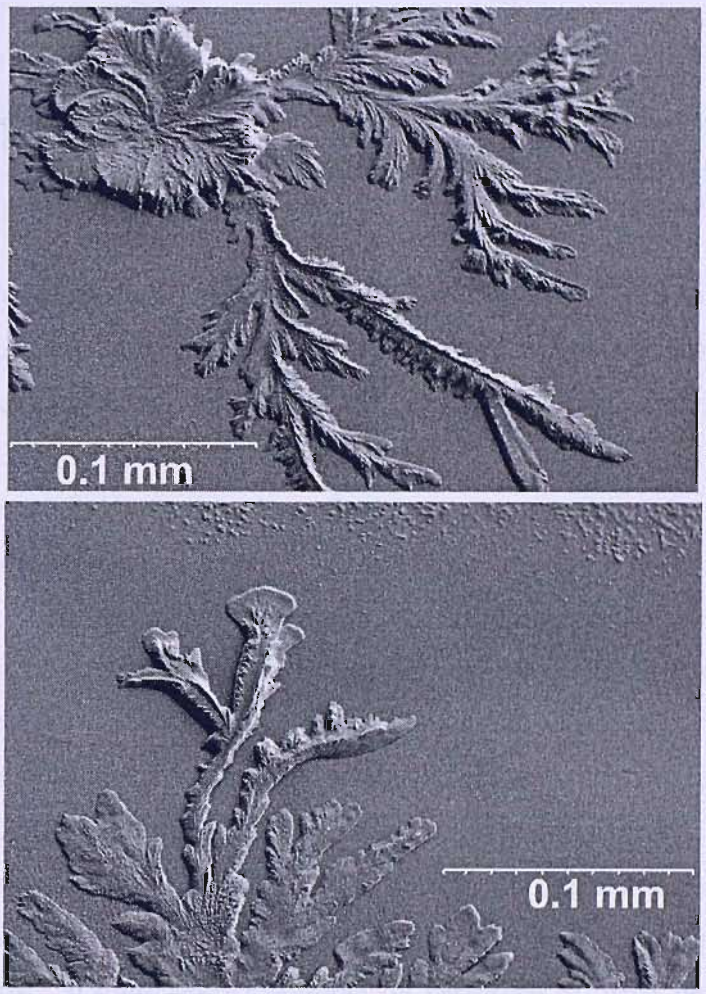

Figure 3.13: *Top-view SEM image showing dendritic growth of Ni on Si in the early stages of electrodeposition. The continuous background is the Si surface. The flower-like features grown on Si are electrodeposited Ni.*

Electrodeposition Potential (V)	RMS Roughness (nm)	Coercivity (Oe)
-1.1	17.9	74.9
-1.3	15.2	70.8
-1.4	19.1	76.9
-1.6	237	80.1
-1.8	608	87.2

Table 3.3: *Electrodeposition potential, surface and magnetic properties correlation. The thickness of the films was around 300 nm.*

different electrodeposition rates. The surface of the resulting films was characterised using optical microscopy and AFM. The correlation between the electrodeposition potential and the RMS roughness of the films, as measured with AFM, is shown in table 3.5.3.

The smoothest surfaces and smallest grains were achieved for the potential of -1.3 V. Lower absolute potential values could not provide a uniform electrochemical nucleation, resulting in increased roughness. Higher absolute potential values lead to very fast film growth giving even rougher and intensively dendritic surfaces with high spikes.

Further reduction of the surface roughness was achieved by applying pulsed electrochemical pretreatment of the Si surface before the film deposition stage. As the electrochemical nucleation rate is proportional to the applied current density, a high, short duration pulse just before electrodeposition leads to smoother Ni layers. AFM images of two Ni films electrodeposited on patterned Si using pulsed pretreatment and cyclic voltammetry are shown in Fig. 3.14. A pulse of -1.5 V for 0.2 s gave films with 37.1 nm RMS roughness whereas a pulse of -1.7 V for 0.4 s gave a much smoother film of 7.1 nm RMS roughness.

3.5.4 The role of buffered HF treatment

It must be emphasised that the BHF pretreatment before electrodeposition is a very critical step of the fabrication method presented here. This is because the native

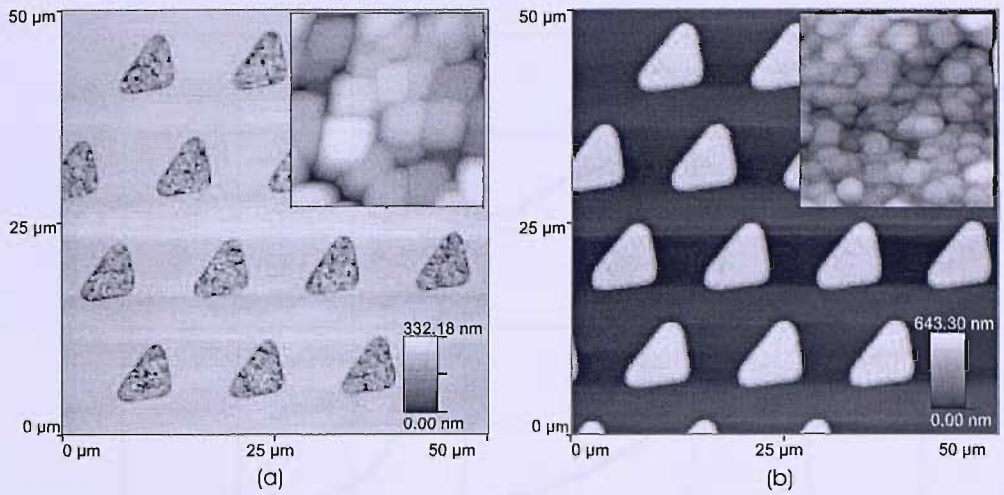

Figure 3.14: *AFM images of Ni electrodeposited on patterned Si showing roughness reduction by using electrochemical pulse pretreatment: (a) 1.5 V for 0.2 s, (b) 1.7 V for 0.4 s. In the insets, AFM scans of 2 µm by 2 µm surface areas are presented.*

oxide on the Si surface disturbs the Ni nucleation on Si and should be removed before electrodeposition. Most of the studies found in the literature carry out the BHF treatment shortly before electrodeposition [113, 119, 126, 127]. It is noted that BHF not only etches the native oxide but it leaves the Si surface H-terminated, preventing its reformation [128].

3.5.5 Magnetic Properties

Magnetic measurements were performed using a Vibrating Sample Magnetometer (VSM) to investigate the impact of the surface morphology on the magnetic properties of the Ni films. A typical hysteresis loop from a 300 nm thick Ni film electrodeposited on Si is illustrated in Fig. 3.15. Table 3.5.3 shows correlation among the electrodeposition potential, the root-mean-square (RMS) roughness, and the coercivity values.

The coercivity increases with the surface roughness, in good agreement with other reports on similar magnetic films [112]. This effect can be attributed to roughness induced domain wall pinning contributions to coercivity [129]. From magnetisation measurements the film thickness was calculated to be 300 *nm*. The charge corre-

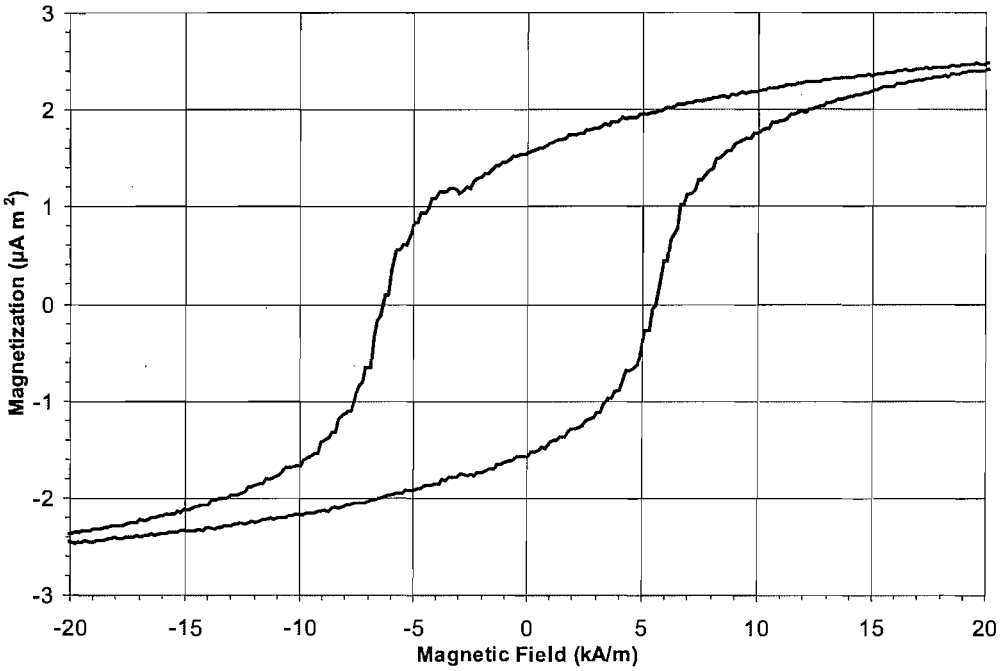

Figure 3.15: *Vibrating Sample Magnetometer measurements showing the hysteresis loop of a 300 nm thick Ni film electrodeposited on Si.*

sponding to this Ni mass revealed that 10% of the charge reaching the Si substrate during electrodeposition was due to hydrogen evolution, giving a current efficiency of $\alpha = 0.9$. These considerations allowed the control of the Ni films thicknesses, as discussed in section 3.3.2.

3.6 Conclusions

The results presented and discussed in this chapter reveal that electrodeposition of magnetic materials directly on n-type Si without a seed layer or back contact is possible. BHF treatment of the Si surface just before electrodeposition is vital for the process. The Si doping concentration directly affects the voltage drop along the Si electrode and hence reduces the electrodeposition current. This result is in excellent agreement with a theoretical model for current flow through semiconductors. Successful electrodeposition for Si resistivities up to 10-20 Ω cm is possible. Elec-

trodeposition is compatible with other microelectronics processes such as lithography as demonstrated by selective electrodeposition on Si/SiO_2 patterns. The roughness and the coercivity of the electrodeposited films can be correlated to controllable electrodeposition conditions.

Chapter 4

Guided Self Assembly of Inverse sphere magnetic nano-arrays on Si

Patterned recording media have been suggested to overcome thermal instability at data storage densities over 10 Gbit per cm^2. Such patterns have to be on the nanometre scale. Here, a review of self-assembly techniques for the fabrication of magnetic nanostructures is presented. Polystyrene latex sphere self-assemblies are used as templates for the fabrication of inverse sphere magnetic arrays electrodeposited directly on Si. This method is unique for defining 3-dimensional structures on the nanoscale. Lithographic patterns on Si guide the self-assembly along particular directions and better the long-range order. It is shown that size commensurability between the etched tracks and the spheres is critical for the long range ordering of the spheres. Non-commensurate guiding results in reproducible periodic triangular distortion of the close packed self-assembly. The alignment of self-assembly arrays on both sides of a guiding line is achieved and used for enhancement of the long range order of inverse sphere magnetic arrays.

Partly published in J. App. Phys., **100**, 113720, 2006. and to be published in J. Magn. Magn. Mater. Accepted, 2006.

4.1 Introduction

Nano-patterned magnetic materials are very attractive for fundamental studies on magnetism and applications such as patterned storage media and spintronic devices. However, the limitations of conventional lithography and the high cost of e-beam lithography limits widespread applications in this field. To overcome these restrictions, self-assembly has been widely proposed as an alternative technique. Self-assembly is the autonomous organisation of components into patterns or structures without human intervention [130]. Such structures can be used as templates to transfer the pattern to magnetic materials. A variety of natural systems with self-assembly properties has been used for this purpose including lyotropic liquid crystals [131], anodised alumina membranes [132], block copolymers [133] and close packed arrays of polystyrene latex and silica spheres [134, 135].

While these systems provide well-ordered, short range periodic templates, they lack long-range order and the ability to determine the precise position and direction of the periodic structure. In order to address these issues, guiding of the self-assembly has been proposed. This is a hybrid method involving pre-patterning of the substrate using conventional fabrication techniques to assist the self-assembly process. Guided block copolymer self-assembly has been studied showing remarkable guiding effects [136] and lithographically defined patterns have been used to aid close packed spheres self-assembly [137–142].

In comparison with block copolymers, close-packed sphere self assembly techniques are significantly different as they can produce arrays of 3-Dimensional (3D) magnetic spherical structures in dimensions not accessible by any other means. Block copolymer techniques do not allow control of the shape of the nano-structures [143]. Furthermore, the pattern transfer process is considerably simpler for spheres, as it doesn't involve any intermediate materials. Finally, while both techniques can be used to fabricate isolated magnetic dots or pillars [143–146], nano sphere lithography has the unique advantage of creating inverse sphere structures [134].

In addition to the aforementioned differences, the elastic response of block copolymers to patterned substrates results in a different guiding behaviour compared with

that of the close packed spheres. While block copolymers adjust their period to match the width of the pattern [136], spheres have an almost inelastic behaviour. Therefore, guidance has to be studied separately for these two techniques.

The combination of lithographic patterns and self-assembly of spheres has been studied and the importance of size commensurability between the patterns and the spheres has been recognised [147, 148]. However, no close-packed sub-micrometre sphere arrangements have been achieved and no systematic variation of the sphere arrangements with commensurability was detected. Furthermore, such hybrid structures have not yet been exploited for the fabrication of nanoscale magnetic structures.

In the work presented in this chapter, guides for sphere self-assembly are designed and used to manipulate the type and quality of the sphere order. Original theoretical considerations on the appropriate guide geometry for sphere self-assemblies are presented in section 4.2. Based on the outcome of this analysis a lithographic mask to study guiding effects has been designed. A description of this mask is presented in Appendix B (Mask KB73R). Details of the experimental method are given in section 4.3. Finally, experimental results on the effects of commensurability, the pattern transfer process and the alignment of arrays for long range self-assembly are presented.

4.2 Lithographic design for latex spheres guiding

The four main possible sphere packing structures will be initially reviewed in this section. The appropriate lithographic pattern dimensions for n columns of hexagonally self-assembled sphere monolayers in stripes are calculated next. The case of equilateral triangle patterns is also studied. Finally, the undesired pattern widening caused by BHF pretreatment before latex sphere confinement is calculated.

4.2.1 Regular Arrangements of Latex Spheres

The confinement of latex spheres on a surface is generally random. By using special deposition techniques though, one can achieve local ordering of the spheres structure. This means that there will be areas of uniformly and regularly deposited spheres.

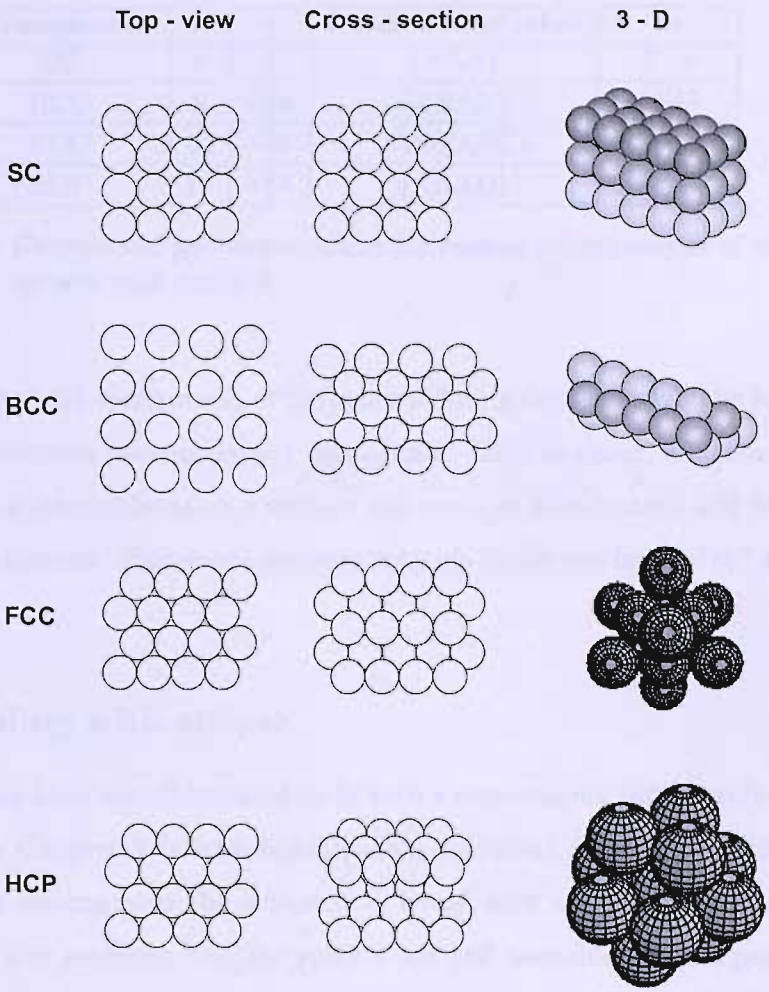

Figure 4.1: *Top-view, cross-section and 3D illustration of different sphere arrangements.*

The four basic regular arrangements of spheres are Simple Cubic Packing (SC), Body Centred Cubic Packing (BCC), Face-Centred Close Packing (FCC) and Hexagonal Close Packing (HCP). A graphic illustration of these arrangements is show in Fig. 4.1.

In order to compare such arrangements, the following characteristics are taken into account. Each sphere is in contact with n other spheres. The packing density η is defined as the occupied space per unit volume. The layer orientation is described with a series of letters with each letter corresponding to a uniquely aligned layer (e.g.: ABCDABCDABCD...), and with the distance b between two closest vertically aligned layers. These characteristics for the aforementioned arrangements are summarised in table 4.1, for spheres with radius r.

Arrangement	n	η	Layer Orientation	b
SC	8	$\frac{\pi}{6}$	(AAA)	$2 \cdot r$
BCC	8	$\frac{\sqrt{3}\cdot\pi}{8}$	(ABAB)	$\frac{4\cdot\sqrt{3}\cdot r}{3}$
FCC	12	$\frac{\sqrt{2}\cdot\pi}{6}$	(ABCABC)	$2 \cdot \sqrt{6} \cdot r$
HCP	12	$\frac{\sqrt{2}\cdot\pi}{6}$	(ABAB)	$\frac{4\cdot\sqrt{6}\cdot r}{3}$

Table 4.1: *Geometrical parameter values for regular arrangements of latex spheres with radius r.*

Assuming that the confinement of the spheres during deposition will be such that, in general, a maximum packing density will be most likely to occur, it comes out that the deposition of latex spheres on a surface will result in face-centred and hexagonal close packed structures. These arrangements coincide if only one layer of self-assembly is considered.

4.2.2 Guiding with stripes

Guiding patterns have been fabricated on Si with a conventional lithographic method as described in Chapter 2 (electrodeposition on patterned Si). It is assumed that during the wet etching step the side-etch is linear with an angle ϕ, as shown in Fig. 4.2. It is also assumed that the spheres are self assembled in the patterns in a hexagonal orientation, in parallel with the stripe. A top view of the hexagonal confinement of the spheres is given in Fig. 4.3a. The appropriate stripe width for the confinement of precisely n columns of spheres will be calculated. A close up of the geometry at the edge, where the spheres touch both the Si and the SiO_2 is illustrated in Fig. 4.3b. It will be:

$$\tau = 2r \cdot tan\frac{\phi}{2} \tag{4.1}$$

The appropriate stripe width for n sphere columns will then be given by:

$$W_p = 2r \cdot [(n-1) \cdot sin\theta + tan\frac{\phi}{2}] \tag{4.2}$$

with $\theta = 60^o$. Theoretically, the edge angle for wet etching should be 45^o. However, AFM measurements such as that shown in Fig. 4.4 revealed that typical values

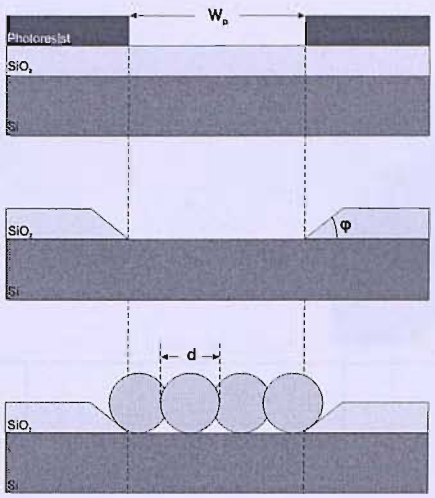

Figure 4.2: *Self assembly of latex spheres in stripes (cross section).*

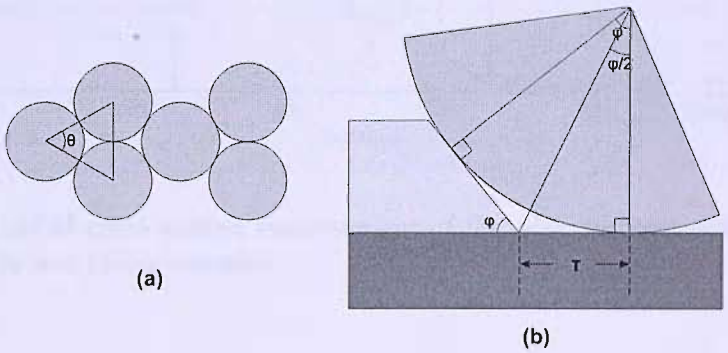

Figure 4.3: *(a) Top view of hexagonal close packed self assembly of latex spheres. (b) Edge geometry of a stripe filled up with a sphere self-assembly.*

of the edge angle ϕ for the fabricated patterns are between 20^o and 30^o. This applies to a SiO_2 thickness of 250 nm.

For sphere size of 500 nm (diameter), from equation 4.2 the numerical data shown in table 4.2 are obtained. The same data are graphically plotted in Fig. 4.5. Note that the effect of angle ϕ is small and hence not visible in the plot.

4.2.3 Guiding with equilateral triangles

In the case of using equilateral triangular patterns for guiding the sphere self assembly, the vertices will look as shown in Fig. 4.6a.

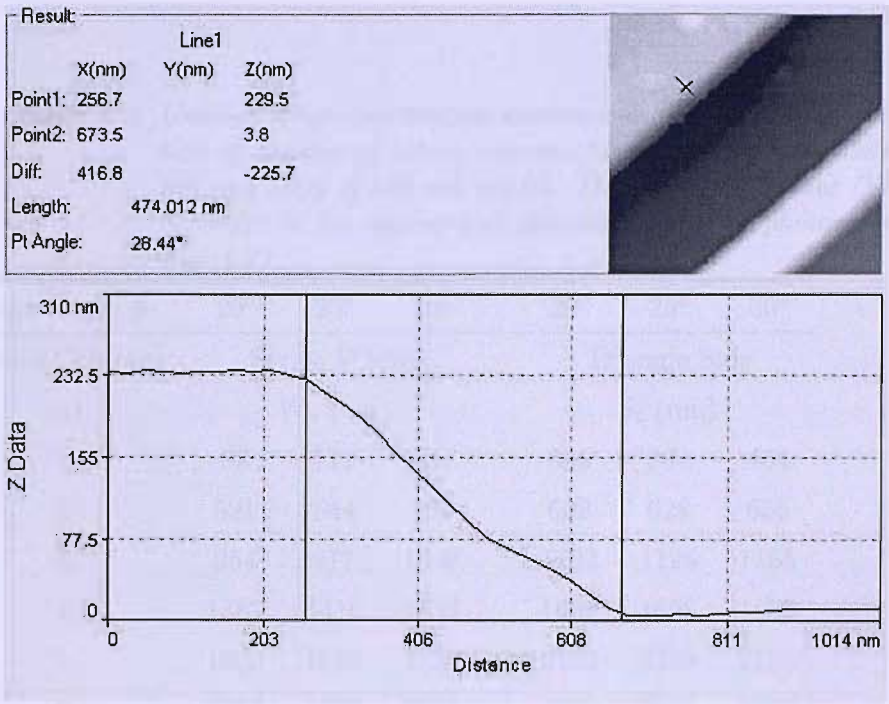

Figure 4.4: *AFM cross section measurement of the edge gradient obtained by wet etch processing.*

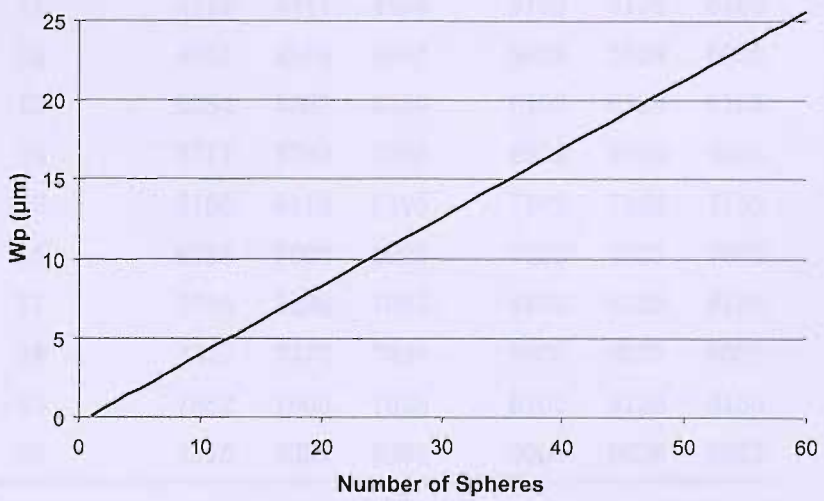

Figure 4.5: *Guiding stripe width as a function of number of sphere columns.*

Table 4.2: *Guiding stripe and triangle commensurate dimensions as a function of number of sphere columns for spheres with diameter 500 nm and SiO_2 of 250 nm height. The calculated values (W_p and S_t) refer to the appropriate dimensions on the photoresist (see Fig. 4.2).*

Edge Angle ϕ:	20^o	25^o	30^o	20^o	25^o	30^o
Sphere Columns	Stripe Width			Triangle Side		
(n)	W_p (nm)			S_t (nm)		
1	88	111	134	305	384	464
2	521	544	567	602	628	655
3	954	977	1000	1102	1128	1155
4	1387	1410	1433	1602	1628	1655
5	1820	1843	1866	2102	2128	2155
6	2253	2276	2299	2602	2628	2655
7	2686	2709	2732	3102	3128	3155
8	3119	3142	3165	3602	3628	3655
9	3552	3575	3598	4102	4128	4155
10	3985	4008	4031	4602	4628	4655
11	4418	4441	4464	5102	5128	5155
12	4851	4874	4897	5602	5628	5655
13	5284	5307	5330	6102	6128	6155
14	5717	5740	5763	6602	6628	6655
15	6150	6173	6196	7102	7128	7155
16	6583	6606	6629	7602	7628	7655
17	7016	7039	7062	8102	8128	8155
18	7449	7472	7495	8602	8628	8655
19	7882	7905	7928	9102	9128	9155
20	8315	8338	8361	9602	9628	9655

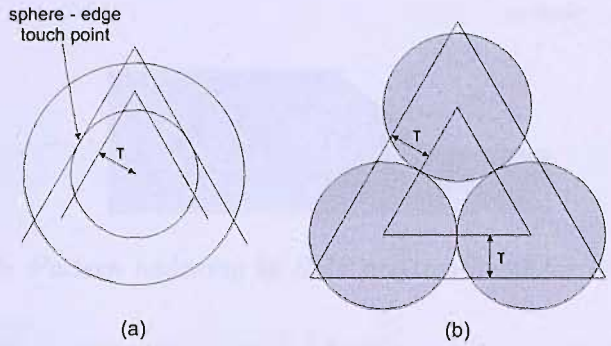

Figure 4.6: *(a) Sphere confinement at a vertex of a triangular pattern (top-view). (b) Top-view illustrating the distance between the lithographically patterned triangle and the triangle formed by the centres of the self-assembled spheres.*

The distance τ is given by equation 4.1. In order to calculate the appropriate triangle size for the confinement of n spheres, the difference between the lithographically patterned triangle and the triangle formed by the centres of the spheres should be taken into account. This difference is illustrated in Fig. 4.6b. The difference of the triangle height is τ, giving a side difference of:

$$a_{pattern} - a_{spheres} = \frac{2 \cdot \sqrt{3}}{3} \cdot \tau \tag{4.3}$$

Setting n to be the number of spheres confined along one side it will be:

$$a_{spheres} = (n-1) \cdot 2r \tag{4.4}$$

$$a_{pattern} = (n-1) \cdot 2r + \frac{2 \cdot \sqrt{3}}{3} \cdot \tau \tag{4.5}$$

Substituting τ from equation 4.1, the formula giving the lithography triangle size needed for the confinement of n sphere along the side becomes:

$$S_l = a_{pattern} = 2r \cdot (n - 1 + \frac{2 \cdot \sqrt{3}}{3} \cdot \tan\frac{\phi}{2}) \tag{4.6}$$

For sphere size of 500 nm (diameter), from equation 4.6 the numerical data shown in table 4.2 are obtained (triangle side).

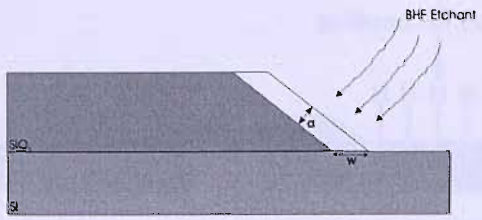

Figure 4.7: *Pattern widening by BHF pre-treatment for sphere deposition.*

4.2.4 BHF pretreatment widening

The effect of the surface pre-treatment before spheres deposition to the lithographically defined patterns is illustrated in Fig. 4.7. The widening (one side) will be given by:

$$w = \frac{a}{sin\phi} \tag{4.7}$$

where ϕ is the angle of the pattern walls. For adjusting the size of stipes, w should be doubled to take into account this effect at both sides. For the case of triangles w should be multiplied by the factor:

$$f_{triangle} = \frac{2}{3} \cdot (3 + \sqrt{3}) \tag{4.8}$$

4.3 Experimental Conditions

A description of the fabrication process is illustrated in Fig. 4.8. N-type ⟨100⟩ single-side polished silicon wafers with resistivity 0.01-0.02 Ω cm were used as substrates (Fig. 4.8a). A 250 nm thick layer of SiO_2 was thermally grown on the front side (Fig. 4.8b) and photoresist was spun on top (Fig. 4.8c). Guiding stripes with thicknesses ranging from 1.1 μm to 12 μm were transferred to the photoresist from an optical mask using a Nikon NSR-2005/i9C step and repeat system. (Fig. 4.8d). Subsequently, the wafers were immersed in a 20:1 Buffered Hydrogen Fluoride (BHF) solution which etched the oxide and exposed the Si at the selected areas, followed by a fuming nitric acid clean to remove the photoresist (Fig. 4.8e). Then, the wafers were sawn to pieces and cleaned using an aqueous mixture of hydrogen peroxide and

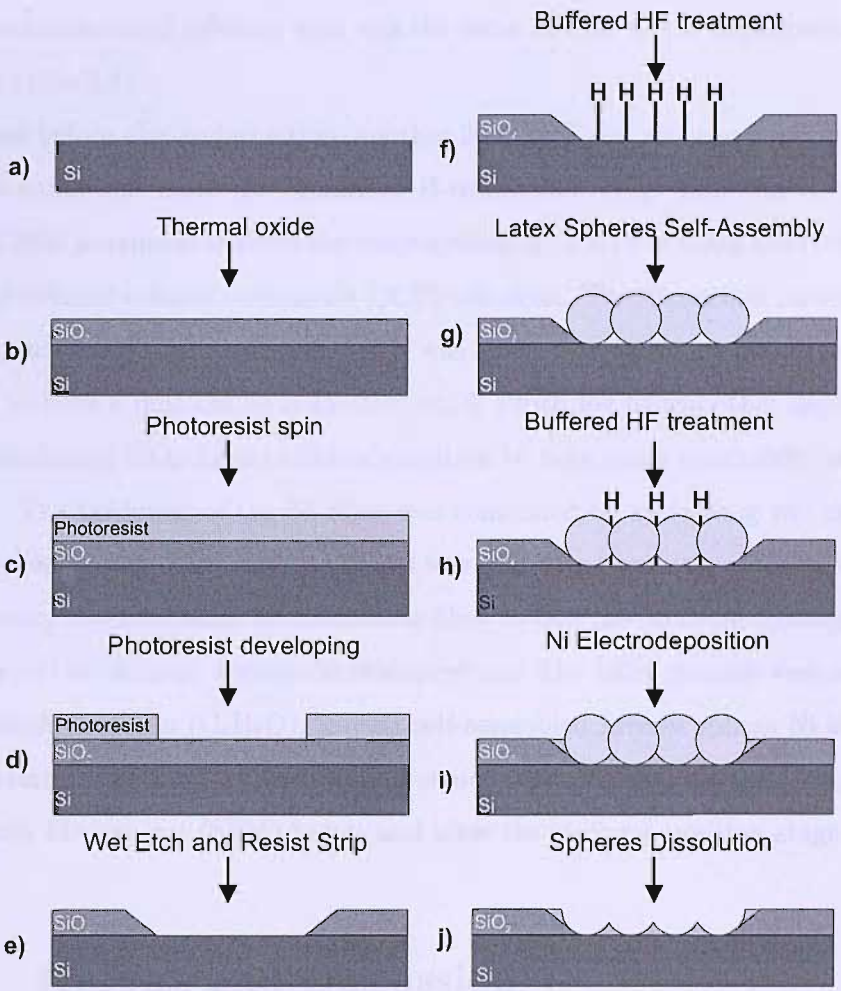

Figure 4.8: *Process flow for guided self-assembly of inverse sphere magnetic arrays.*

ammonium hydroxide and a mixture of hydrogen peroxide and HCl (RCA Clean).

A 20:1 BHF dip followed, leaving the Si surface H-terminated and hence, hydrophobic. Shortly after (typically a few hours), negatively charged, unmodified, 500 nm diameter latex spheres were self-assembled on the substrates by slow evaporation of a colloidal water suspension containing 1wt. % of spheres. The sphere solution was purchased from Duke Scientific Corporation. In most of the cases, trapping of the spheres into the morphological patterns of the substrate resulted in selective sphere self-assembly on Si.

Electrodeposition through the self-assembly of the latex spheres was used to grow inverse sphere Ni arrays directly on Si without a back contact. The composition of

the electrochemical solution used was the same as that of the experiments of chapter 3 (see table 3.1).

Just before electrodeposition, another 20:1 BHF dip was necessary to remove the native oxide and leave the Si surface H-terminated (Fig. 4.8h and i). An Autolab AUT72032 potentiostat three electrode system with a Pt counter electrode and a saturated calomel reference electrode (SCE) was used. The deposition potential was -1.1 V (against the SCE). A pulse of -1.5 V was applied for 0.2 s just before the deposition stage to form a uniform Ni nucleation on Si which led to smoother deposition [149]. The insulating SiO_2 forced electrodeposition to take place selectively on the Si patterns. The thickness of the Ni films was controlled by measuring the charge during electrodeposition. This control process was calibrated against vibrating sample magnetometry measurements on continuous films to take into account hydrogen evolution effects at the cathode during electrodeposition. The latex spheres were dissolved using tetrahydrofuran (C_4H_8O), leaving self-assembled inverse sphere Ni arrays on the Si patterns (Fig. 4.8j). The resulting structures were characterised using Scanning Electron Microscopy (SEM) before and after the electrodeposition stage.

4.4 Results and Discussion

4.4.1 Commensurability between guiding patterns and spheres

When a colloidal solution of latex spheres is left to evaporate on a surface, strong attractive capillary forces among the spheres tend to maximise the density of the remaining structure [150]. Since the maximum sphere density is achieved by close packing [151], this mechanism leads to self-assembled face-centred or hexagonal close packed multi-layers. By adjusting the amount of the colloidal solution, close-packed monolayers can also be fabricated. In this manner, self-assembly monolayers of latex spheres with no guidance on SiO_2 were prepared as shown in Fig. 4.9. These structures typically have a uniform orientation for lengths more than 10 μm. However, the unrestricted deposition area permits the spheres to shift and create fractures.

Self-assembly monolayers of latex spheres guided by 12 μm and 6 μm stripes

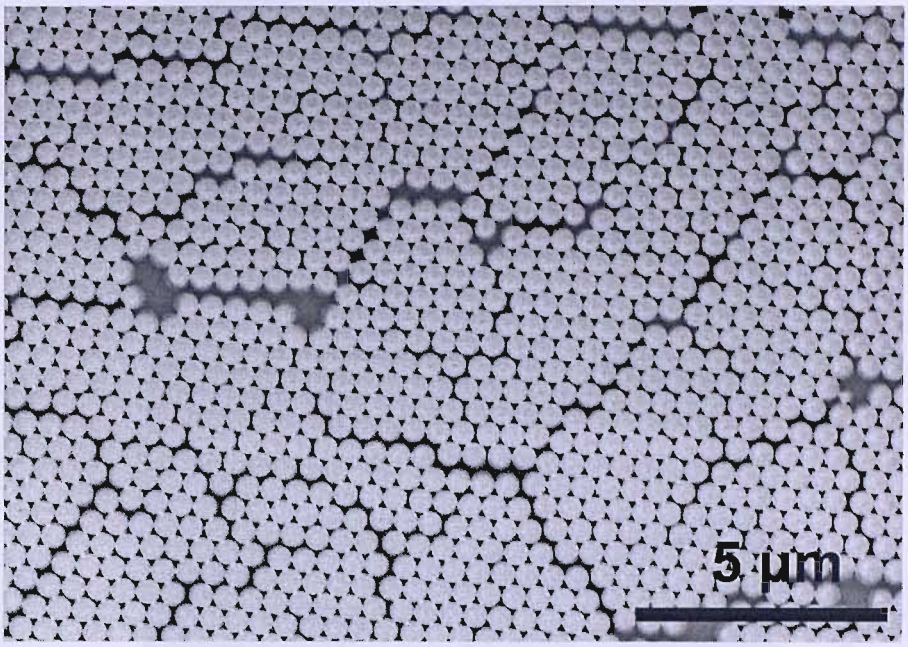

Figure 4.9: *SEM image of self-assembled latex spheres without guiding. The arrangement is hexagonal and has a uniform orientation, but severe fracturing occurs.*

are shown in Figs. 4.10a and b respectively. The sphere deposition technique was the same as that used in the case of Fig. 4.9. Improvement of the self-assembly is observed with one discrete defect in an area of 10 x 12 μm. One of the axes of the hexagonal structures is aligned with the edges of the guiding structures, demonstrating the ability to predetermine the orientation of the self assembly.

Furthermore, Fig. 4.10 shows selective sphere deposition on the hydrophobic Si surface rather than on the hydrophilic SiO_2. This result contradicts studies reported in the literature showing strong preference for deposition on hydrophilic surfaces [152]. It suggests domination of the sphere trapping mechanism in the morphological patterns [147] over hydrophobic/hydrophilic effects. It must be noted however that in cases where large amounts of colloidal suspension were used, indiscriminate self-assembly of latex spheres throughout the substrate was observed. These extra spheres on the oxide do not affect the Ni deposition and they are removed by the solvent which removes the spheres from the Ni film.

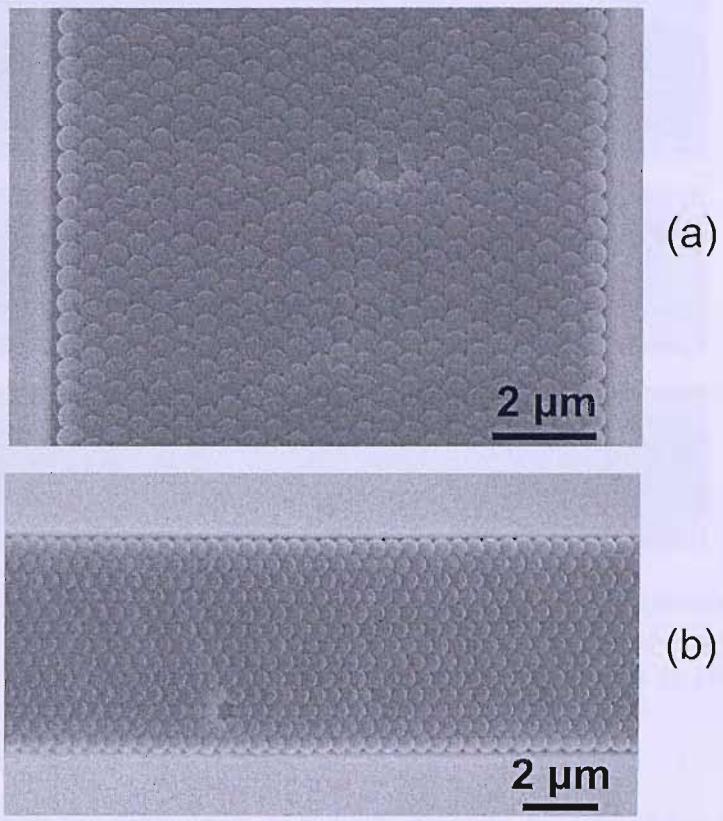

Figure 4.10: *SEM image of self-assembled latex spheres guided by a 12 µm (a) and a 6 µm (b) wide Si/SiO_2 stripe. The close packing of the spheres is aligned to the guiding edges. The missing sphere represents the state-of-the-art defect rate of the self-assembly technique.*

It is apparent from the left edge of the pattern in Fig. 4.10 that the self-assembly does not abut against the sides of the guiding stripe. This is because the size of the stripe is not commensurate with the diameter of the spheres. After the electrodeposition step, these non-patterned spaces would result in continuous magnetic stripes at the sides of the inverse sphere array. Such imperfections would not always be desirable. More importantly, in some cases this mismatch results in low quality guiding. The sphere arrays can move in the patterns deviating from the desired orientation and create fractures. An example of such effects is shown in Fig. 4.11 These possibilities make it difficult to achieve good quality structures in non-commensurate cases.

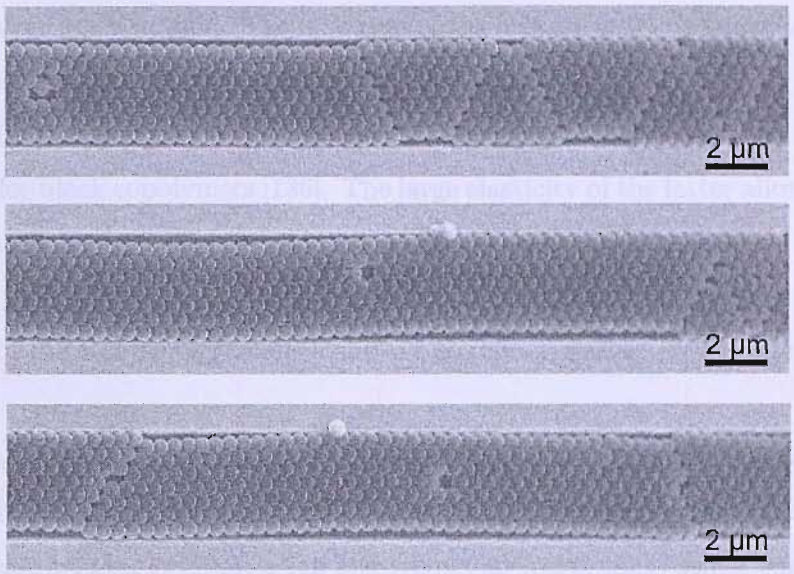

Figure 4.11: *SEM image of long arrays of self-assembled latex spheres guided by 5 μm stripes. The size of the spheres is not commensurate with the width of the stripes, causing the arrays to float and resulting in defects.*

In order to study the dependence of the self-assembly process on the size of the guiding patterns, stripes with various widths were fabricated. In Fig. 4.12a, a stripe with a width of 3.7 μm is used to guide the sphere self-assembly. The stripe is too big for a sphere array of 7 rows and too small for 8 rows. The demand of maximum density imposes a structure of 7 rows with trigonal symmetrical fractures. Such a structure embodies two levels of self assembly. One of close packed spheres at the sphere level (500 nm) and one of equilateral triangles at the grain level (7 spheres-a-side or 3.5 μm). In Fig. 4.12b, a stripe with a width of 3.9 μm is used. This size is commensurate with a close packed sphere array of 8 rows and hence it works as a perfect guide. Similarly, in Fig. 4.12c, a stripe with a width of 4.2 μm is used. The stripe is too big for an array of 8 rows and too small for 9 rows. The demand of maximum density imposes a dual self assembly structure of 8 rows with trigonal symmetrical fractures. The equilateral triangles are 8 spheres-a-side or 4 μm. Lastly, in Fig. 4.12d, a stripe with a width of 4.3 μm is used. This size is commensurate with a close packed sphere array of 9 rows and perfect guiding is achieved. Note that in this case, spheres are also observed on the SiO_2 as a result of the large amount of

colloidal suspension used. The guidance of the pattern extends onto the SiO_2 because the spheres are twice the height of the SiO_2 thickness.

The above results on incommensurate guiding are very different from those reported for block copolymers [136]. The large elasticity of the latter allows deformation to fit the guided pattern. In contrast, the hard nature of latex spheres imposes direct control of the sphere packing arrangement by the size of the guiding patterns. The period of the structures remains constant as predetermined by the size of the spheres used.

These results demonstrate the ability to fabricate perfectly guided sphere self-assembly arrays by tailoring the size of the guiding structure. Moreover, on-demand dual (close packing crystallisation and triangular fractioning) self-assembly structures can be constructed. The number of spheres per triangle is controlled by the size of the stripe. Although non-commensurability complicates guidance and increases the sensitivity of the fabrication process the resulting structures are very interesting. The reproducible fabrication of regular defects in the close packed sphere symmetry can prevent certain light frequencies from being transmitted. This attribute, often called photonic band-gap, is very promising for photonic crystal applications [153, 154].

4.4.2 Metallisation

Commensurately guided close packed sphere arrays as described in section A were used to fabricate inverse sphere magnetic arrays on Si, as shown in Fig. 4.13. The array thickness was 250 nm (half the diameter of the spheres) to allow observation of the inverse sphere structure. Ni electrodeposition occurs only on Si and not on the insulating SiO_2, resulting in confinement of the magnetic arrays exclusively to the Si patterns. The sphere template pattern has been transferred to the Ni layer without defects. In Fig. 4.13a, Ni arrays guided by 1.3 μm wide stripes are shown. Good commensurability between the stripes and the spheres prevents the formation of uniform Ni lines at the sides of the array. In Fig. 4.13b, a Ni array guided by a 2.6 μm wide stripe is shown. The guiding stripe is slightly wider than the array resulting in very thin Ni lines at the edges. This result demonstrates the ability of on-demand

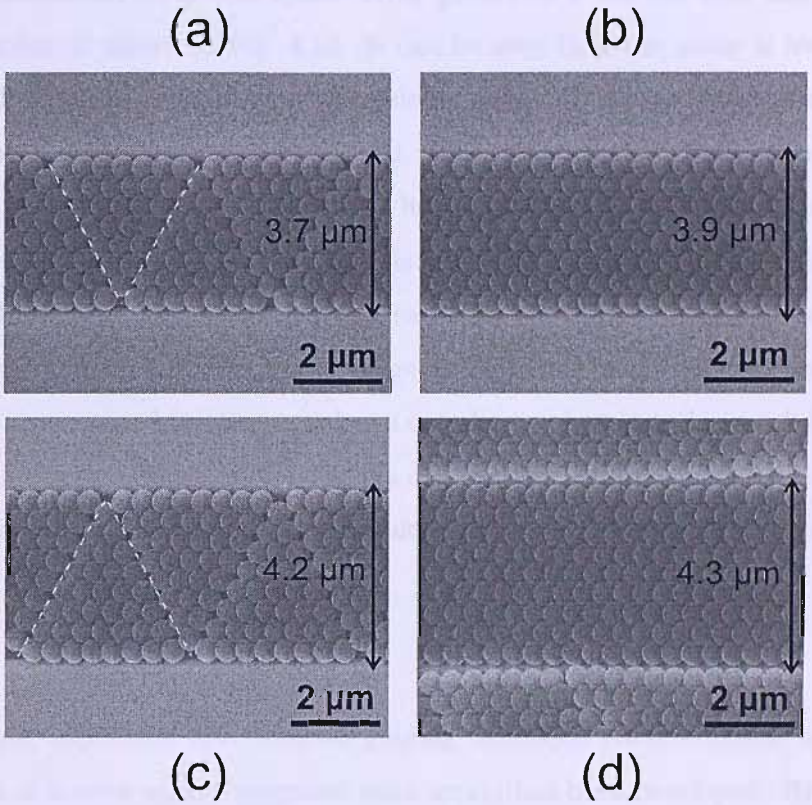

Figure 4.12: *In (a), an array of 7 rows of spheres is guided by a 3.7 μm wide stripe. This excessive width allows for a natural, triangular distortion of the array which increases the sphere density. In (b), an array of 8 rows of spheres is guided by a 3.9 μm wide stripe. The dimensional match results in a perfectly guided sphere array. Similarly, in (c) an array of 8 rows of spheres is guided by a 4.2 μm wide stripe resulting in a distorted array. In (d) an array of 9 rows of spheres is guided by a 4.3 μm wide stripe resulting in perfect guidance. Note that in (d) the spheres self-assembly is expanded to the SiO_2 region indicating that the spheres deposition process is not always selective.*

bordering of the inverse sphere magnetic arrays.

4.4.3 Long-range self assembly

A self-assembled Ni inverse sphere array guided by a 140 nm wide and 100 nm thick SiO_2 stripe is shown in Fig. 4.14. It can be seen that the array is free of fractures and it follows the orientation of the guiding stripe. Moreover, the phases of the array on either side of the stripe are aligned. This is accomplished by continuation of the sphere self-assembly over the stripe, lining up the two sides, as illustrated in the inset of Fig. 4.14. The self-assembly is hence not hampered by the lithographically defined guidance stripe, while at the same time it forces the orientation of the self-assembly creating therefore longer range ordering. Although some defects on the anti-sphere array caused by missing spheres can also be observed, this result is particularly important for patterned storage media as it reveals that long-range self-assembly can be achieved by lining-up a series of guided self-assembled magnetic arrays.

4.5 Conclusions

A simple, rapid and cost effective guiding technique for orientation and symmetry control of inverse sphere magnetic nano arrays has been developed. By tailoring the dimensions of the guiding patterns, switching between perfect and triangularly distorted close packed self-assembly symmetries is possible. Lining up of inverse sphere arrays was achieved by employing thin guiding lines, expanding the long-range order. These patterns were successfully transferred to the Ni layers by electrodeposition without observable defects. The results are promising for micromagnetic studies and applications such as patterned storage media and magnetoresistance devices. This fabrication technique could also be applied to nanoscale self-assembly arrays with customised symmetries for photonic crystals.

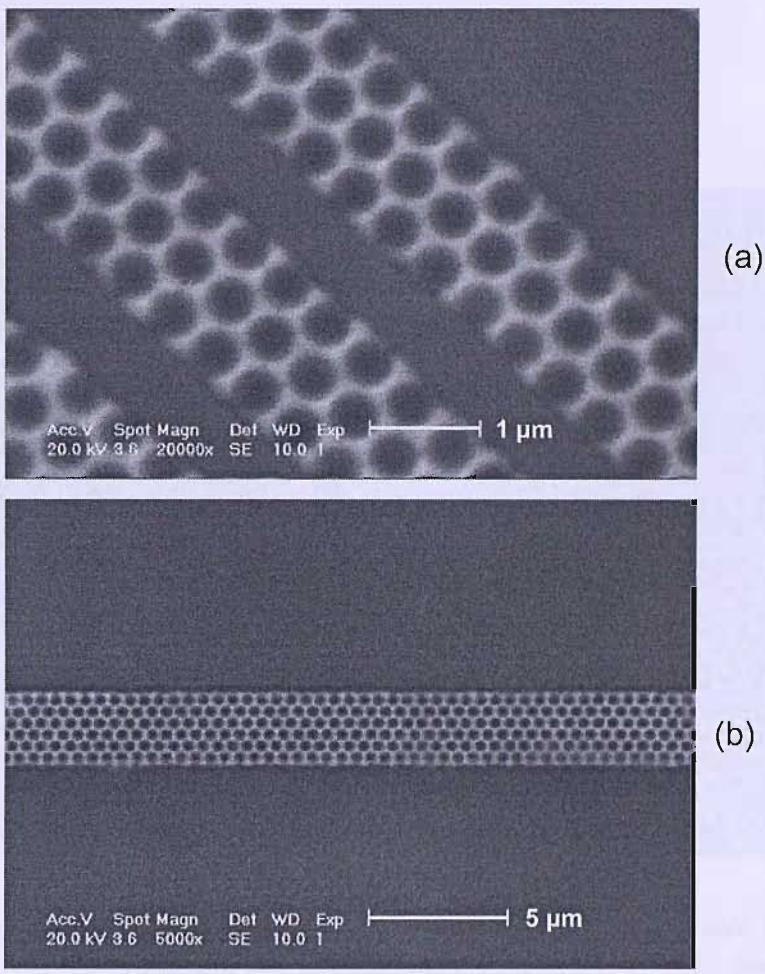

Figure 4.13: *SEM image of self-assembled inverse sphere Ni arrays guided by (a) 1.3 µm Si/SiO_2 and (b) 2.6 µm stripes. The uniform, black area is SiO_2 while the honeycomb-like, white structure is the surface of the Ni. The holes in the array correspond to the spherical Ni cavities with the Si bottom appearing black at the centres.*

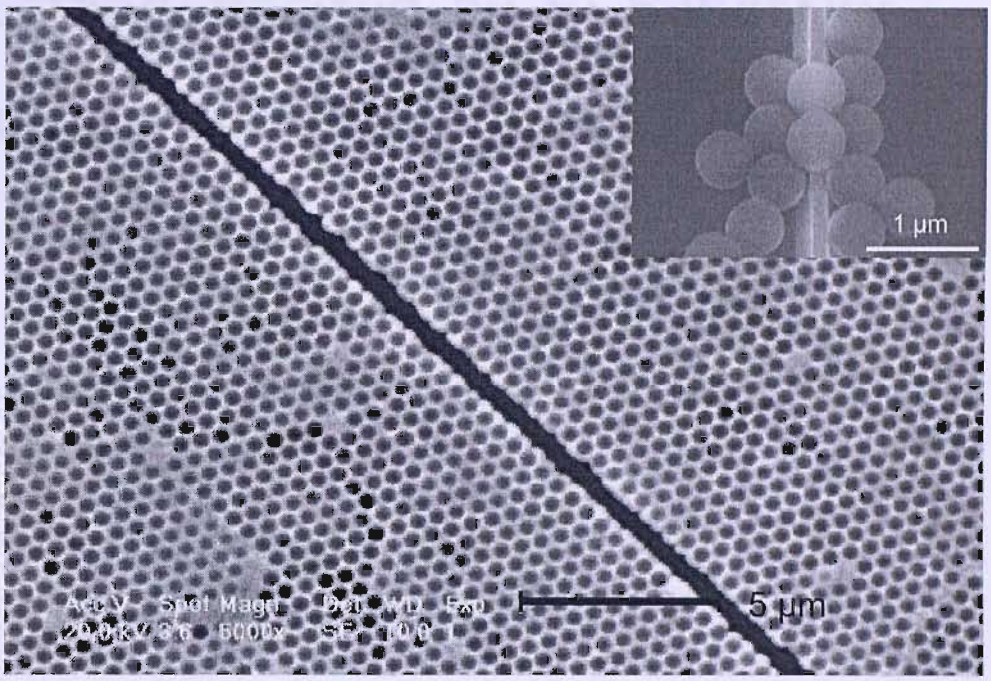

Figure 4.14: *SEM image of a Ni inverse sphere array, guided by a 140 nm wide and 100 nm high SiO2 stripe. In the inset, the mechanism of lining up the arrays at either sides of the stripe is demonstrated.*

Chapter 5

Electrodeposited Ni-Si Schottky barriers and magnetoresistance of Ni anti-sphere arrays

The Schottky barrier at magnetic metal-semiconductor interfaces is of particular importance for spin injection and detection and for suppressing substrate leakage currents at magnetoresistance devices grown directly on semiconductors. In this chapter a brief introduction to Schottky Barriers is given. The Schottky barrier at electrodeposited Ni-lowly doped Si contacts is characterised. A high quality rectifying behaviour is observed. The results are explained using modern Schottky barrier models taking into account a spatial distribution of the barrier height. Physical characterisation of the contact is also presented and taken into account for a consistent interpretation of the results. The Ni-Si Schottky barrier is used to suppress leakage currents and allow anisotropic magnetoresistance measurements in self-assembled magnetic anti-sphere arrays directly on Si.

This chapter is partly published in Sol. St. Comm., **140**, 508, 2006.

5.1 Introduction

Schottky barriers (SB) play an important role in recent advances of spintronics. Giant magnetoresistance multilayers have been grown by electrodeposition on Si substrates,

using the metal-Si SB to prevent shorting the circuit [111]. Spin valve and hot electron transistors have been fabricated using the Si Schottky barrier for collection of hot electrons [103, 155]. The latter devices, fabricated by physical vapour deposition, work only at low temperatures due to the high leakage of the barrier at room temperature. Considering these applications, it is surprising to know that little attempt has been made to characterise electrodeposited magnetic metal-Si SBs.

After a brief introduction to the Schottky barrier theory, the characterisation of the Schottky barrier formed at electrodeposited Ni-lowly doped Si contacts is presented. Physical characterisation of the Ni-Si interface by SEM and X-Ray Diffraction measurements is also included to ensure the correct interpretation of the electrical results. The rectifying behaviour of the Ni-Si contact is used to suppress leakage currents in magnetoresistance measurements performed in a self-assembled inverse sphere Ni array as described in the last section of this chapter.

The case of highly doped Si is also very interesting as it enables tunnelling currents which are particularly important for spin injection and detection in semiconductor spintronic devices. This case is presented in chapter 6.

5.2 Schottky Barriers

A brief introduction of the electrical behaviour of metal-semiconductor junctions is given in this section. This background is important for the interpretation of the experimental results of the fabricated Ni-Si SBs. Further details of metal-semiconductor contacts can be found in the literature [156–158].

When metal makes contact with a semiconductor a barrier is formed at the metal-semiconductor interface. The formation of this barrier can be explained with the energy band diagrams as shown in Fig. 5.1 for n-type semiconductors.

If there is no contact between the metal and the semiconductor there is a difference between the metal work function $q \cdot \phi_M$ and the Fermi level E_F of the semiconductor(Fig. 5.1a). The barrier height ϕ_B is defined as the potential difference between the metal work function and the semiconductor band edge where the majority carriers reside. If χ is the electron affinity and E_g is the band gap of the semiconductor

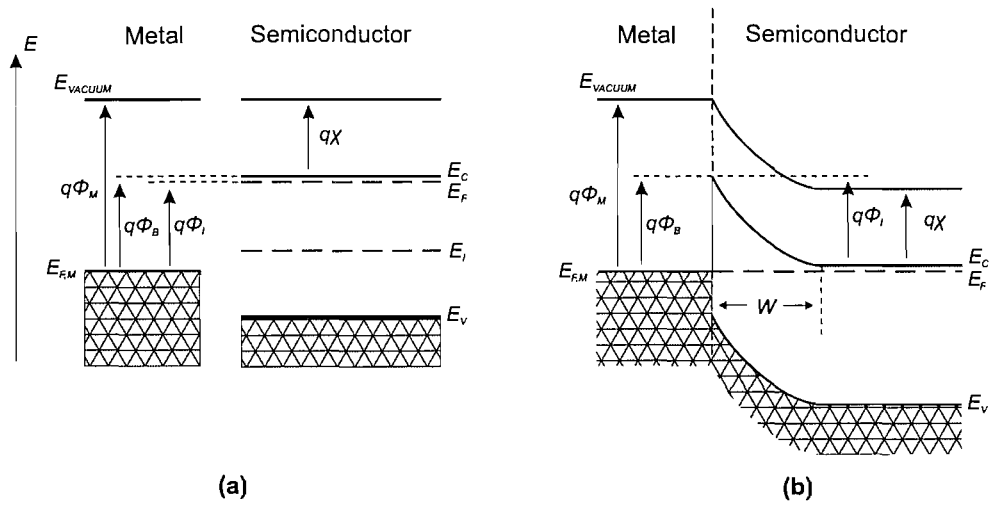

Figure 5.1: *(a) Flat energy band diagram and (b) Thermal equilibrium diagram of a metal-n-type semiconductor junction.*

then the barrier height for n-type and p-type semiconductors will respectively be:

$$\phi_{B,n-type} = \phi_M - \chi \tag{5.1}$$

$$\phi_{B,p-type} = \frac{E_g}{q} + \chi - \phi_M \tag{5.2}$$

The built-in potential ϕ_i is defined as the difference between the Fermi energy of the metal and that of the semiconductor:

$$\phi_{i,n-type} = \phi_M - \chi - \frac{E_c - E_{F,n}}{q} \tag{5.3}$$

$$\phi_{i,p-type} = \frac{E_g}{q} + \chi - \frac{E_{F,p} - E_v}{q} - \phi_M \tag{5.4}$$

When a metal and a semiconductor come to contact, their Fermi levels align to achieve thermal equilibrium. Electrons from an n-type semiconductor can lower their energy by traversing the junction. As the electrons leave the semiconductor, a positive charge due to the ionised donor atoms stays behind. This charge creates a negative field and lowers the band edges of the semiconductor. Electrons flow into the metal until equilibrium is reached between the diffusion of electrons from the

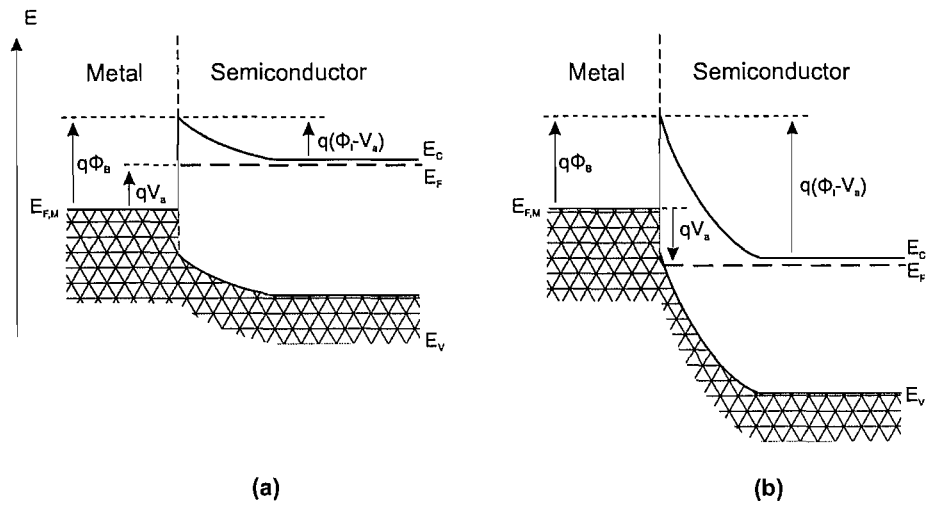

Figure 5.2: *Energy band diagrams of a metal - n-type semiconductor contact at (a) forward bias and (b) reverse bias. For simplicity, the vacuum level is omitted in these diagrams.*

semiconductor into the metal and the drift of electrons caused by the field created by the ionised donor atoms. The band diagram at thermal equilibrium is shown in Fig. 5.1b.

In thermal equilibrium there is a region in the semiconductor (W in Fig. 5.1b) which is depleted of mobile carriers. This region is called depletion region. For n-type semiconductors, the depletion region width is given by:

$$W = \sqrt{\frac{2 \cdot \epsilon_s}{q \cdot N_D} \cdot (\phi_i - V_a - \frac{k \cdot T}{q})} \tag{5.5}$$

At forward bias (positive bias to the metal) the Fermi level of the metal is lowered with respect to that of the semiconductor. At reverse bias the Fermi level of the metal is raised with respect to that of the semiconductor. The corresponding band diagrams are shown in Fig. 5.2.

The current across a metal-semiconductor junction is mainly due to majority carriers. There are four main current transport processes in metal-semiconductor contacts. The first assumes electron transmission over the potential barrier and can be explained by the thermionic emission and diffusion theory. The second involves quantum mechanical tunnelling through the barrier and is relevant to highly doped

semiconductors. The third and fourth mechanisms are the recombination processes at the depletion and the neutral region respectively.

The work presented in this chapter mainly involved moderately doped n-type Si. Therefore, tunnelling phenomena are excluded from the following analysis. Generation-recombination effects are also excluded as they are not expected to appear due to the high carrier lifetime of silicon [157].

5.2.1 Thermionic Emission Theory

If a homogeneous SB and a thermionic emission current transport mechanism are assumed [156, 159], the current density (J) will be given by:

$$J(V_a) = J_S \cdot (e^{\frac{q \cdot V_a}{k \cdot T}} - 1) \tag{5.6}$$

with saturation current density J_S:

$$J_S = A^* \cdot T^2 \cdot e^{-\frac{q \cdot \phi_{Bn}}{k \cdot T}} \tag{5.7}$$

where V_a is the applied potential, q is the elementary charge, k is the Boltzmann constant, T is the absolute temperature, A^* is the Richardson constant and ϕ_{Bn} is the SB height. In order to fit experimental data, an ideality factor n is introduced to equation 5.6 as:

$$J(V_a) = J_S \cdot (e^{\frac{q \cdot V_a}{n \cdot k \cdot T}} - 1) \tag{5.8}$$

5.2.2 Theoretical $C - V$ Characteristics

The theoretical expression for the capacitance C_a of a metal/n-type Si junction is [156]:

$$C_a = \sqrt{\frac{q \cdot \epsilon_s \cdot N_D}{2 \cdot (V_{bi} - V_a - \frac{k \cdot T}{q})}} \tag{5.9}$$

where ϵ_s and N_D are the permittivity and the doping concentration of the semiconductor, V_{bi} is the built-in potential and V_a is the applied potential. From equation 5.9,

the n-Si doping concentration as a function of the gradient of the inverse square capacitance per unit area can be derived:

$$N_D = \frac{2}{q \cdot \epsilon_s} \cdot (-\frac{dC_a^{-2}}{dV_a})^{-1} \tag{5.10}$$

Assuming a constant N_D throughout the depletion region of the junction, C^{-2} versus V_a should be a straight line. From the gradient of such a straight line the doping concentration of the semiconductor can be obtained. Moreover, a measure of the average Schottky barrier height of the junction can be determined from the intercept V_i of its extension on the voltage axis [156]:

$$\phi_{Bn} = V_i + V_n + \frac{k \cdot T}{q} \tag{5.11}$$

where V_n is the depth of the Fermi level below the conduction band. For inhomogeneous SB contacts models have been proposed to incorporate inhomogeneity effects [160]. The effect of such models on the analysis of our $C - V$ measurements is negligible and therefore they are not discussed in this work.

5.2.3 Temperature Dependence of the Schottky barrier height

The temperature dependence of a Schottky Barrier is usually studied by plotting the activation energy (or Richardson) diagram. An example of such a diagram is shown in Fig. 5.3. In such a plot, a temperature independent SB height would give a straight line. Experimental curves typically exhibit a bending for low temperatures which corresponds to temperature-dependent SB heights. One of the simplest SB height temperature dependencies is the so-called T_o anomaly [161]. In this model, the ideality factor n is introduced to the SB height exponential term as:

$$J(V_a) = A^* \cdot T^2 \cdot e^{-\frac{q \cdot \phi_{Bn}}{n \cdot k \cdot T}} \cdot (e^{\frac{q \cdot V_a}{n \cdot k \cdot T}} - 1) \tag{5.12}$$

and n is assumed to have a temperature dependence described by:

$$n = 1 + \frac{T_o}{T} \tag{5.13}$$

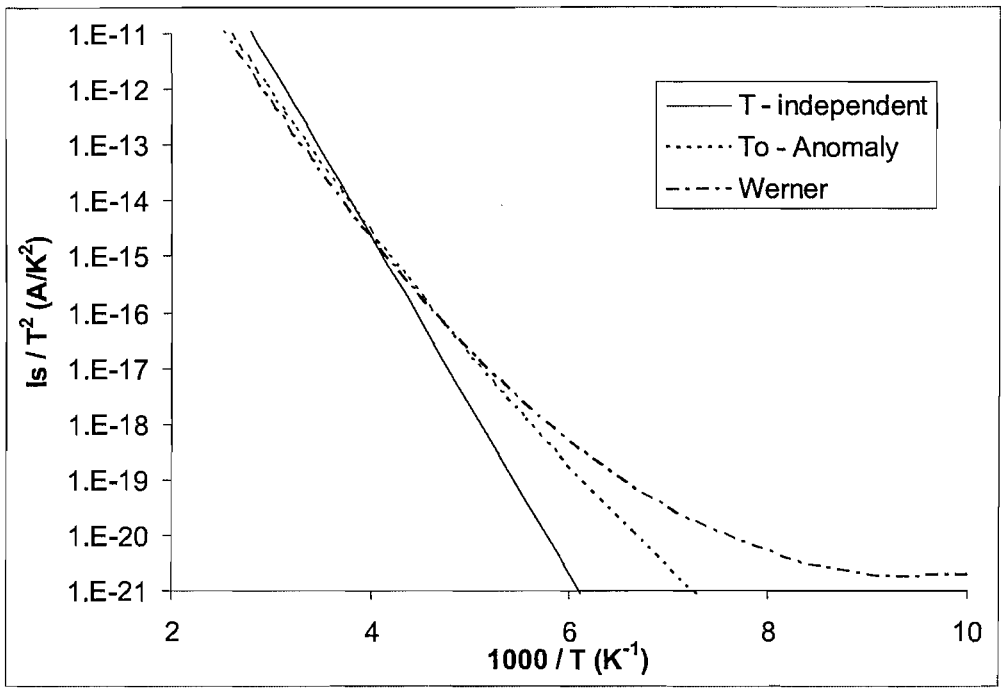

Figure 5.3: *Activation energy diagram illustrating the temperature behaviour of Schottky barriers according to different models.*

where T_o is a fitting parameter. This model can also be written such as to eliminate n and leave only T_o as a parameter in the $J-V$ expression:

$$J(V_a) = A^* \cdot T^2 \cdot e^{-\frac{q \cdot \phi_{Bn}}{k \cdot (T+T_o)}} \cdot (e^{\frac{q \cdot V_a}{k \cdot (T+T_o)}} - 1) \tag{5.14}$$

The corresponding activation energy curve is a straight line with a different gradient, as shown in Fig. 5.3. Another temperature dependent model is that suggested by Werner [160], which assumes an inhomogeneous SB. According to Werner, the current density can be written as:

$$J(V_a) = A^* \cdot T^2 \cdot e^{-\frac{q \cdot \phi_{Bn}}{k \cdot T}} \cdot (e^{\frac{q \cdot V_a}{k \cdot T}} - 1) \tag{5.15}$$

where

$$\phi_{Bn} = \overline{\phi_{Bn}} - \frac{q \cdot \sigma_s^2}{2 \cdot k \cdot T} \tag{5.16}$$

with $\overline{\phi_{Bn}}$ and σ_s being the mean value and the standard deviation of a spatial SB height distribution respectively. $\overline{\phi_{Bn}}$ and σ_s are assumed to have a linear dependence on the applied potential:

$$\overline{\phi_{Bn}} = \overline{\phi_{B_0}} + \rho_2 \cdot U_a \tag{5.17}$$

$$\sigma_s^2 = \sigma_{s_0}^2 + \rho_3 \cdot U_a \tag{5.18}$$

The activation energy diagram of this model can be obtained by calculating the saturation current from equation 5.15. The result is shown in Fig. 5.3. If the spatial distribution is on a length scale less than the space-charge width, then $\overline{\phi_{Bn}}$ should match the SB height value obtained by $C-V$ measurements. [160].

5.3 Thermionic emission analysis of electrodeposited Ni-Si Schottky barriers

5.3.1 Introduction

Here, the detailed characterisation of electrodeposited Ni-Si SBs is presented. Si substrates with epitaxial n on n+ layers are used. The n-Si layer is used to eliminate tunnelling effects and allow for a detailed characterisation of the SB using the thermionic emission theory. The n+ bulk is used to minimise the series resistance and increases the exponential region at the forward bias. Room temperature $I-V$ measurements are compared with those obtained from evaporated Ni-Si Schottky barriers and with corresponding results from the literature. $C-V$ and low temperature $I-V$ measurements are presented and interpreted according to the thermionic emission theory. The temperature dependence of the SB height is analysed using recent theoretical models. Furthermore, a possible physical explanation of the spatial Schottky barrier distribution is given using X-ray diffraction and Scanning Electron Microscopy measurements.

5.3.2 Experimental Procedure

A description of the fabrication process is illustrated in Fig. 5.4. Epitaxial n on n+ ⟨100⟩ single-side polished silicon wafers with resistivity 0.9-1 Ω cm / 0.01-0.02 Ω cm were used as substrates (Fig. 5.4a). The thickness of the n layer was 6-8 μm. A 20 nm thick layer of SiO_2 was thermally grown on the front side (Fig. 5.4b). Circular and square patterns of sizes from 0.1 mm to 1.5 mm were transferred to the SiO_2 layer by conventional lithography (Fig. 5.4c). Al ohmic back contacts were created by evaporation and annealing for 30 minutes at 450 °C in H_2/N_2 to allow for electrical measurements. (Fig. 5.4d) Subsequently, after a standard RCA cleaning step (Radio Corporation of America, H_2O_2 / NH_4OH followed by H_2O_2 / HCl) and a 20:1 buffered HF dip for 30 s , electrodeposition of Ni directly on Si was performed (Fig. 5.4e and f). The role of the HF dip is essential for the fabrication process as it removes the native oxide and prevents its reformation by leaving the Si surface H-terminated [128]. Moreover, the saturation of the dangling bonds on the Si surface by H-termination reduces the formation of interface defects during Ni deposition [162].

For electrodeposition, a Ni sulphate bath (see table 3.1) and an Autolab AUT72032 potentiostat three electrode system with a Pt counter electrode and a saturated calomel reference electrode (SCE) were used [124]. The deposition potential was -1.1 V (against the SCE). A pulse of -1.7 V was applied for 0.4 s just before the deposition stage to form a uniform Ni nucleation on Si which led to smoother deposition [149]. A metal overlap structure was formed at the edges suppressing the edge leakage currents (Fig. 5.4f). Hence, the formation of a guard ring was not required for these SBs. SBs with Ni layer thicknesses from 200 nm to 400 nm were fabricated but no variation of the SB parameters with thickness was observed.

For comparison, evaporated Ni-Si SBs were also fabricated. Al ohmic back contacts were defined and Ni-Si Schottky contacts were formed at the front by evaporation and lift-off. Again, a 20:1 buffered HF dip for 30 s was used to remove the native oxide and leave the Si surface H-terminated, just before evaporation.

$I-V$ and $C-V$ characteristics measurements were performed using a Hewlett Packard 4155A semiconductor parameter analyser and a Hewlett Packard 4280A, 1

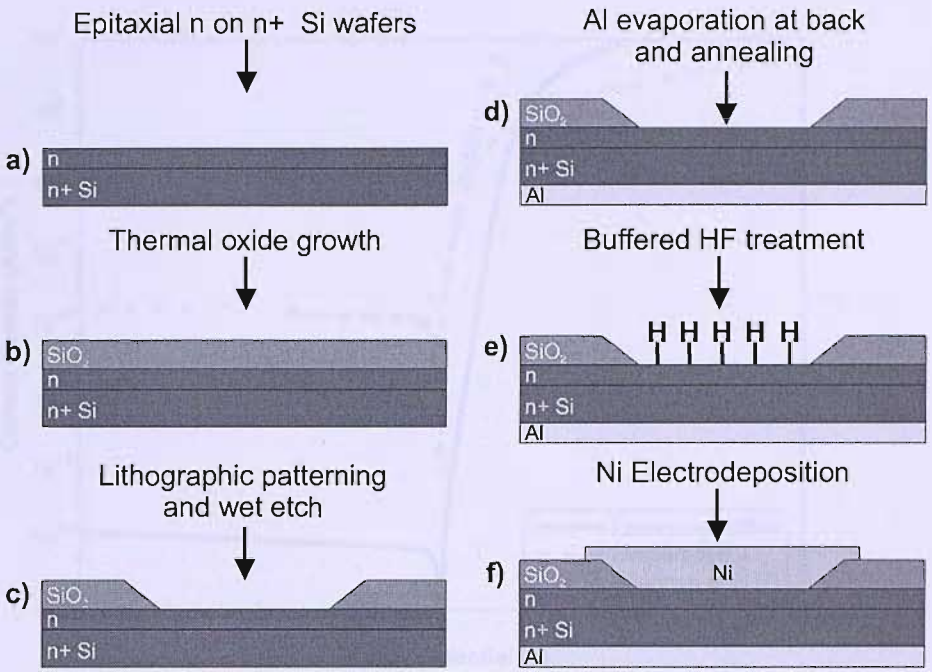

Figure 5.4: *Process flow for the fabrication of electrodeposited Ni-Si Schottky Barriers.*

MHz, C Meter/$C-V$ plotter. Low temperature $I-V$ measurements down to 86 K were performed using a Bio-Rad DL 4960 cryostat temperature controller. X-ray diffraction and Scanning Electron Microscopy (SEM) measurements where performed using a Siemens D5000 X-Ray Diffractometer and a LEO 1455VP SEM.

5.3.3 Results and Discussion

A typical current density (J) versus applied potential (V_a) characteristic of electrodeposited Ni-Si SBs for n on n+ Si is shown in Fig. 5.5. The Si resistivity of the n-layer is 0.9-1.0 Ω cm. A high quality rectifying behaviour is observed. The n+ bulk Si keeps the series resistance low increasing the exponential region at the forward bias. This allows the extrapolation of the SB parameters with increased accuracy.

For such doping concentrations tunnelling effects can be neglected and therefore thermionic emission is assumed to be the dominant transport mechanism. From the exponential part of the forward bias in Fig. 5.5, a saturation current density of J_S

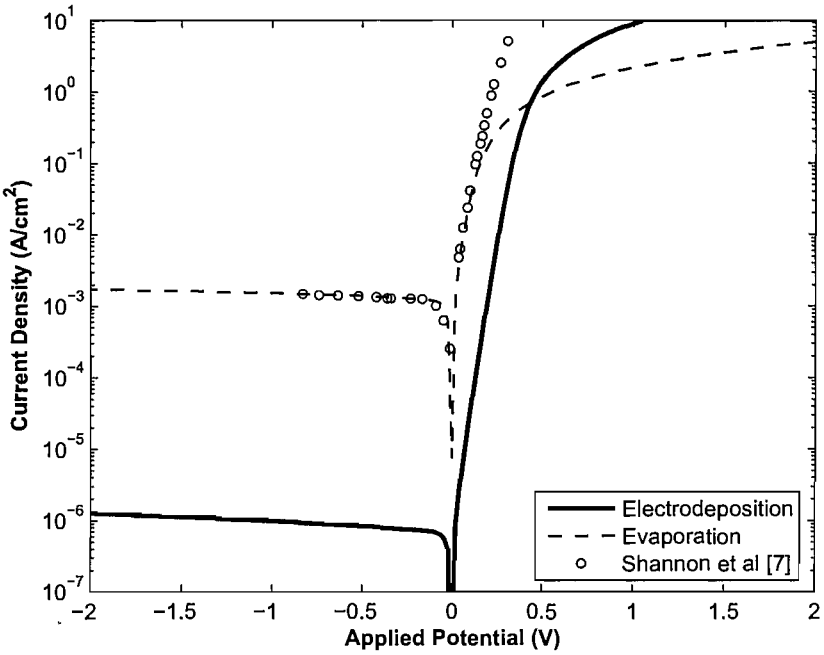

Figure 5.5: *J - V characteristics of electrodeposited and evaporated Ni-Si SBs. Epitaxial n on n+ Si with resistivity 0.9-1 Ω cm / 0.01-0.02 Ω cm was used for the electrodeposited SBs while 10-20 Ω cm Si was used for the evaporated ones. Corresponding results from the literature for evaporated Ni-Si SBs are also shown for reference. The electrodeposited contact was square with a side of 0.1 cm while the evaporated one was circular with diameter 0.04 cm.*

= 1 μA cm^{-2} is extrapolated. Using the Richardson constant value for free electrons (A^*=120 $A\ cm^{-2}\ K^{-2}$) a SB height of ϕ_B=0.78 V is obtained. The reverse leakage matches the saturation current density and has a low field dependence. No size variation of the leakage current and the SB parameters was observed indicating an effective metal overlap structure at the edges. In higher fields the junction eventually breaks down. The breakdown typically occurs for reverse biases beyond 10 V.

A typical $J-V$ characteristic of evaporated Ni-Si Schottky barriers with Si resistivity of 10-20 Ω cm is also shown in Fig. 5.5 for comparison. These measurements coincide with others reported in the literature for similar Ni-Si contacts [163]. The rectifying behaviour is much weaker compared to that of electrodeposited SBs with a considerably higher reverse bias current. The saturation current density is 1 mA

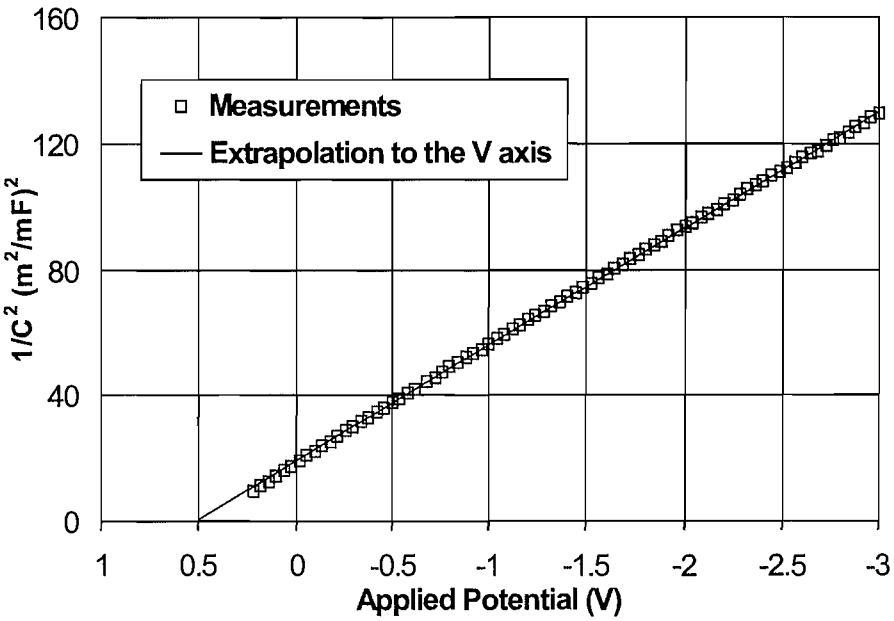

Figure 5.6: *C^{-2} - V curve of an electrodeposited Ni-Si contact. For the measurements a 1 MHz signal with 30 mV rms was used. From this curve a SB height of 0.76 V is extrapolated.*

cm^{-2} corresponding to a SB height of ϕ_B=0.60 V.

Capacitance (C) versus voltage measurements of the SBs were performed for an A^*-independent measurement of the SB height. An inverse square capacitance versus voltage characteristic is shown in Fig. 5.6. As expected, a straight line is observed and from its intercept on the voltage axis the SB height is found to be 0.76 V. Furthermore, from the slope of this characteristic the Si doping concentration can be extrapolated. A value of 2.96 10^{15} cm^{-3} is obtained, corresponding to a resistivity of 1.6 Ω cm which matches the specification of the Si substrate used (1-2 Ω cm).

In order to further investigate the quality of Ni-Si SBs obtained by electrodeposition, low temperature $J-V$ measurements were performed. The range was from 86 K to 320 K with steps of 10 K. The forward bias characteristics are shown in Fig. 5.7. For clarity, only 7 different temperatures are plotted in this diagram. As expected from the thermionic emission theory, J_S is reduced drastically with temperature. The reverse leakage current is also reduced following J_S (not shown in Fig. 5.7). Below

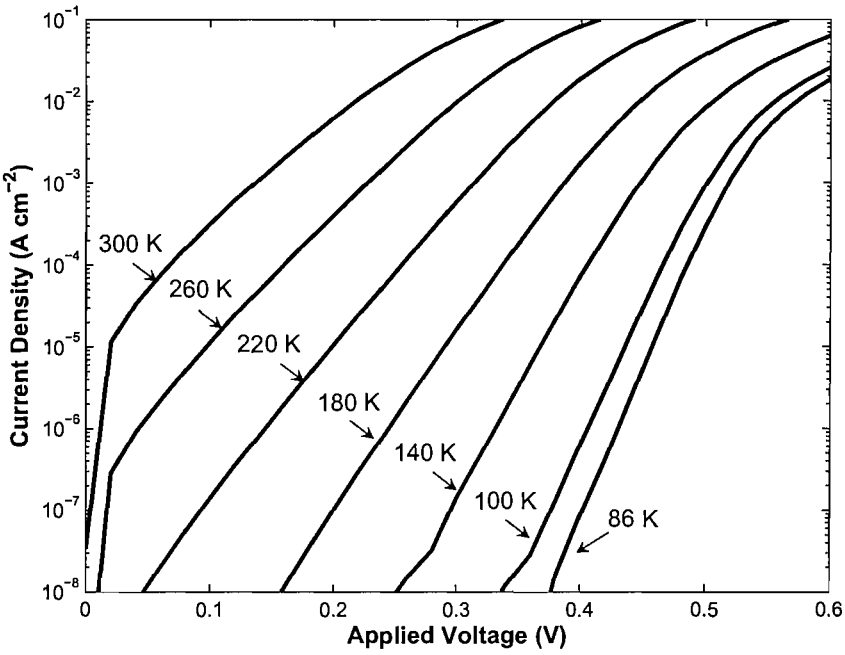

Figure 5.7: *Low temperature, forward bias J-V characteristics of a circular electrodeposited Ni-Si SB with diameter 0.15 cm.*

190 K the reverse leakage is lower than 1 pA which is the lower current limit of the measurement setup that has been used.

The saturation current density was extrapolated from the $J - V$ measurements for different temperatures and the activation energy diagram was acquired as shown in Fig. 5.8. A temperature independent SB height would result in a straight line on the activation energy diagram. A fit with $\phi_B = 0.70\ V$ is shown as a solid line in Fig. 5.8. This line fits only the high temperature experimental results. For lower temperatures a deviation from a straight line is observed, indicating a temperature dependent SB height.

Several models for the explanation of the low temperature behaviour of SBs have been proposed [159]. In order to model the temperature dependence of SB heights the T_0 effect is often used [161]. In this model, the thermionic emission equation is modified as described by equation 5.14. By using ϕ_{Bn} and T_o as free parameters, a better fit than the temperature independent SB height is achieved (dashed line in Fig. 5.8). The fitting values were 0.89 V and 70 K respectively. The square of

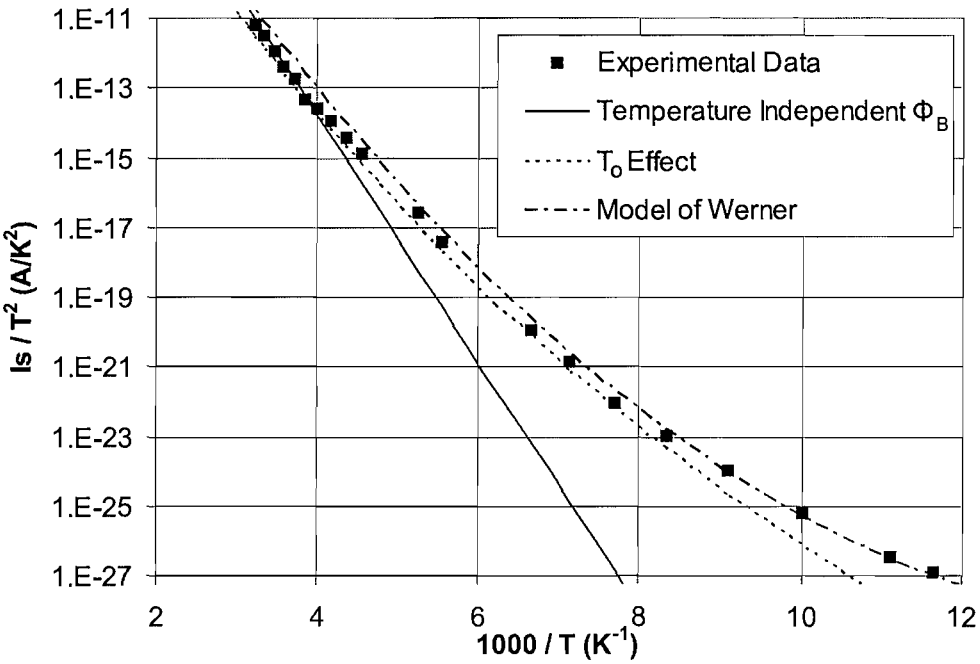

Figure 5.8: *Activation energy diagram of the same electrodeposited Ni-Si contact as in Fig. 5.7. The measurements are fitted using a temperature-independent SB height thermionic emission model, the T_0 effect model [161] and the model of Werner and Guttler [160].*

the Pearson product moment correlation coefficient for this fit is $R^2 = 0.9869$. For consistency, the same Richardson constant value as for the thermionic emission model was used (120 $A\ cm^{-2}\ K^{-2}$). However, this model fails to fit the experimental data for temperatures below 125 K.

A model that physically justifies the temperature dependence of SBs is that proposed by Werner and Guttler [160]. This model assumes a distribution of SB heights as a result of spatial inhomogeneities at the metal/semiconductor interface and is described by equations 5.15 - 5.18. If the spatial distribution is on a length scale less than the space-charge width, then $\overline{\phi_{Bn}}$ should match the SB height value obtained by $C - V$ measurements.

In order to fit our experimental results with this model we use the SB height value from $C - V$ measurements leaving the standard deviation as the only fitting parameter. Again, a value of 120 $A\ cm^{-2}\ K^{-2}$ for the Richardson constant is used.

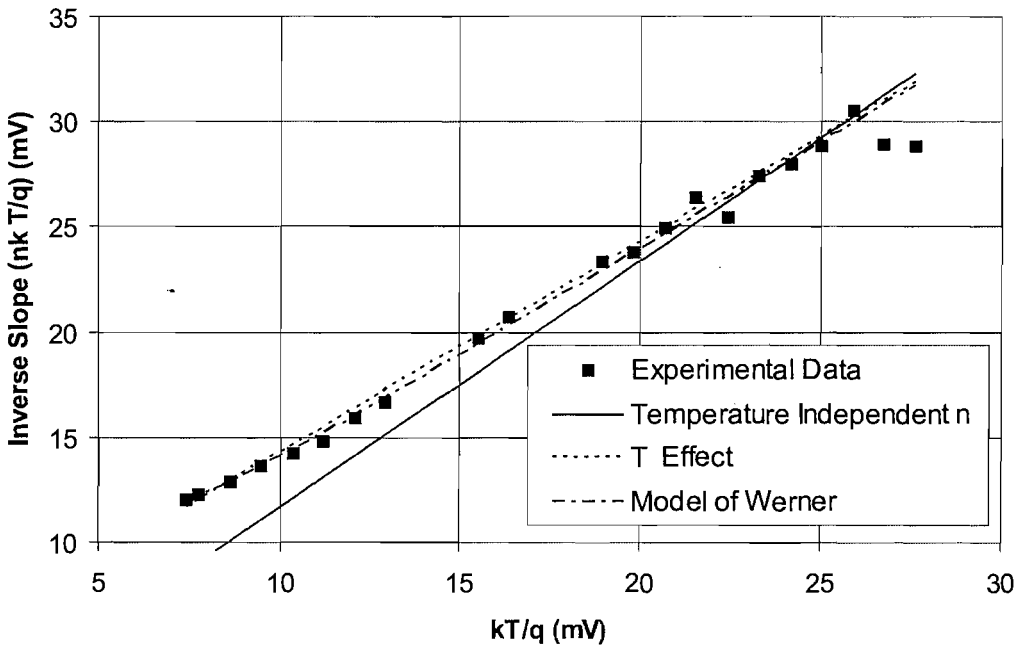

Figure 5.9: *Inverse slope of the characteristics in Fig. 5.7 versus k_BT/q. The measurements are fitted using the same models as in Fig 5.8.*

The resulting fit, using a standard deviation of 66 mV is shown as a dash-dot curve in Fig. 5.8. A good fit is obtained throughout the range of measurements ($R^2 = 0.9866$).

To investigate the slope of the $J-V$ characteristics in Fig. 5.7, the ideality factor n is introduced such that:

$$J(V_a) = A^* \cdot T^2 \cdot e^{-\frac{q \cdot \phi_B}{k \cdot T}} \cdot (e^{\frac{q \cdot V_a}{n \cdot k \cdot T}} - 1) \tag{5.19}$$

In this equation it is assumed that ϕ_B doesn't depend on V_a and therefore the slope is exclusively defined by the second exponential term.

The inverse slope of the $J-V$ characteristics in Fig. 5.7 was extrapolated and plotted versus kT/q as shown in Fig. 5.9. A temperature independent n would result in a zero-crossing straight line which cannot fit the measurements at low temperatures. A limited fit is achieved at temperatures near 300 K using an ideality factor of 1.17 (solid line in Fig. 5.9).

By comparison of equations 5.14 and 5.19, one can easily note that the T_0-effect model corresponds to an ideality factor that varies with temperature as:

$$n = 1 + \frac{T_0}{T} \tag{5.20}$$

This model results in a good fit of the measurements as shown in Fig in Fig. 5.9 (dashed line, $R^2 = 0.9867$) with $T_0 = 50$ K. However, it lacks a direct physical explanation. Moreover, as implied in equation 5.14, T_0 should have the same value for the temperature dependence of both ϕ_{Bn} and n.

The model of Werner and Guttler suggests that the deviation of the ideality factor from unity and its temperature dependence are due to the voltage dependence of the barrier distribution [160]. With the assumption that $\overline{\phi_{Bn}}$ and σ_s^2 vary linearly with bias, with gradients ρ_2 and ρ_3 respectively, as described by equations 5.17 - 5.18, n will be:

$$n = \frac{1}{1 - \rho_2 + \frac{\rho_3}{2kT/q}} \tag{5.21}$$

A good fit is obtained using $\rho_2 = 0.04$ and $\rho_3 =$ -5 mV as shown in Fig. 5.9 (dash-dot curve,$R^2 = 0.9856$). This result, along with the excellent fit of the temperature dependence of the SB height indicates that the inhomogeneous SB model of Werner and Guttler is an accurate description for electrodeposited SBs.

In order to investigate the physical origin of inhomogeneity at the electrodeposited SBs, X-ray diffraction measurements were performed and are presented in Fig. 5.10. The $\langle 400 \rangle$ Si peak at $2\theta = 69.7^o$ and a much shorter (forbidden) $\langle 200 \rangle$ Si peak at 33.3^o are observed. These peaks indicate a $\langle 100 \rangle$ crystal orientation as expected from the specifications of the Si substrate. Also, the $\langle 111 \rangle$, $\langle 200 \rangle$ and $\langle 220 \rangle$ Ni peaks are observed at 44.66^o, 51.8^o and 76.3^o respectively. The relative intensities of the Ni peaks are found to be ($\langle 111 \rangle$:$\langle 200 \rangle$:$\langle 220 \rangle$) = (100:36:16) indicating a polycrystalline Ni layer in good agreement with the relative intensities for polycrystalline Ni which are 100:42:21 (see [164] and the references therein). The Ni peaks are less intensive than those of Si because of the single crystal structure of the Si substrate.

From the width of the $\langle 111 \rangle$ Ni peak shown in the inset of Fig. 5.10 the single-

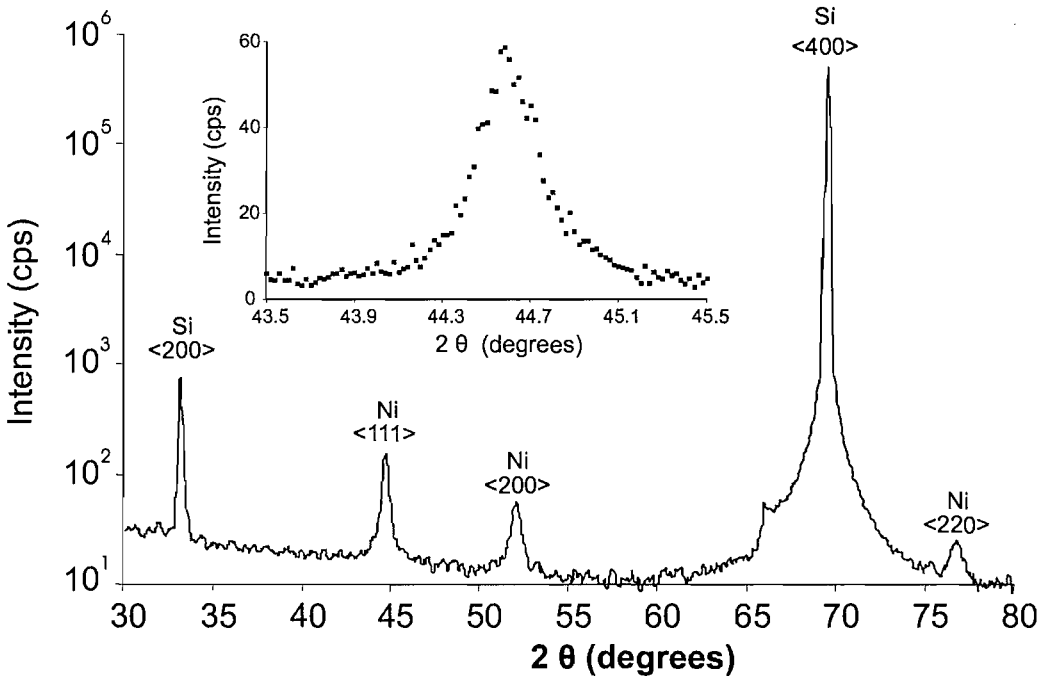

Figure 5.10: *X-ray diffraction measurements of an electrodeposited Ni-Si SB. The width of the ⟨111⟩ Ni peak (inset) reveals a vertical crystal grain size of 340 nm which is close to the total Ni layer thickness.*

crystal height is found to be 340 nm, very close to the thickness of the Ni layer which was 400 nm ±10%. This result suggests that the Ni crystal grains span from the Ni-Si interface to the top of the Ni layer.

The formation of such a structure can be explained by studying the growth process of Ni on Si. For this purpose SEM measurements were performed during the early stages of electrodeposition. A top-view SEM image of Ni on Si after an electrodeposition pulse of -1.7 V for 0.4 s is illustrated in Fig. 5.11a. The gray background is the Si substrate while the brighter dots are Ni nucleation sites. These sites may initiate crystal grains with different orientations on a length scale smaller than 200 *nm*. As these grains grow, they come to contact and, in different areas along the surface, different orientations dominate resulting ultimately in a polycrystalline film. A side-view of an electrodeposited Ni film is shown in Fig. 5.11b.

Different crystal orientations may have different work functions [165]. Therefore, the polycrystalline structure of the Ni layer may result in a spatial distribution of the

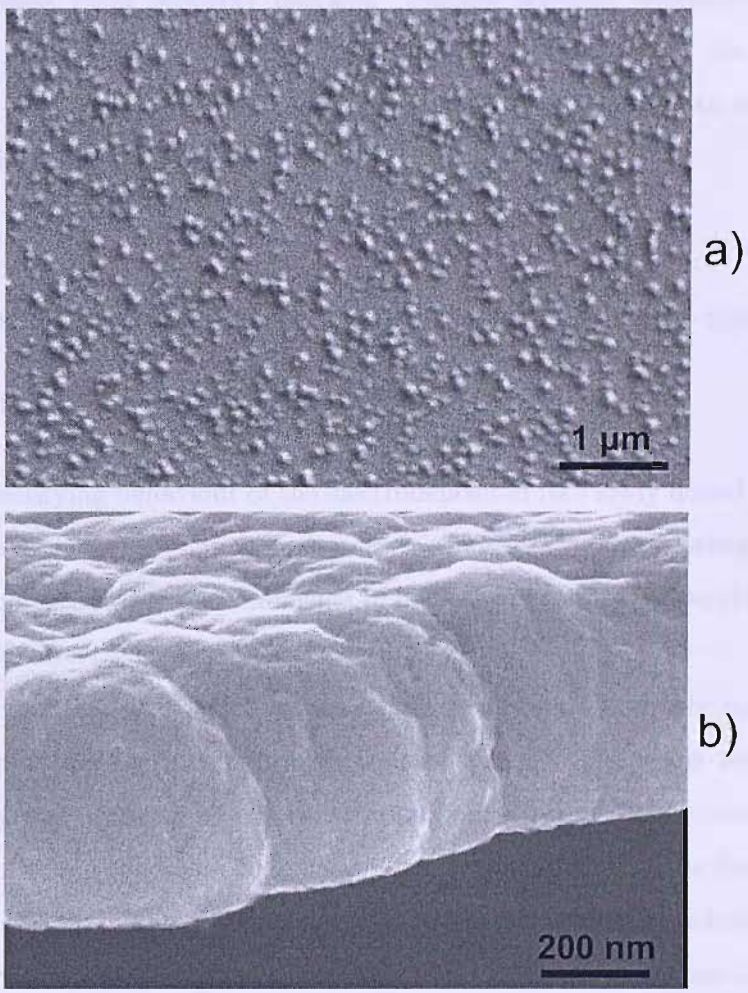

Figure 5.11: *SEM measurements showing: (a) Nucleation of Ni on Si after an electrodeposition pulse of -1.7 V for 0.4 s. The gray background is the Si substrate while the brighter dots are Ni nucleation sites. (b) Side view of an electrodeposited Ni film.*

SB height on a length scale smaller than the depletion width. This justifies the use of the SB height obtained from $C - V$ measurements as the mean SB height in the model of Werner and Gutter.

The above considerations give a possible physical explanation of inhomogeneity at electrodeposited Ni-Si Schottky barriers. Further physical characterisation by high resolution transmission electron microscopy is required to study the formation of defects and silicides at the electrodeposited Ni-Si interface and to adjudge its viability for spintronic applications.

5.4 Anisotropic magnetoresistance in self-assembled inverse sphere Ni arrays

The excellent rectifying behaviour of the electrodeposited Ni - lowly doped Si contact analysed in the previous section is now used to prevent substrate leakage currents and allow magnetoresistance measurements to be performed on self-assembled inverse sphere Ni arrays directly on Si.

These structures were prepared exploiting the guided self-assembly method presented in Chapter 4. For magnetoresistance measurements, a single layer inverse sphere Ni array was prepared as described in section 4.3. The Ni thickness was 500 nm. Dissolution of the spheres was omitted to prevent oxidation of the fine Ni structure on the inner side of the array. Due to the relatively large Ni thickness, surface oxidation was not expected to affect significantly the magnetic properties of the array.

Predetermination of the position of the array allowed Ag pads to be defined and 4-probe magnetoresistance measurements to be performed. A description of the measurement setup is shown in Fig. 5.12. Room temperature magnetoresistance measurements were performed using a square modulated current with frequency 68 Hz and a lock-in detection technique. The amplitude of the current was 1 μA for measurements with the magnetic field parallel and 10 μA for those with the magnetic field perpendicular to the current direction.

In a setup such as the one shown in Fig. 5.12, leakage currents flowing through

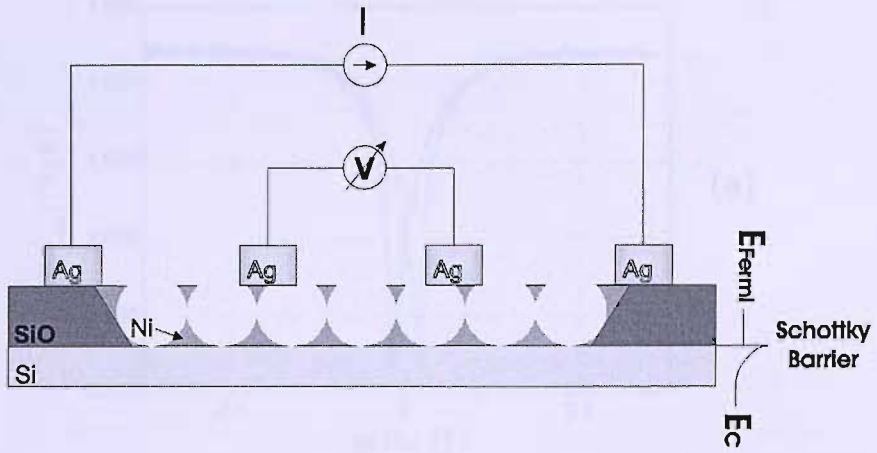

Figure 5.12: *Four-probe measurements on guided self-assembly of inverse sphere Ni arrays on Si. The size of the spherical voids is not to scale.*

the semiconducting substrate would suppress the observed magnetoresistance effects. For plain magnetic layers with very small ohmic resistances, the substrate leakage current is negligible and magnetoresistance measurements can be performed [113]. However, for patterned magnetic layers such as the inverse sphere magnetic anti-sphere arrays shown in Fig. 4.13 the resistance is substantially higher and suppression of leakages becomes paramount. This can be achieved by exploiting the excellent Schottky barrier at the electrodeposited Ni-Si interface [149].

Magnetoresistance measurements were performed at room temperature on a single layer inverse sphere rectangular Ni array with in-plane dimensions 230x10 μm and height 500 nm. The net current flow was parallel to the long dimension of the rectangle. The resistance of the array at remanence was $R(0) = 12.2\ \Omega$. In-plane measurements with the magnetic field parallel to the current are shown in Fig. 5.13a. The resistance is at a maximum when the magnetic moments in the array are parallel to the current flow. During the magnetisation reversal process, the magnetic moment turns perpendicular to the current flow resulting in lower resistance. The two distinct minima at -8 mT and +8 mT indicate some hysteresis in the array. Fig. 5.13b shows magnetoresistance measurements with the in-plane magnetic field perpendicular to the current. The resistance is at a minimum when the magnetic moments in the array

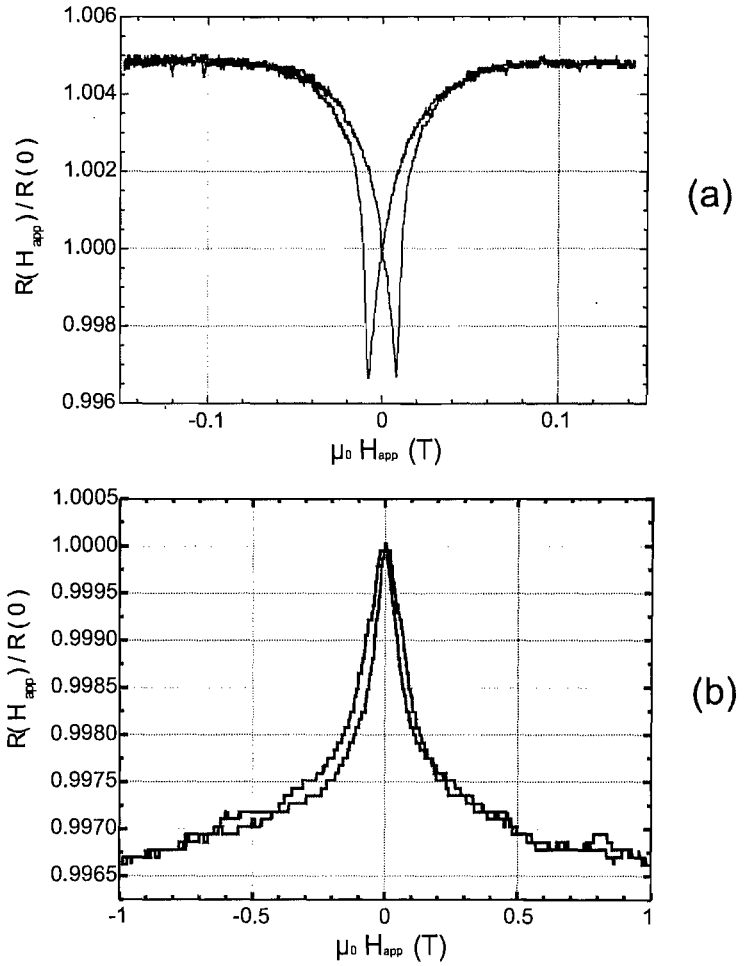

Figure 5.13: *Room temperature magnetoresistance measurements of an inverse sphere Ni array on Si for in-plane magnetic fields, (a) parallel and (b) perpendicular to the current flow.*

are aligned perpendicular to the current flow by the magnetic field. No significant hysteresis is observed indicating a reversible rotation. The maximum resistance for this case is observed when no magnetic field is applied.

From Fig. 5.13, the AMR ratio is found to be 0.85% as defined by equation 2.1. Similar results have been observed in CoFe anti-dot arrays fabricated by anodised alumina techniques but with weaker AMR effects [166]. This can be attributed to the unique geometry of the inverse sphere arrays which causes interesting magnetisation phenomena [167, 168].

It is noted that smaller resistance variation is observed for magnetisation re-

versal in the perpendicular direction. This difference could be attributed to the 3-dimensional magnetisation pattern of the zero-field state outweighing the easy axis preference. However, closer examination of the magnetisation reversal mechanisms in such structures is required for a full explanation of this effect.

5.5 Conclusions

Electrodeposited Ni-Si SBs were characterized by $J-V$, $C-V$ and low temperature $J-V$ measurements. Electrodeposition was shown to result in higher SB heights compared with evaporation. The reverse leakage current was found to be extremely low assuring a high quality rectifying behaviour. The temperature dependence of the $I-V$ characteristics can be quantitatively fitted by taking into account a model for inhomogeneous SBs as proposed by Werner and Guttler. A possible origin of the spatial variation of the SB height is the polycrystalline structure of the Ni layer. The high quality rectifying behaviour of the Ni-Si interface can be used to prevent leakage currents through the semiconducting substrate during magnetoresistance measurements on Si. The anisotropic magnetoresistance of an inverse sphere Ni array was measured to be 0.85% exceeding values obtained from similar structures. This effect is attributed to the unique 3D geometry of the arrays. More detailed studies on the magnetoresistance of these arrays should take into account that the current is not exactly parallel or perpendicular to the magnetisation as it follows the inverse spherical geometry.

Chapter 6

Thermionic field emission at Ni-Si contacts for spin injection

Current transport at Schottky barriers is of particular interest for spin injection and detection in semiconductors. Here, electrodeposited Ni-Si contacts are fabricated and the transport mechanisms through the formed Schottky barrier are studied. Highly doped Si is used to enable tunnelling currents. $I-V$, $C-V$ and low-temperature $I-V$ measurements are performed and the results are interpreted using tunnelling theory for Schottky barriers and modern models for spatially distributed barrier heights. It is shown that tunnelling is the dominant mechanism for both forward and reverse bias. An exponential reverse bias $I-V$ behaviour with negative temperature coefficient is reported. An explanation can be found in the rapid decrease of the reverse bias $I-V$ slope with temperature predicted by Padovani and Stratton for thermionic field emission in conjunction with the increase of the Schottky barrier height with temperature suggested for spatially distributed barrier heights. These results reveal the high potential of Schottky barriers for spin-injection and detection in active spintronic devices.

6.1 Introduction

Spin injection from a magnetic metal into a semiconductor requires spin conservation during the injection of the electrons. It is particularly interesting because

it allows the integration of magnetic devices with microelectronics. The conductivity mismatch problem has been shown to prevent ohmic contacts from being used for spin injection [98, 169]. Instead, Schottky barriers (SBs) and Ferromagnet (FM)/Insulator/Semiconductor contacts have been used [170]. A FM/Si/FM spintronic device has been proposed by Bratkovsky and Osipov using the SBs for injection and extraction of spin polarised electrons [171]. A detailed understanding of the transmission mechanisms in the SBs is required for the fabrication of such devices.

Thermionic Emission (TE) over a SB is believed to be unsuitable for spin injection and detection because forward bias electron transmission occurs at energies well above the Fermi level [172]. The barrier lies completely in the semiconductor due to image force lowering and hence, the spin-resolved density of states of the metal cannot provide spin dependent transmission. Furthermore, the reverse bias TE current is too small. On the other hand, it has been recognised that tunnelling currents through SBs could potentially be used for spin injection/detection [172].

In Chapter 5 it was shown that electrodeposited Ni-lowly doped Si contacts exhibit a high quality Schottky barrier [173]. TE analysis using modern models [160] revealed a large SB height and extremely low reverse leakage current. In the work presented here electrodeposited Ni-Si contacts using highly doped Si to activate tunnelling were fabricated and characterised. The results are analysed and compared with the predictions of Padovani and Stratton for tunnelling through SBs [174]. The potential of electrodeposited Schottky contacts for spin injection and detection is discussed taking into account forward and reverse bias Thermionic Field Emission (TFE).

6.2 Analytical Expressions For Thermionic Emission and Thermionic Field Emission

According to the thermionic emission theory for Schottky barriers the current density (J) versus applied potential (V) characteristic is described by the following equations:

$$J_{TE} = J_{S,TE} \cdot (e^{\frac{V}{V_t}} - 1) \tag{6.1}$$

$$J_{S,TE} = A^* \cdot T^2 \cdot e^{-\frac{\phi_{Bn}}{V_t}} \tag{6.2}$$

where $J_{S,TE}$ is the thermionic emission saturation current density, q is the elementary charge, k is the Boltzmann constant, T is the absolute temperature, $V_t = kT/q$ and A^*=120 m$^*/m$ (Acm^{-2} K^{-2}) is the effective Richardson constant with m^* and m being the effective and the free electron mass respectively. Moreover, ϕ_{Bn} is the Schottky barrier height including image force lowering:

$$\phi_{Bn} = \phi_{B,0} - \sqrt{\frac{q \cdot \mathcal{E}_{max}}{4\pi\varepsilon_s}} \tag{6.3}$$

where $\phi_{B,0}$ is the barrier height without image force lowering and ε_s is the dielectric constant of the semiconductor. In addition, $\mathcal{E}_{max}$ is the maximum electric field in the depletion region given by:

$$\mathcal{E}_{max} = \sqrt{\frac{2q \cdot N_D}{\varepsilon_s} \cdot (\phi_{B,0} - V - \xi - V_t)} \tag{6.4}$$

Here, N_D is the semiconductor doping concentration and $\xi = V_t \cdot ln(N_C/N_D)$. N_C is the effective density of states at the bottom of the conduction band.

Tunnelling at Schottky barriers can occur either at the Fermi level (field emission) or at an energy above Fermi level (thermionic field emission). For the Si doping level and the temperature range used in this work, no significant field emission is expected [157]. Therefore, only thermionic field emission is considered in the analysis. The thermionic field emission expressions are different for the forward and the reverse bias. According to Padovani and Stratton the forward bias can be described by the following equations [174]:

$$J_{TFE,f} = J_{s,TFE,f} \cdot e^{\frac{V}{E_0}} \tag{6.5}$$

$$J_{s,TFE,f} = J_m \cdot \frac{\sqrt{\pi E_{00} E_m}}{V_t} \cdot e^{-\frac{\phi_{Bn}-\xi}{E_0}} \tag{6.6}$$

where J_m is the flat-band thermionic current density and E_m is the energy at which the maximum of the energy distribution of the emitted electrons occurs:

$$J_m = A^* \cdot T^2 \cdot e^{-\frac{\xi}{V_t}} \tag{6.7}$$

$$E_m = \frac{\Phi_{Bn} - V - \xi}{cosh^2(\frac{E_{00}}{V_t})} \tag{6.8}$$

Moreover:

$$E_0 = E_{00} \cdot coth(\frac{E_{00}}{V_t}) \tag{6.9}$$

Interestingly, on account of the above, the flat-band thermionic current density can be rewritten as:

$$J_m = A^* \cdot T^2 \cdot \frac{N_D}{N_C} \tag{6.10}$$

The reverse bias thermionic field emission can be described by the following equations:

$$J_{TFE,r} = J_{s,TFE,r} \cdot e^{\frac{V}{\varepsilon'}} \tag{6.11}$$

$$J_{s,TFE,r} = \frac{A^* \cdot T^2 \cdot \sqrt{\pi E_{00}}}{V_t} \cdot \sqrt{-V + \frac{\phi_{Bn}}{cosh^2(E_{00}/V_t)}} \cdot e^{-\frac{\phi_{Bn}}{E_0}} \tag{6.12}$$

$$\varepsilon' = \frac{E_{00}}{E_{00}/V_t - tanh(E_{00}/V_t)} \tag{6.13}$$

6.3 Experimental Procedure

Ni-highly doped Si contacts were fabricated by electrodeposition on n+ -type ⟨100⟩ single-side polished silicon wafers with resistivity 0.01-0.02 Ω cm. For comparison,

Ni - moderately doped Si contacts were also fabricated using n on n+ Si The n+ resistivity was 0.01-0.02 $\Omega\ cm$ while the n resistivity was 0.9 - 1.0 $\Omega\ cm$. A 20 nm thick layer of SiO_2 was thermally grown on the front side. Circular and square patterns of sizes from 0.1 mm to 1.5 mm were transferred to the SiO_2 layer by conventional lithography. Al Ohmic back contacts were created by evaporation and annealing for 30 minutes at 450 °C in H_2/N_2 to allow for electrical measurements. Subsequently, after a standard RCA cleaning step (Radio Corporation of America, H_2O_2 / NH_4OH followed by H_2O_2 / HCl) and a 20:1 buffered HF dip for 30 s , electrodeposition of Ni directly on Si was performed. The role of the HF dip is essential as explained in section 5.3.2.

For electrodeposition, a Ni sulphate bath and an Autolab AUT72032 potentiostat three electrode system with a Pt counter electrode and a saturated calomel reference electrode (SCE) were used [124]. The deposition potential was -1.1 V (against the SCE). A pulse of -1.7 V was applied for 0.4 s just before the deposition stage to form a uniform Ni nucleation on Si which led to smoother deposition [149]. A metal overlap structure was formed at the edges suppressing the edge leakage currents. Hence, the formation of a guard ring was not required for these SBs. SBs with Ni layer thicknesses from 200 nm to 400 nm were fabricated but no variation of the SB parameters with thickness was observed.

$I-V$ and $C-V$ characteristics measurements were performed using a Hewlett Packard 4155A semiconductor parameter analyser and a Hewlett Packard 4280A, 1 MHz, C Meter/$C-V$ plotter. Low temperature $I-V$ measurements down to 86 K were performed using a Bio-Rad DL 4960 cryostat temperature controller.

6.4 Results and Discussion

Room temperature current density (J) versus voltage (V) measurements of a Ni-highly doped Si contact are shown as squares in Fig. 6.1. For comparison, $J-V$ measurements of a Ni-n on n+ Si contact are also shown (circles in Fig. 6.1). The use of n+ bulk Si for both cases assured the same series resistance as is apparent from the coincidence of the two experimental curves at forward bias higher than 0.4 V.

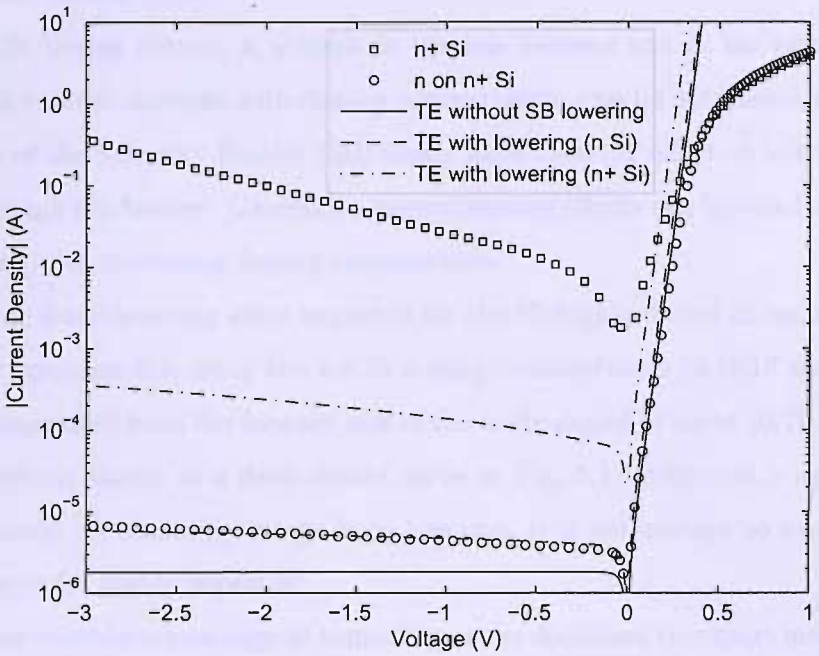

Figure 6.1: *Room temperature J - V characteristics of electrodeposited Ni-Si contacts for highly and lowly doped Si. The contacts were circular with diameter 1.5 mm. Theoretical models using the SB height extracted from the forward bias of the n on n+ characteristic are also shown.*

For n/n+ Si, a high quality rectifying behaviour is observed. TE can be assumed to be the dominant transport mechanism, since the lowly doped n layer suppresses tunnelling effects. By extrapolation from the exponential forward bias region, a Schottky barrier height value of $\Phi_{b,0}$= 0.76 V is obtained. Here, image force lowering as described by equation 6.3 has been taken into account using the N_D value that corresponds to the resistivity of the n-Si (5.3E15 cm^{-3} corresponding to the mean value of the n layer specification and confirmed by $C - V$ measurements [173]). The fitting characteristic is shown as a dashed line in Fig. 6.1. The theoretical TE characteristic for the same $\Phi_{b,0}$ without lowering is also shown as a solid line in Fig. 6.1. The difference is apparent in the reverse bias region, demonstrating the excess current that can be attributed to image force lowering for lowly doped Si. A detailed characterisation of such contacts using thermionic emission has been presented in the previous chapter and the results have been explained using the model

of Werner and Gutter [173].

For n+ Si, excess current is evident in the low forward and in the reverse bias region. This current increase with doping concentration can be attributed either to the increase of the Schottky Barrier (SB) image force lowering effect or to tunnelling currents through the barrier. Generation-recombination effects can be ruled out since they decrease with increasing doping concentration.

The image force lowering effect expected for the Ni-highly doped Si contacts will be given by equation 6.3, using the n+ Si doping concentration (2.1E18 cm^{-3}) and the $\Phi_{b,0}$ extrapolated from the forward bias of the lowly doped Si curve (0.76 V). The resulting curve is shown as a dash-dotted curve in Fig. 6.1. Although a significant J increase could be caused by image force lowering, it is not enough to explain the excess currents for highly doped Si.

The above considerations suggest tunnelling as the dominant transport mechanism at electrodeposited Ni- highly doped Si contacts. To further support this suggestion, low temperature measurements were performed as shown in Fig. 6.2. These measurements were taken with a temperature step of 10 K. For clarity, only five curves are plotted in Fig. 6.2. In the forward bias, a minor increase of J with T is observed. In the low reverse bias, J increases with T as well. However, for temperatures below 250 K, at around -1 V to -1.5 V a sudden slope increase is observed indicating a switch of the dominant transport mechanism. For reverse bias larger than -1.5 V, the temperature coefficient becomes negative. While Schottky barrier models predict the decrease of the barrier height with decreasing temperature [160], and the thermionic field emission theory can, under certain circumstances predict higher currents for lower temperatures [174], this is the first experimental observation of negative current-temperature coefficient at Schottky barriers to my knowledge.

6.4.1 Forward bias

By extension of the linear forward bias part of Fig. 6.2 from 0.1 V to 0.4 V, to the J axis, the saturation current density is obtained for different temperatures. These measurements are plotted as filled circles in Fig. 6.3. For comparison, corresponding

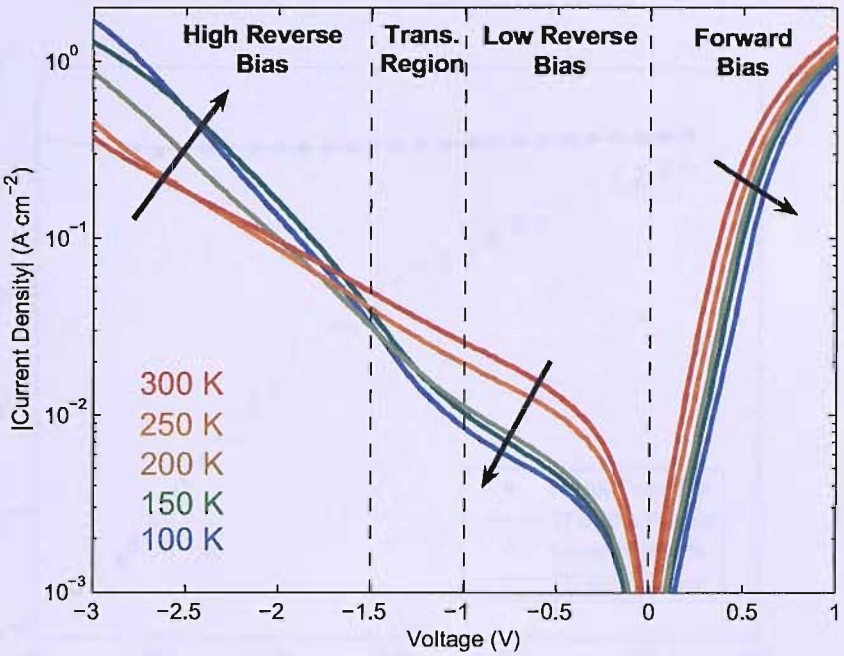

Figure 6.2: *Low temperature J - V characteristics of an electrodeposited Ni-Si contact for highly doped Si. The contact was circular with diameter 1.5 mm.*

data for n/n+ Si from [173] are also shown as open circles.

The decrease of J_s with decreasing temperature for highly doped Si is much smaller than that observed for the lowly doped Si. This can be explained by comparing the theoretical temperature dependence of J_s for thermionic and thermionic field emission as given by equations 6.2 and 6.6. While thermionic emission always gives a strong temperature dependence, thermionic field emission can be much less temperature dependent.

The experimental results for lowly doped Si suggest a spatial distribution of the SB height [173]. A good fit is obtained by using the model of Werner and Guttler [160]. This fit is shown as a dashed line in Fig. 6.3. In analogy, a spatial SB height distribution can be assumed for the highly doped Si contact and used in equation 6.6 for the TFE model. However, the resulting large number of parameters (m^*, N_D, mean SB height value $\overline{\phi_{Bn}}$ and standard deviation σ_s) requires the independent determination of some of them.

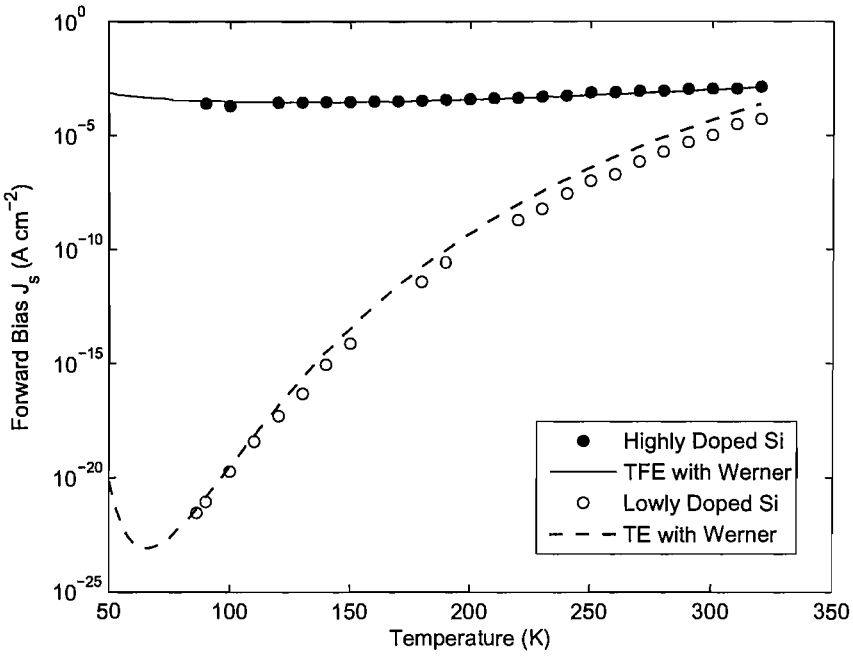

Figure 6.3: *Saturation current density versus temperature as extrapolated from Fig 6.2, from 0.1 V to 0.4 V. Results from lowly doped Si Ni-Si Schottky barriers [173] are also shown for comparison.*

For this reason, room temperature $C-V$ measurement were performed to determine N_D and $\overline{\phi_{Bn}}$. An inverse square capacitance versus voltage characteristic is shown in Fig. 6.4. For low reverse bias a straight line is observed. From the intercept of this line on the voltage axis, as extrapolated from the bias interval [-1,0] the SB height is calculated to be 1.19 V [156]. This value should match the mean SB height $\overline{\phi_{Bn}}$ of Werner and Guttler's model [160]. Furthermore, from the slope of this characteristic the Si doping concentration can be extrapolated. A value of 1.32 10^{18} cm^{-3} is obtained, corresponding to a resistivity of 0.019 Ω cm which matches the specification of the Si substrate used (0.01-0.02 Ω cm).

Using the $C-V$ measured values for N_D and $\overline{\phi_{Bn}}$ the highly doped Si experimental data of Fig. 6.3 are fit, using m* and σ_s as fitting parameters. A good fit shown as a dash-dotted black line is obtained with m*=0.013 and σ_s= 90 mV.

The above results indicate that thermionic field emission is the dominating transmission mechanism in the low forward bias region. This is illustrated in Fig. 6.5.

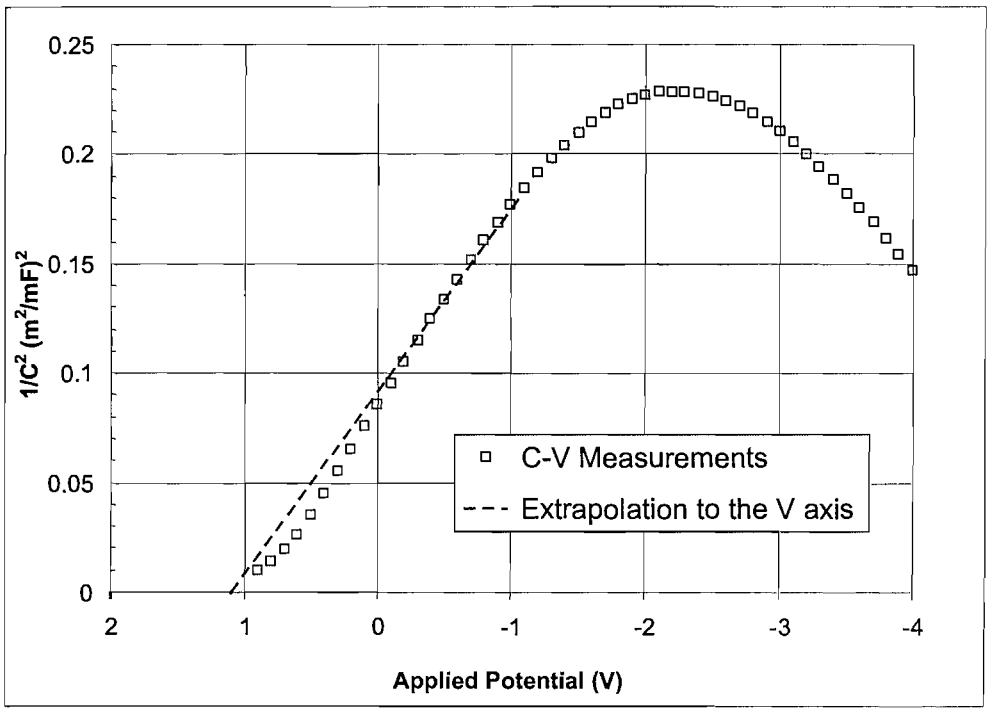

Figure 6.4: *C−V measurements of electrodeposited Ni-Si contacts for highly doped Si. From the linear reverse bias region [-1, 0] (Volts) the mean SB height and the Si doping concentration can be extrapolated.*

The excess forward bias current observed for highly doped Si compared with that for lowly doped Si is attributed to tunnelling. This excess current is large (around 10^{-3} $A\ cm^{-2}$, corresponding to tunnelling current 2 orders of magnitude larger than thermionic emission) between 0 and 0.1 V forward bias and decreases with increasing bias. This result provides an excellent explanation of recent observation of spin-detection through Fe/GaAs and NiFe/GaAs SBs [175]. According to this study, the spin dependent current across the metal-semiconductor interface varies with forward bias as shown in the inset of Fig. 6.5. Maximum spin dependent current observation is obtained within the thermionic field emission bias region revealed by this Ph.D. work. For larger biases, thermionic emission kicks in and spin effects are decreased, reaching zero for sufficiently high forward bias.

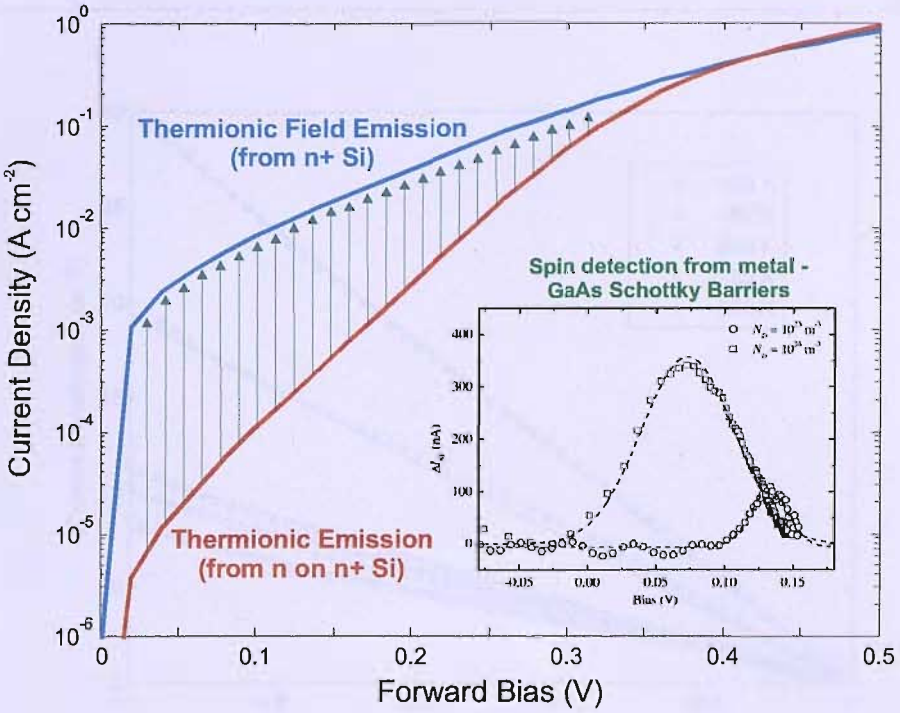

Figure 6.5: *J-V characteristics of Ni-Si contacts for lowly and highly doped Si re-plotted from Fig. 6.1, for the low forward bias. The excess current for highly doped Si is attributed to thermionic field emission. This result explains the observation of spin-detection through metal-GaAs SBs in the same bias region and for similar doping concentration shown in the inset (after Steinmuller et. al. [175])*

6.4.2 Low reverse bias

For low reverse bias, the current density appears to increase linearly with bias. Using a linear model, a good fit is obtained as illustrated in Fig. 6.6. The intersection of the fitting curves with the J axis was set to zero. For low temperatures, the experimental results indicate a transport mechanism with small temperature dependence. For temperatures greater than 240 K a sharp increase is observed. This increase could be attributed to the interpolation of the high reverse bias mechanism in this region for high temperatures. A physical explanation of this linear mechanism could involve tunnelling effects through the oxide at the edges or other defective sites of the contact.

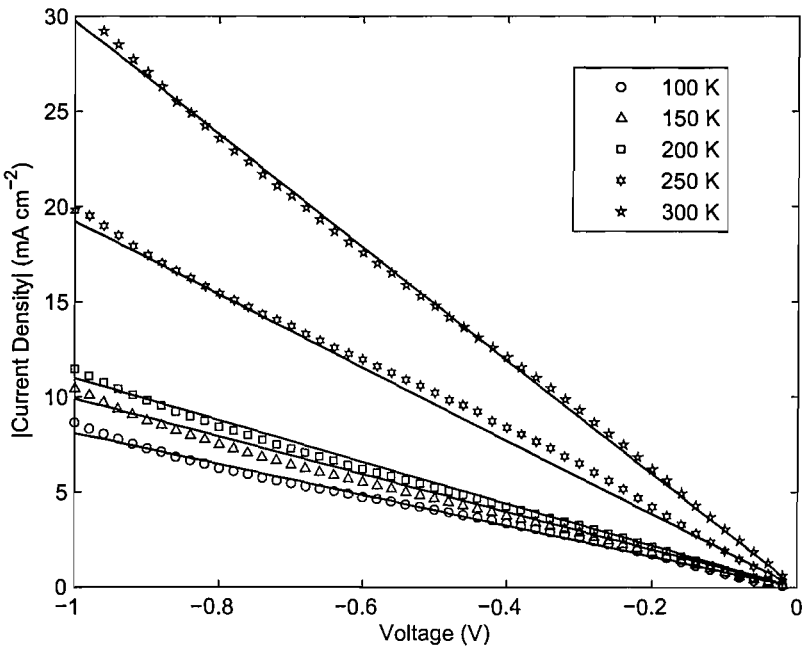

Figure 6.6: *Low reverse bias $J-V$ characteristics for different temperatures. A linear model of the form y=a·x fits the experimental results.*

6.4.3 High reverse bias

The response for reverse biases higher than -1.5 V is studied by extrapolation of its saturation current density $J_{S,r}$ from the interval between -1.5 V and -2.5 V as shown in Fig. 6.7. The excellent fit indicates that the high reverse bias current density increases exponentially with reverse voltage, in agreement with the predictions of thermionic field emission theory (equation 6.11). The reverse bias gradient $\mathrm{d}(\ln J)/\mathrm{d}V$ and saturation current density can be extrapolated from this fit. The gradient increases with decreasing temperature as expected from thermionic field emission theory (equation 6.13). The extrapolated saturation current density, $J_{s,r}$ for different temperatures is plotted as filled squares in Fig. 6.8.

For consistency, these results should be discussed in combination with the forward bias analysis. Therefore, the forward bias extrapolated $J_{S,f}$ data from Fig. 6.3 are re-plotted here for comparison (shown as filled circles in Fig. 6.8). It can be observed that the forward and reverse bias J_s follow very similar trends.

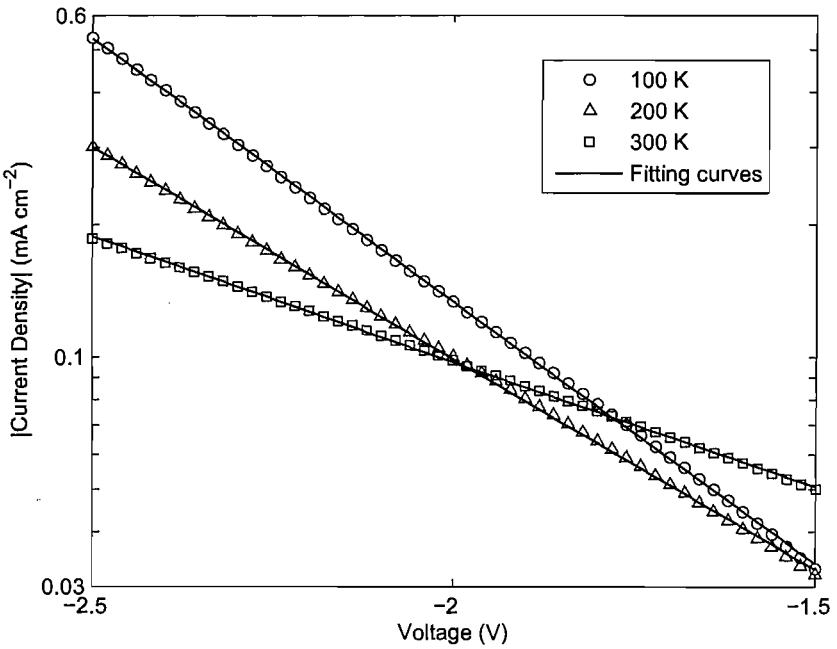

Figure 6.7: *Exponential fit of the high reverse bias $J-V$ characteristics for different temperatures. For clarity, only the 100 K, 200 K and 300 K characteristics are shown. The lines are linear extrapolations of the experimental data in the logarithmic scale.*

The forward bias thermionic field emission fit as described in the analysis of the forward bias is shown as a solid line in Fig. 6.8. Using the parameter values obtained from this fit, the reverse bias thermionic field emission saturation current density is calculated from equation 6.12. The result is shown as a dashed line in Fig. 6.8.

The pair of theoretical curves in Fig. 6.8 predict that the forward and reverse bias saturation current densities follow the same temperature-dependence trend with $J_{s,r} \sim 10 \cdot J_{s,f}$. This is consistent with the experimental results which indeed exhibit such a ratio. The relatively poor quantitative fit of the reverse bias data can be attributed to the inevitable complications involved in the consistent, simultaneous fitting of forward and reverse bias for thermionic field emission.

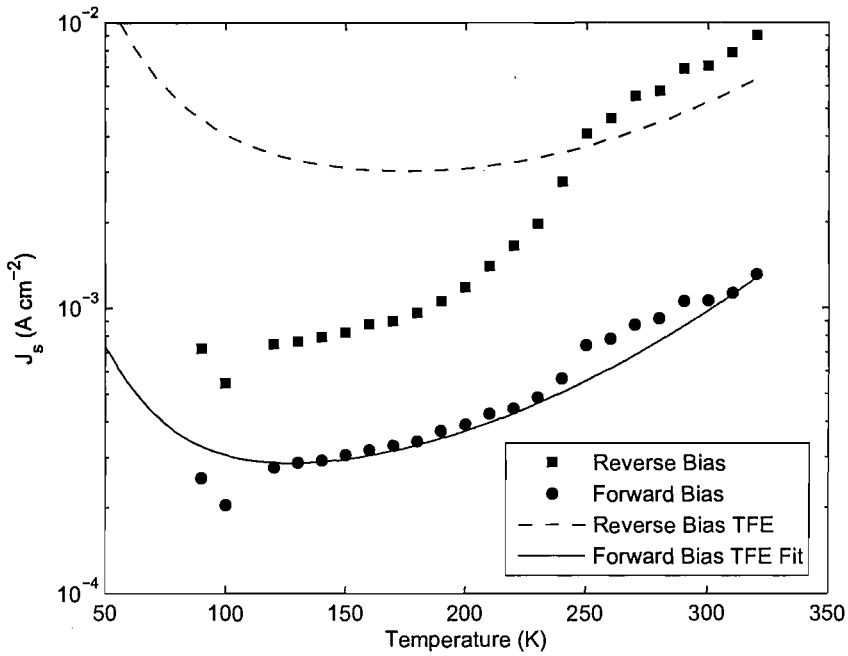

Figure 6.8: *Temperature dependence of the original and modified, high reverse bias J_s extrapolated as show in Fig 6.7. The forward bias J_s and its TFE fit from Fig. 6.3 is also plotted for comparison.*

6.5 Conclusions

In this work, thermionic field emission at electrodeposited Ni - highly doped Si contacts was studied. It is concluded that the excess forward and reverse bias current for n+ Si at electrodeposited Ni-Si contacts may be attributed to thermionic field emission over the Schottky barrier.

Current increase with decreasing temperature at reverse biased, electrodeposited Ni-highly doped Si Schottky barriers is reported. This effect takes place in the exponential reverse bias region and can be explained by the decrease of the Schottky barrier height with decreasing temperature as suggested by Werner and Gutter's model in conjunction with the rapid increase of the $\ln(J)$ - V slope predicted by Padovani and Stratton for thermionic field emission. This is the first experimental demonstration of this effect to my knowledge.

While the domination of tunnelling in reverse biased Schottky barriers has been widely acknowledged, the identification of the forward bias Schottky barrier current as

a tunnelling current for certain bias voltages is of particular importance. Assuming domination of thermionic emission at forward bias, it has been pointed out that SBs need to be reverse biased for spin injection and detection [172]. Under this assumption a spin injection and detection device with two SBs in series and a single type semiconductor would not be possible. The evidence presented in this chapter showing tunnelling dominating at forward and reverse bias even at room temperature reveals that SBs have the potential of being used in series for all electrical spin injection and detection devices. It also provides an excellent explanation of recent spin-injection optical studies in GaAs showing SB spin detection evidence at low forward biases [175].

Chapter 7

Conclusion

Practical application of spin-electronics and nanotechnology depends largely on their compatibility with conventional microelectronics technology and hence on their integration with semiconductors. The work of this Ph.D. thesis is on the integration of spintronic devices and nano-fabrication techniques with silicon. In the first two chapters a review of spintronics was presented. The need of semiconductors for active spin devices was highlighted.

A metallisation technique was developed for Si using Ni electrodeposition. An electrodeposition setup was manually built. The effect of Si resistivity to the electrodeposition process was studied and it was shown that electrodeposition on n-type Si with resistivities ranging from 0.01 Ω cm to 10 Ω cm is possible without the need of back contacts. Using patterned Si/SiO_2 substrates, selective electrodeposition on the semiconducting Si and not on the insulating SiO_2 was demonstrated. This allowed the use of conventional lithography for electrodeposition patterning. The electrodeposition growth modes were studied and improvement of the film roughness by adjustment of the electrodeposition parameters was achieved. The magnetic properties of electrodeposited films were studied and a correlation between the film roughness and coercivity was revealed.

A latex spheres self-assembly technique was successfully applied to Si substrates. This allowed the combination of this technique with conventional lithography for guided self assembly. Self-assembly selective localisation and orientation control were

achieved by using Si/SiO_2 geometrical structures on Si wafers. Guiding effects were studied using a specially prepared lithography mask. Commensurability between the guiding patterns and the spheres was shown to control the quality and the symmetry of the self-assembly. Reproducible fracturing by using accurately sized guiding stripes was demonstrated. The alignment of self-assembly arrays using guiding stripes was achieved, improving the long-range self-assembly quality. This technique was combined with electrodeposition to transfer the structures to magnetic materials. An almost defect-free pattern transfer was achieved allowing the fabrication of inverse sphere Ni nano arrays on Si by guided self-assembly. This work is promising for Si integrated magnetic random access memory and patterned recording media applications.

The Schottky barrier at electrodeposited Ni-Si contacts was studied. Lowly doped Si was used to suppress tunnelling currents and allow for a thermionic emission analysis. A high-quality Schottky barrier was observed with extremely low reverse leakage current. The experimental results were analysed using modern models for Schottky barriers assuming a spatial distribution for the barrier height. Physical characterisation of the Ni layer by Scanning Electron Microscopy and X-Ray Diffraction measurements were performed revealing that the polycrystalline structure of electrodeposited Ni may be the origin of this spatial distribution. The strong rectifying behaviour obtained for lowly doped Si was used to suppress substrate leakage currents during magnetoresistance measurements on inverse sphere Ni nanoarrays prepared as described above. The demonstration of magnetoresistance effects directly on Si show that active integration of spintronic devices with semiconductor microchips may be viable.

Ni-Si Schottky barriers using highly doped Si to enable and characterise tunnelling effects for spin injection and detection applications were fabricated. Large excess currents both at the forward and the reverse bias were observed which could not be explained by thermionic emission even by taking image force lowering into account. The high quality of electrodeposited Ni-Si Schottky barriers allowed the observation and study of a leakage-free reverse bias thermionic field emission current. A negative temperature coefficient is revealed which can be explained by the radical decrease of

the thermionic field emission ln$J$-V slope with temperature as predicted by Padovani and Stratton [174] along with the barrier height increase with temperature predicted by modern Schottky barrier models [160]. Furthermore thermionic field emission was identified as the dominant transmission mechanism for low forward bias as well. This result reveals that Schottky barriers can be used in both biases for spin dependent transmission and therefore they are very promising as spin injectors and detectors for active spin devices.

The outcome of this work is significant because it provides an understanding of the physical and electrical properties of electrodeposited metal-Si interfaces and because of the potential applications to current and future microelectronics. For example, a Si spin-valve can be fabricated using back-to-back electrodeposited Schottky barriers for the demonstration of all electrical spin-injection and detection. A simple device design is shown in Fig. 7.1. The demonstration of all electrical spin-injection and detection would be an international breakthrough in the field of electronics with major physical and engineering implications. It would open up the way for the observation of predicted physical effects that have not been experimentally confirmed. Another potential application of this Ph.D. work could be to self-assembled magnetic tunnel junctions (MTJs) on Si for magnetic random access memory (MRAM). This will combine the long-range and positioning of sphere self-assembly on Si with the controllable Schottky barrier at the metal-Si interface to fabricate highly ordered MTJ arrays with integrated diodes for sneak current suppression.

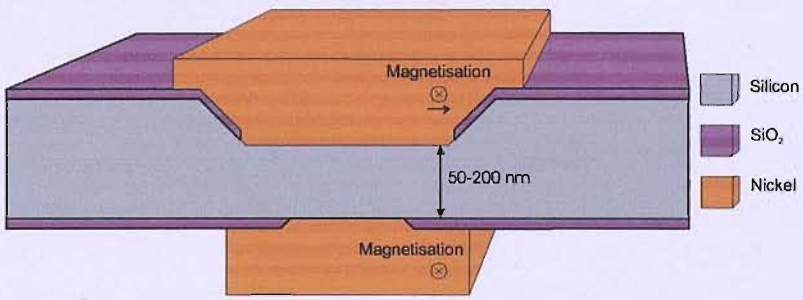

Figure 7.1: *Si spin injection and extraction device utilising tunnelling through electrodeposited Ni-Si contacts. The two ferromagnetic layers are asymmetrically designed to switch under different external magnetic fields.*

References

[1] S. A. Wolf, D. D. Awchalom, R. A. Buhrman, J. M. Daughton, S. von Molnar, M. L. Roukes, A. Y. Chtchelkanova, and D. M. Treger. Spintronics: A spin-based electronics vision for the future. *Science*, 294:1488–1495, 2001.

[2] D. D. Awschalom, R. A. Buhrman, J. M. Daughton, M. L. Roukes, and S. von Molnar. Wtec panel on spin electronics, final report, 2003. (url = http://www.wtec.org/spin).

[3] I. Zutic, J. Fabian, and S. Das Sarma. Spintronics: Fundamentals and applications. *Rev. Mod. Phys.*, 76:323–410, 2004.

[4] H. Ohno, F. Matsukura, and Y. Ohno. Semiconductor spin electronics. *J. Soc. App. Phys. Int.*, (5):4–13, 2002.

[5] J. F. Gregg, I. Petej, E. Jouguelet, and C. Dennis. Spin electronics a review. *J. Phys. D: Appl. Phys.*, 35:R121–R155, 2002.

[6] J. F. Bobo, L. Gabillet, and M. Bibes. Recent advances in nanomagnetism and spin electronics. *J. Phys.: Condens. Matter*, 16:S471–S496, 2004.

[7] T. McGuire and R. Potter. Anisotropic magnetoresistance in ferromagnetic 3D alloys. *IEEE Trans. Magn.*, 11:1018–1038, 1975.

[8] S. Parkin, X. Jiang, C. Kaiser, A. Panchulaand K. Roche, and M. Samant. Magnetically engineered spintronic sensors and memory. *Proceedings of the IEEE*, 91:661–680, 2003.

[9] I. E. T. Iben. Head reliability of amr sensors based on thermal stress tests. *IBM J. of Res. and Dev.*, 47:415–428, 2003.

[10] E. Favre-Nicolin and L. Ranno. Anisotropic magnetoresistance in manganite films. *J. Magn. Magn. Mater.*, 272-276:1814–1815, 2004.

[11] H. Nagura, K. Saito, K. Takanashi, and H. Fujimori. Influence of third elements on the anisotropic magnetoresistance in permalloy films. *J. Magn. Magn. Mater.*, 212:53–58, 2000.

[12] M. Gruyters. Anisotropic magnetoresistance in CoO/Co and CoO/Fe bilayers in the biased and unbiased state. *J. Appl. Phys.*, 95:2587–2592, 2004.

[13] P. Ripka, M. Vopalensky, A. Platil, M. Doscher, K. M. H. Lenssen, and H. Hauser. Amr magnetometer. *J. Magn. Magn. Mater.*, 254-255:639–641, 2003.

[14] H. Hauser, J. Hochreiter, G. Stangl, R. Chabicovsky, M. Janiba, and K. Riedling. Anisotropic magnetoresistance effect field sensors. *J. Magn. Magn. Mater.*, 215-216:788–791, 2000.

[15] A. Platif, J. Kubik, M. Vopalensky, and P. Ripka. Precise amr magnetometer for compass. *Proc. of IEEE Sensors.*, 1:472–476, 2003.

[16] B. Dieny, M. Li, S. H. Liao, C. Horng, and K. Ju. Effect of interfacial specular electron reflection on the anisotropic magnetoresistance of magnetic thin films. *J. Appl. Phys.*, 88:4140–4145, 2000.

[17] M. N. Baibich, J. M. Broto, A. Fert, F. Nguyen Van Dau, F. Petroff, P. Eitenne, G. Creuzet, A. Friederich, and J. Chazelas. Giant magnetoresistance of (001) Fe/(001)Cr magnetic superlattices. *Phys. Rev. Lett.*, 61:2472–2475, 1988.

[18] G. Binasch, P. Grunberg, F. Saurenbach, and W. Zinn. Enhanced magnetoresistance in layered magnetic structures with antiferromagnetic interlayer exchange. *Phys. Rev. B*, 39:4828–4830, 1989.

[19] G. A. Prinz. Magnetoelectronics. *Science*, 282:1660–1663, 1998.

[20] L. Wang, W. J. McMahon, B. Liu, Y. H. Wu, and C. T. Chong. Interface or bulk scattering in the semiclassical theory for spin valves. *Phys. Rev. B*, 69(214403), 2004.

[21] J. Barnas, A. Fuss, R. E. Camley, P. Grnberg, and W. Zinn. Novel magnetoresistance effect in layered magnetic structures: Theory and experiment. *Phys. Rev. B*, 42:8110–8120, 1990.

[22] T. Valet and A. Fert. Theory of the perpendicular magnetoresistance in magnetic multilayers. *Phys. Rev. B*, 48:7099–7113, 1993.

[23] Q. Huang, D. P. Young, and E. J. Podlaha. Magnetoresistance of electrodeposited ironcobaltnickelcopper multilayers. *J. Appl. Phys.*, 94:1864–1867, 2003.

[24] S. S. P. Parkin, Z. G. Li, and David J. Smith. Giant magnetoresistance in antiferromagnetic Co/Cu multilayers. *Appl. Phys. Lett.*, 58:2710–2712, 1991.

[25] B. Dieny, V. S. Speriosu, S. Metin, S. S. P. Parkin, B. A. Gurney, P. Baumgart, and D. R. Wilhoit. Magnetotransport properties of magnetically soft spin-valve structures (invited). *J. Appl. Phys.*, 69:4774–4779, 1991.

[26] S. S. P. Parkin and D. Mauri. Spin engineering: Direct determination of the Ruderman-Kittel-Kasuya-Yosida far-field range function in ruthenium. *Phys. Rev. B*, 44:7131–7134, 1991.

[27] H. Fukuzawa, K. Koi, H. Tomita, H. N. Fuke, Y. Kamiguchi, H. Iwasaki, and M. Sahashi. NOL specular spin-valve heads using an ultrathin CoFe free layer. *J. Magn. Magn. Mater.*, 235:208–212, 2001.

[28] W. F. Egelhoff, P. J. Chen, C. J. Powell, M. D. Stiles, R. D. McMichael, J. H. Judy, K. Takano, A. E. Berkowitz, and J. M. Daughton. Specular electron scattering in giant magnetoresistance spin valves. *IEEE Trans. Magn.*, 33(5):3580–3582, 1997.

[29] M. A. M. Gijs, S. K. J. Lenczowski, and J. B. Giesbers. Perpendicular giant

magnetoresistance of microstructured Fe/Cr magnetic multilayers from 4.2 to 300 K. *Phys. Rev. Lett.*, 70:3343–3346, 1993.

[30] Y. Seyama, A. Tanaka, and M. Oshiki. Giant magnetoresistance properties of CoFe/Cu multilayer in the CPP (Current Perpendicular to the Plane) geometry. *IEEE Trans. Magn.*, 35:2838–2840, 1999.

[31] M. A. M. Gijs and G. E. W. Bauer. Perpendicular giant magnetoresistance of magnetic multilayers. *Adv. Phys.*, 46:285–445, 1997.

[32] H. Yuasa, M. Yoshikawa, Y. Kamiguchi, K. Koi, H. Iwasaki, M. Takagishi, and M. Sahashi. Output enhancement of spin-valve giant magnetoresistance in current-perpendicular-to-plane geometry. *J. Appl. Phys.*, 92:2646–2650, 2002.

[33] H. Hoshiyaa and K. Hoshino. Current-perpendicular-to-the-plane giant magnetoresistance in structures with half-metal materials laminated between CoFe layers. *J. Appl. Phys.*, 95:6774–6776, 2004.

[34] W. F. Egelhoff, J. P. J. Chen, C. J. Powell, D. Parks, R. D. McMichael, J. H. Judy, D. Martien, A.E. Berkowitz, and J. M. Daughton. Optimizing gmr spin valves: the outlook for improved properties. *IEEE Int. Nonvol. Mem. Techn. Conf.*, pages 34–37, 1998.

[35] S. S. P. Parkin. Tne magic of magnetic multilayers. *IBM J. of Res. and Dev.*, 1:3–6, 1998.

[36] J. Daughton, J. Brown, E. Chen, R. Beech, A. Pohm, and W. Kude. Magnetic field sensors using GMR multilayer. *IEEE Trans. Magn.*, 30:4608–4610, 1994.

[37] C. Tsang, R. E. Fontana, T. Lin, D. E. Heim, V. S. Speriosu, B. A. Gurney, and M. L. Williams. Design, fabrication and testing of spin-valve read heads for high density recording. *IEEE Trans. Magn.*, 30:3801–3806, 1994.

[38] R. R. Katti. Current-in-plane pseudo-spin-valve device performance for giant magnetoresistive random access memory applications (invited). *J. Appl. Phys.*, 91:7245–7250, 2002.

[39] R. R. Katti. Giant magnetoresistive random-access memories based on current-in-plane devices. *Proceedings of the IEEE*, 91:687–702, 2003.

[40] J. G. Zhu and Y. Zheng. Ultrahigh density vertical magnetoresistive random access. *J. Appl. Phys.*, 87:6668–6673, 2000.

[41] X. Zhu and J. G. Zhu. A vertical MRAM free of write disturbance. *IEEE Trans. Magn.*, 39:2854–2856, 2003.

[42] M. Julliere. Tunneling between ferromagnetic films. *Phys. Lett. A*, 54:225–226, 1975.

[43] J. S. Moodera, L. R. Kinder, T. M. Wong, and R. Meservey. Large magnetoresistance at room temperature in ferromagnetic thin film tunnel junctions. *Phys. Rev. Lett.*, 74:3273–3276, 1995.

[44] T. Miyazaki and N. Tezuka. Spin polarized tunneling in ferromagnet/insulator/ferromagnet junctions. *J. Magn. Magn. Mater.*, 151:403–410, 1995.

[45] J. S. Moodera and G. Mathon. Spin polarized tunneling in ferromagnetic junctions. *J. Magn. Magn. Mater.*, 200:248–273, 1999.

[46] A. Saffarzadeh. Tunnel magnetoresistance in double spin filter junctions. *J. Phys. : Cond. Matt.*, 15:3041–3051, 2003.

[47] J. C. Slonczewski. Conductance and exchange coupling of two ferromagnets separated by a tunneling barrier. *Phys. Rev. B*, 39:6995–7002, 1989.

[48] S. S. P. Parkin, C. Kaiser, A. Panchula, P. M. Rice, B. Hughes, M. Samant, and S. Yang. Giant tunnelling magnetoresistance at room temperature with Mgo (100) tunnel barriers. 3:862–867, 2004.

[49] B. G. Park, T. D. Lee, T. H. Lee, C. G. Kim, and C. O. Kim. Magnetic tunnel junctions with Hf oxide and modified Hf oxide tunnel barriers. *J. Appl. Phys.*, 93:6423–6425, 2003.

[50] Z. Li, C. de Groot, and J. H. Moodera. Gallium oxide as an insulating barrier for spin-dependent tunneling junctions. *Appl. Phys. Lett.*, 77:3630–3632, 2000.

[51] J. S. Parker, P. G. Ivanov, D. M. Lind, and P. Xiong. Large inverse magnetoresistance of CrO_2/Co junctions with an artificial barrier. *Phys. Rev. B*, 69(220413), 2004.

[52] P. LeClair, J. K. Ha, H. J. M. Swagten, J. T. Kohlhepp, and C. H. van de Vin. Large magnetoresistance using hybrid spin filter devices. *Appl. Phys. Lett.*, 80:625–627, 2002.

[53] P. Seneor, A. Fert, J. L. Maurice, F. Montaigne, F. Petroff, and A. Vaures. Large magnetoresistance in tunnel junctions with an iron oxide electrode. *Appl. Phys. Lett.*, 74:4017–4019, 1999.

[54] K. Schwarz. CrO_2 predicted as a half-metallic ferromagnet. *J. Phys. F: Metal Phys.*, 16:L211–L215, 1986.

[55] Z. Zhang and S. Satpathy. Electron states, magnetism, and the verwey transition in magnetite. *Phys. Rev. B*, 44:13319–13331, 1991.

[56] J. H. Park, E. Vescovo, H. J. Kim, C. Kwon, R. Ramesh, and T. Venkatesan. Direct evidence for a half-metallic ferromagnet. *Nature*, 392:794–796, 1998.

[57] W. J. Gallagher and S. S. P. Parkin. Development of the magnetic tunnel junction MRAM at IBM: From first junctions to a 16-Mb MRAM demonstrator chip. *IBM J. of Res. and Dev.*, 50:5–23, 2006.

[58] N. Garcia, M. Munoz, and Y. W. Zhao. Magnetoresistance in excess of 200% in ballistic Ni nanocontacts at room temperature and 100 Oe. *Phys. Rev. Lett.*, 82:2923–2926, 1999.

[59] K. Hong and N. Giordano. New effects in ferromagnetic nanostructures. *J. Magn. Magn. Mater.*, 151:396–402, 1995.

[60] J. F. Gregg, W. Allen, K. Ounadjela, M. Viret, M. Hehn, S. M. Thompson, and J. M. D. Coey. Giant magnetoresistive effects in a single element magnetic thin film. *Phys. Rev. Lett.*, 77:1580–1583, 1996.

[61] M. Viret, D. Vignoles, D. Cole, J. M. D. Coey, W. Allen, D. S. Daniel, and J. F. Gregg. Spin scattering in ferromagnetic thin films. *Phys. Rev. B*, 53:8464–8468, 1996.

[62] P. M. Levy and S. Zhang. Resistivity due to domain wall scattering. *Phys. Rev. Lett.*, 79:5110–5113, 1997.

[63] T. Y. Chen, Y. Ji, C. L. Chien, and M. D. Stiles. Current-driven switching in a single exchange-biased ferromagnetic layer. *Phys. Rev. Lett.*, 93(026601), 2004.

[64] A. D. Kent, U. Rdiger, J. Yu, L. Thomas, and S. S. P. Parkin. Magnetoresistance, micromagnetism, and domain wall effects in epitaxial Fe and Co structures with stripe domains (invited). *J. Appl. Phys.*, 85:5243–5248, 1999.

[65] U. Ebels, A. Radulescu, Y. Henry, L. Piraux, and K. Ounadjela. Spin accumulation and domain wall magnetoresistance in 35 nm Co wires. *Phys. Rev. Lett.*, 84:983–986, 2000.

[66] T. Taniyama, I. Nakatani, T. Namikawa, and Yamazaki. Resistivity due to domain walls in Co zigzag wires. *Phys. Rev. Lett.*, 82:2780–2783, 1999.

[67] U. Ruediger, J. Yu, S. Zhang, A. D. Kent, and S. S. P. Parkin. Negative domain wall contribution to the resistivity of microfabricated Fe wires. *Phys. Rev. Lett.*, 80:5639–5642, 1998.

[68] J. B. A. N. van Hoof, K. M. Schep, A. Brataas, G. E. W. Bauer, and P. J. Kelly. Ballistic electron transport through magnetic domain walls. *Phys. Rev. B*, 59:138–141, 1999.

[69] P. A. E. Jonkers. Magnetoresistance in magnetic domain wall systems. *J. Magn. Magn. Mater.*, 247:178–186, 2002.

[70] V. K. Dugaev, J. Barna, A. Usakowski, and A. Turski. Electrons in a ferromagnetic metal with a domain wall. *Phys. Rev. B*, 65(224419), 2002.

[71] D. A. Allwood, G. Xiong, M. D. Cooke, C. C. Faulkner, D. Atkinson, N. Vernier, and R. P. Cowburn. Submicrometer ferromagnetic NOT gate and shift register. *Science*, 296:2003–2006, 2002.

[72] C. H. Marrows and B. C. Dalton. Spin mixing and spin-current asymmetry measured by domain wall magnetoresistance. *Phys. Rev. Lett.*, 92(097206), 2004.

[73] C. Yu, S. F. Lee, J. L. Tsai, E. W. Huang, T. Y. Chen, Y. D. Yao, Y. Liou, and C. R. Chang. Study of domain wall magnetoresistance by submicron patterned. *J. Appl. Phys.*, 93:8761–8763, 2003.

[74] S. H. Florez, M. Dreyer, K. Schwab, C. Sanchez, and R. D. Gomez. Magnetoresistive effects in planar NiFe nanoconstrictions. *J. Appl. Phys.*, 95:6720–6722, 2004.

[75] A. Moser, K. Takano, D. T. Margulies, M. Albrecht, Y. Sonobe, Y. Ikeda, S. Sun, and E. E. Fullerton. Magnetic recording: advancing into the future. *J. Phys. D: Appl. Phys.*, 35:R157–R167, 2002.

[76] R. D. Wood and H. Takano. Prospects for magnetic recording over the next 10 years (invited). *Proceedings of IEEE International Magnetics Conference (INTERMAG) 2006*, pages CA–01, 2006.

[77] Hitachi Global Storage. Conventional media and the superparamagnetic limit. http://www.hitachigst.com/hdd/research/storage/pm/pm1.html.

[78] R. Wood, Y. Sonobe, Z. Jin, and B. Wilson. Perpendicular recording: the promise and the problems. *J. Magn. Magn. Mater.*, 235:1–9, 2001.

[79] A. Moser, C. Bonhote, Q. Dai, H. Do, B. Knigge, Y. Ikeda, Q. Le, B. Lengsfield, S. MacDonald, J. Li, V. Nayak, R. Payne, M. Schabes, N. Smith, K. Takano,

C. Tsang, P. van der Heijden, W. Weresin, M. Williams, and M. Xiao. Perpendicular magnetic recording technology at 230 Gbit/in^2. *J. Magn. Magn. Mater.*, 303:271–275, 2006.

[80] C. A. Ross. Patterned magnetic recording media. *Annu. Rev. Mater. Res.*, 31:203–235, 2001.

[81] M. Albrecht, S. Anders, T. Thomson, C. T. Rettner, M. E. Best, A. Moser, and B. D. Terris. Thermal stability and recording properties of sub-100 nm patterned CoCrPt perpendicular media. *J. Appl. Phys.*, 91(10):6845–6847, 2002.

[82] E. F. Wassermann, M. Thielen, S. Kirsch, A. Pollmann, H. Weinforth, and A. Carl. Fabrication of large scale periodic magnetic nanostructures. *J. Appl. Phys.*, 83:1753–1757, 1998.

[83] P. Candeloro, R. Kumar, M. Altissimo, L. Businaro, E. Di Fabrizio, M. Conti, G. Gubbiotti, G G. Carlotti, A. Gerardino, and R. Zivieri. X-ray lithography patterning of magnetic materials and their characterization. 42:3802–3806, 2003.

[84] D. Chen and T. Ye. Modern lithography techniques (a review). *Nuclear Techniques*, 27:81–86, 2004.

[85] A. K. Bates, M. Rothschild, T. M. Bloomstein, T. H. Fedynyshyn, R. R. Kunz, V. Liberman, and M. Switkes. Review of technology for 157-nm lithography. *IBM J. of Res. and Dev.*, 45:605–614, 2001.

[86] R. M. H. New, R. F. W. Pease, and R. L. White. Submicron patterning of thin cobalt films for magnetic storage. *J. Vac. Sci. Techn. B*, 12:3196–3201, 1994.

[87] B. D. Terris and T. Thomson. Nanofabricated and self-assembled magnetic structures as data storage media. *J. Phys. D: Appl. Phys.*, 38:R199–R222, 2005.

[88] J. J. M. Ruigrok, R. Coehoorn, S. R. Cumpson, and H. W. Kesteren. Disk

recording beyond 100 Gb/in^2: Hybrid recording? (invited). *J. Appl. Phys.*, 87:5398–5403, 2000.

[89] S. Sun, C. B. Murray, D. Weller, L. Folks, and A. Moser. Monodisperse FePt nanoparticles and ferromagnetic FePt nanocrystal superlattices. *Science*, 287:1989–1992, 2000.

[90] E. W. Pugh, D. L. Critchlow, R. A. Henle, and L. A. Russell. Solid-state memory development in IBM. *IBM J. of Res. and Dev.*, 25:585–602, 1981.

[91] M. Durlam, D. Addie, J. Akerman, B. Butcher, P. Brown, J. Chan, M. DeHerrera, B.N. Engel, B. Feil, G. Grynkewich, , J. Janesky, M. Johnson, K. Kyler, J. Moband J. Martin, K. Nagel, J. Ren, N.D. Rizzo, T. Rodriguez, L. Savtchenko, J. Salter, J.M. Slaughter, K. Smith, J.J. Sun, M. Lien, K. Papworth, P. Shah, W. Qin, R. Williams, L. Wise, and S. Tehrani. A 0.18 μm 4Mb toggling MRAM. *IEDM Tech. Digest*, pages 34.6.1–34.6.3, 2003.

[92] D. C. Worledge. Single-domain model for toggle MRAM. *IBM J. of Res. and Dev.*, 50:69–79, 2006.

[93] Toshiba corporation and NEC Corporation. Toshiba and nec develop world's fastest, highest density mram. Press Release, February 2006.

[94] J.M. Slaughter, R.W. Dave, M. Durlam, G. Kerszykowski, K. Smith, K. Nagel, B. Feil, J. Calder, M. DeHerrera, B. Garni, and S. Tehrani. High speed toggle MRAM with MgO-based tunnel junctions. *IEEE International Electron Devices Meeting*, pages 35.7.1–35.7.3, 2005.

[95] T. W. Andre, J. J. Nahas, C. K. Subramanian, B. J. Garni, H. S. Lin, A. Omair, and W. L. Martino. A 4-Mb 0.18-μm 1T1MTJ toggle MRAM with balanced three input sensing scheme and locally mirrored unidirectional write drivers. *IEEE J. of Sol. St. Circ.*, 40(1):301–309, 2005.

[96] I. L. Prejbeanu, W. Kula, K. Ounadjela, R. C. Sousa, O. Redon, B. Dieny, and J. P. Nozieres. Thermally assisted switching in exchange-biased storage layer magnetic tunnel junctions. *IEEE Trans. Magn.*, 40(4):2625–2627, 2004.

[97] J. Z. Sun. Spin angular momentum transfer in currentperpendicular nanomagnetic junctions. *IBM J. of Res. and Dev.*, 50:81–100, 2006.

[98] G. Schmidt. Concepts for spin injection into semiconductors - a review. *J. Phys. D: Appl. Phys.*, 38:R107–R122, 2005.

[99] M. Johnson. The bipolar spin transistor. *Nanotechnology*, 7:390396, 1996.

[100] S. Datta and B. Das. Electronic analog of the electro-optic modulator. *Appl. Phys. Lett.*, 56(7):665–667, 1990.

[101] K. Saraswat. How far can we push Si CMOS? what lies beyond? Lecture on Future Devices. Department of Electrical Engineering. Stanford University, 2006.

[102] B. A. Bernevig and S. Zhang. Toward dissipationless spin transport in semiconductors. *IBM J. of Res. and Dev.*, 50:141–148, 2006.

[103] D. J. Monsma, J. C. Lodder, Th. J. A. Popma, and B. Dieny. Perpendicular hot electron spin-valve effect in a new magnetic field sensor: The spin-valve transistor. *Phys. Rev. Lett.*, 74(26):5260–5263, 1995.

[104] S. van Dijken, X. Jiang, and S. S. P. Parkin. Room temperature operation of a high output current magnetic tunnel transistor. *Appl. Phys. Lett.*, 80(18):3364–3366, 2002.

[105] S. Sugahara and M. Tanaka. Spin MOSFETs as a basis for spintronics. *ACM Transactions on Storage*, 2(2):197219, 2006.

[106] J. Fabian, I. Zutic, and S. Das Sarma. Magnetic bipolar transistor. *Appl. Phys. Lett.*, 84:85–87, 2004.

[107] Y. W. Huang, C. K. Lo, Y. D. Yao, L. C. Hsieh, and J. H. Huang. Spin-valve transistor. *J. Appl. Phys.*, 97:10D504, 2005.

[108] B. E. Kane. A silicon-based nuclear quantum computer. *Nature*, 393:133–137, 1998.

[109] S. M. Sze. *Semiconductor Devices. Physics and Technology.* John Wiley and Sons, 1985.

[110] G. Oskam, J. G. Long, A. Natarajan, and P. C. Searson. Electrochemical deposition of metals onto silicon. *J. Phys. D: Appl. Phys.*, 31:1927–1949, 1998.

[111] A. P. O'Keeffe, O. I. Kasyutich, W. Schwarzacher, L. S. de Oliveira, and A. A. Pasa. Giant magnetoresistance in multilayers electrodeposited on n - Si. *Appl. Phys. Lett.*, 73:1002–1004, 1998.

[112] M. L. Munford, M. L. Sartorelli, L. Seligman, , and A. A. Pasa. Morphology and magnetic properties of Co thin films electrodeposited on Si. *J. Electrochem. Soc.*, 149:C274–C279, 2002.

[113] A.A. Pasa and W. Schwarzacher. Electrodeposition of thin films and multilayers on silicon. *Phys. Stat. Sol.*, 173:73–84, 1999.

[114] C. Wisniewski, I. Denicolo, and I. A. Hummelgen. Electrochemically deposited cobalt thin-films on p-type silicon and its characterization. *J. Electrochem. Soc.*, 142:3889–3892, 1995.

[115] M. L. Sartorelli, A. Q. Schervenski, R. G. Delatorre, P. Klauss, A. M. Maliska, and A. A. Pasa. Cu-Ni thin films electrodeposited on Si: Composition and current efficiency. *Phys. Stat. Sol.*, 187:91–95, 2001.

[116] G. R. Pattanaik, D. K. Pandya, and S. C. Kashyap. Preparation of Cu-Co alloy thin films on n-Si by galvanostatic DC electrodeposition. *J. Electrochem. Soc.*, 149:C363–C369, 2002.

[117] J. W. Chang and L. T. Romankiw. Electrodeposited superlattices of CoFe/Cu and NiFe/Cu on n-type (111) Si single crystal wafers. *Proceedings - Electrochemical Society PV*, 94-6:223–232, 1993.

[118] A. Imanishi, K. Morisawa, and Y. Nakato. Formation of nanosized rodlike Ni clusters by electrodeposition on H-terminated Si(111) surfaces. *Electrochem. Sol. State Lett.*, 4:C69–C72, 2001.

[119] C. A. Moina and M. Vazdar. Electrodeposition of nano-sized nuclei of mangnetic Co-Ni alloys onto n-Si (100). *J. Electrochem. Comm.*, 3:159–163, 2001.

[120] N. Takano, N. Hosoda, T. Yamada, and T. Osaka. Effect of oxidized silicon surface on chemical deposition of nickel on n-type silicon wafer. *Electrochim. Acta*, 44:3743–3749, 1999.

[121] N. Takano, D. Niwa, T. Yamada, and T. Osaka. Nickel deposition behavior on n-type silicon wafer for fabrication of minute nickel dots. *Electrochim. Acta*, 45:3263–3268, 1999.

[122] D. Niwa, T. Homma, and T. Osaka. Deposition mechanism of Ni on Si(100) surfaces in aqueous alkaline solution. *J. Phys. Chem. B*, 108:9900–9904, 2004.

[123] M. Schlesinger and M. Paunovic et al. *Modern Electroplating, Fourth Edition.* John Wiley and Sons, 2000.

[124] P. N. Bartlett, M. A. Ghanem, I. S. El Hallag, P. de Groot, and A. Zhukov. Electrochemical deposition of macroporous magnetic networks using colloidal templates. *J. Mater. Chem.*, (13):2596–2602, 2003.

[125] G. Marshall, E. Mocskos, F. V. Molina, and S. Dengra.

[126] L. J. Gao, P. Ma, K. M. Novogradecz, and P. R. Norton.

[127] R. G. Delatorre, M. L. Sartorelli, A. Q. Schervenski, A. A. Pasa, and S. Guths.

[128] X. Zhang, E. Garfunkel, Y. J. Chabal, S. B. Christman, and E. E. Chaban). Stability of HF-etched S(100) surfaces in oxygen ambient. *Appl. Phys. Lett.*, 79(24):4051–4053, 2001.

[129] S. A. Doherty, J. G. Zhu, M. Dugas, S. Anderson, and J. Tersteeg. Correlation between evolving magnetic and morphological properties in magnetic multilayers. *IEEE Trans. Magn.*, 34(4):840–842, 1998.

[130] G. M. Whitesides and B. Grzybowski. Self-assembly at all scales. *Science*, 295:2418–2421, 2002.

[131] P. N. Bartlett, P. N. Birkin, M. A. Ghanem, P. de Groot, and M. Sawicki. The electrochemical deposition of nanostructured cobalt films from lyotropic liquid crystalline media. *J. Electrochem. Soc.*, 148:C119–C123, 2001.

[132] J. C. Hulteen and C. R. Martin. A general template-based method for the preparation of nanomaterials. *J. Mater. Chem.*, 7(7):1075–1087, 1997.

[133] T. Thurn-Albrecht, J. Schotter, G. A. Kastle, N. Emley, T. Shibauchi, L. Krusin-Elbaum, K. Guarini, C. T. Black, M. T. Tuominen, and T. P. Russell. Ultrahigh-density nanowire arrays grown in self-assembled diblock copolymer templates. *Science*, 290:2126–2129, 2000.

[134] P. N. Bartlett, P. R. Birkin, and M. A. Ghanem. Electrochemical deposition of macroporous platinum, palladium and cobalt films using polystyrene latex sphere templates. *Chem. Commun.*, (17):1671–1672, 2000.

[135] L. Xu, W. L. Zhou, C. Frommen, R. H. Baughman, A. A. Zakhidov, L. Malkinski, J. Q. Wang, and J. B. Wiley. Electrodeposited nickel and gold nanoscale metal meshes with potentially interesting photonic properties. *Chem. Commun.*, pages 997–998, 2000.

[136] J. Cheng, C.A. Ross, and A. Mayes. Nanostructure engineering by templated self-assembly. *Nature Materials*, 3(11):823–828, 2004.

[137] S. M. Yang and G. A. Ozin. Opal chips: vectorial growth of colloidal crystal patterns inside silicon wafers. *Chem. Commun.*, pages 2507–2508, 2000.

[138] D. Wang and H. Mohwald. Template-directed colloidal self-assembly the route to top-down nanochemical engineering. *J. Mater. Chem.*, 14:459–468, 2004.

[139] P. Ferrand, M. Egen, B. Griesebock, J. Ahopelto, M. Muller, R. Zentel, S. G. Romanov, and C. M. Sotomayor. Self-assembly of three-dimensional photonic crystals on structured silicon wafers. *Appl. Phys. Lett.*, 81(15):2689–2691, 2002.

[140] J. P. Hoogenboom, C. Retif, E. de Bres, M. van de Boer, A. K. van Langen-Suurling, J. Romijn, and A. van Blaaderen. Template-induced growth of

close-packed and non-close-packed colloidal crystals during solvent evaporation. *Nanoletters*, 4(2):205–208, 2004.

[141] Y. H. Ye, S. Badilescu, V. V. Truong, P. Rochon, and A. Natansohn. Self-assembly of colloidal spheres on patterned substrates. *Appl. Phys. Lett.*, 79(6):872–874, 2001.

[142] J. Zhang, A. Alsayed, K. H. Lin, S. Sanyal, F. Zhang, W.J. Pao, V. S. K. Balagurusamy, P. A. Heiney, and A. G. Yodha. Template-directed convective assembly of three-dimensional face-centered cubic colloidal crystals. *Appl. Phys. Lett.*, 81(17):3176–3178, 2001.

[143] J. Y. Cheng, C. A. Ross, V. Z.-H. Chan, E. L. Thomas, R. G. H. Lammertink, and G. J. Vancso. Formation of a cobalt magnetic dot array via block copolymer lithography. *Adv. Mater.*, 13(15):1174–1178, 2001.

[144] S. M. Weekes, F. Y. Ogrin, and W. A. Murray. Fabrication of large-area ferromagnetic arrays using etched nanosphere lithography. *Langmuir*, 20:11208–11212, 2004.

[145] M. E. Abdelsalam, P. N. Bartlett, J. J. Baumberg, and S. Coyle. Preparation of arrays of isolated spherical cavities by self-assembly of polystyrene spheres on self-assembled pre-patterned macroporous films. *Adv. Mater.*, 16(1):90–93, 2004.

[146] A.A. Zhukov, M.A. Ghanem, A.V. Goncharov, P.A.J. de Groot, I.S. El-Hallag, P.N. Bartlett, R. Boardman, and H. Fangohr. Coercivity of 3D nanoscale magnetic arrays from self-assembly template methods. *J. Magn. Magn. Mater.*, 272-276:1621–1622, 2004.

[147] Y. Yin, Y. Lu, B. Gates, and Y. Xia. Template-assisted self-assembly: A practical route to complex aggregates of monodispersed colloids with well-defined sizes, shapes, and structures. *J. Am. Chem. Soc.*, 123:8718–8729, 2001.

[148] R. K. Golding, P. C. Lewis, E. Kumacheva, M. Allard, and E. H. Sargent. In situ study of colloid crystallization in constrained geometry. *Langmuir*, 20:1414–1419, 2004.

[149] M. E. Kiziroglou, A. A. Zhukov, M. Abdelsalam, X. Li, P. A. J. de Groot, P. N. Bartlett, and C. H. de Groot. Electrodeposition of Ni-Si Schottky barriers. *IEEE Trans. Magn.*, 41(10):2639–2641, 2005.

[150] N. D. Denkov, O. D. Velev, P. A. Kralchevsky, I. B. Ivanov, J. H. Yoshimura, and K. Nagayamat. Mechanism of formation of two-dimensional crystals from latex particles on substrates. *Langmuir*, 8:3183–3190, 1992.

[151] J. H. Conway and N. J. A. Sloane. *Sphere packings, lattices and groups.* Springer-Verlag, 1988.

[152] C. A. Fustin, G. Glasser, H. W. Spiess, and U. Jonas. Parameters influencing the templated growth of colloidal crystals on chemically patterned surfaces. *Langmuir*, 20(21):9114–9123, 2004.

[153] R. Wilson, T. J. Karle, I. Moerman, and T. F. Krauss. Efficient photonic crystal Y-juctions. *J. Opt. A: Pure Appl. Opt.*, 5:S76–S80, 2003.

[154] J. D. Joannopoulos, P. R. Villeneuve, and S. Fan. Photonic crystals: putting a new twist on light. *Nature*, 386:143–149, 1997.

[155] X. Jiang S. van Dijken and S. S. P. Parkin. Comparison of magnetocurrent and transfer ratio in magnetic tunnel transistors with spin-valve bases containing Cu and Au spacer layers. *Appl. Phys. Lett.*, 82(5):775–777, 2003.

[156] S. M. Sze. *Physics of Semiconductor Devices.* Wiley Interscience, 1981.

[157] E. H. Rhoderick and R. H. Williams. *Metal-Semiconductor Contacts, Second Edition.* Clarendon Press, Oxford, 1988.

[158] B. van Zeghbroeck. Principles of semiconductor devices. http://www.colorado.edu/ bart/book.

[159] R. T. Tung. Electron Transport at metal-semiconductor interfaces: General Theory. *Phys. Rev. B*, 45(23):13509–13523, 1992.

[160] J. H. Werner and H. H. Guttler. Barrier inhomogeneities at Schottky contacts. *J. Appl. Phys.*, 69(3):1522–1533, 1991.

[161] A. N. Saxena. Forward current-voltage characteristics of Schottky barriers on n-type Silicon. *Surface Science*, 13:151–171, 1969.

[162] M. Yoshimura, I. Ono, and K. Ueda. Initial stages of Ni reaction on Si (100) and H-terminated Si (100) surfaces. *Appl. Surf. Sc.*, 130-132:276–281, 1998.

[163] J. M. Shannon. Reducing the effective height of a schottky barrier using low-energy ion implantation. *Appl. Phys. Lett.*, 24(8):369–371, 1974.

[164] A. G. McCormack, M. J. Pomeroy, and V. J. Cunnane. Microstructural development and surface characterization of electrodeposited Nickel/Yttria composite coatings. *J. Electrochem. Comm.*, 150(5):C356–C361, 2003.

[165] H. B. Michaelson. The work function of the elements and its periodicity. *J. Appl. Phys.*, 48(11):4729–4733, 1977.

[166] F. J. Castano, K. Nielsch, C. A. Ross, J. W. A. Robinson, and R. Krishnan. Anisotropy and magnetotransport in ordered magnetic antidot arrays. *Appl. Phys. Lett.*, 85(14):2872–2874, 2004.

[167] A. A. Zhukov, A. V. Goncharov, P. A. J. de Groot, M. A. Ghanem, P. N. Bartlett, R. Boardman, H. Fangohr, V. Novosad, and G. Karapetrov. Oscillatory thickness dependence of the coercive field in magnetic three-dimensional antidot arrays. *Appl. Phys. Lett.*, 88:062511, 2006.

[168] M. Tanaka, E. Saitoh, H. Miyajima, and T. Yamaoka. Magnetization process and magnetic structure in a NiFe honeycomb nano-network. *J. Magn. Magn. Mater.*, 282:22–24, 2004.

[169] H. Jaffres and A. Fert. Spin injection from a ferromagnetic metal into a semiconductor. *J. Appl. Phys.*, 91:8111–8113, 2002.

[170] A. T. Hanbicki, O. M. J. van t Erve, R. Magno, G. Kioseoglou, C. H. Li, B. T. Jonker, G. Itskos, R. Mallory, M. Yasar, and A. Petrou. Analysis of the transport process providing spin injection through an Fe/AlGaAs Schottky barrier. *Appl. Phys. Lett.*, 82:4092–4094, 2003.

[171] A. M. Bratkovsky and V. V. Osipov. Efficient spin injection and extraction in modified reverse and forward biased ferromagnetic-semiconductor junctions and low-power ultrafast spin injection devices. *Appl. Phys. A: Mater. Sci. Proc.*, 80:1237–1246, 2005.

[172] G Schmidt and L W. Molenkamp. Spin injection into semiconductors, physics and experiments. *Semicond. Sci. Technol.*, 17:310–321, 2002.

[173] M. E. Kiziroglou, A. A. Zhukov, X. Li, D. C. Gonzalez, P. A. J. de Groot, P. N. Bartlett, and C. H. de Groot. Analysis of thermionic emission from electrodeposited Ni-Si Schottky barriers. Accepted. *Sol. St. Comm.*, 2006.

[174] F. A. Padovani and R. Stratton. Field and thermionic-field emission in Schottky barriers. *Solid-State Electronics*, 9:69, 1966.

[175] S. J. Steinmuller, C. M. Gurtler, G. Wastlbauer, and J. A. C. Bland. Separation of electron spin filtering and magnetic circular dichroism effects in photoexcitation studies of hybrid ferromagnet/GaAs Schottky barrier structures. *Phys. Rev. B*, 72:045301, 2005.

Appendix A

Potential uniformity on Si electrodes

In electrodeposition experiments, it is usually the case that the cathode (the electrode on which the electrodeposition is taking place) is connected to the power supply via a "crocodile" clip. Part of the substrate is immersed into the electrolyte for deposition and the rest is exposed to the air. Moreover, the immersed part is covered by an isolation layer, leaving only a small window of a particular size to be exposed to the electrolyte. This setup is illustrated in Fig. A.1.

In this setup, the potential on the electrodeposition surface (shadowed area in Fig. A.1, S_t) will not be uniform, because of the voltage drop that the flowing current causes. This is of particular interest because it may lead to non-uniform material deposition. In the rest of this appendix, the potential distribution on the electrodeposition surface (S_t) will be investigated.

A.1 Assumptions-Conventions

For the calculation of the potential on S_t, the following assumptions are made:

1. The potential will vary only with the distance from the top of the cathode electrode. This means that the horizontal surfaces in the cathode will be considered as constant potential surfaces.

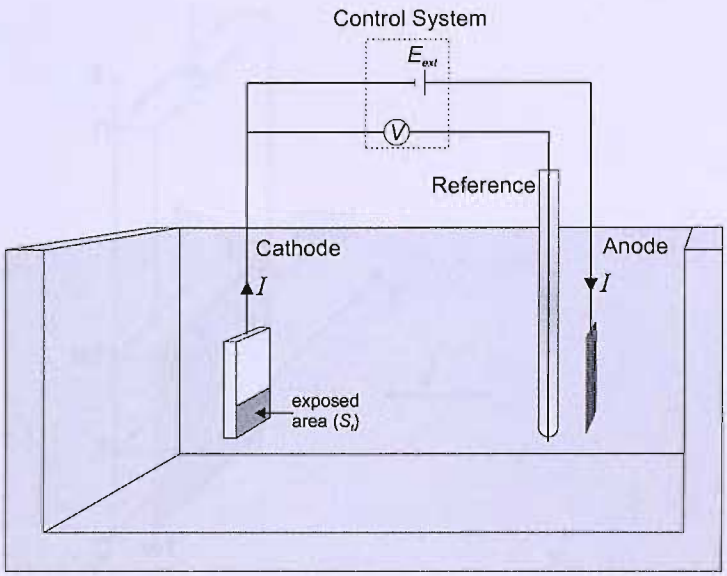

Figure A.1: *Simple setup illustration of a 3- electrode electrodeposition.*

2. The reference potential is that of the anode: $\phi_{anode} = 0V$.

3. The $I-V$ characteristic of the electrolysis phenomenon is the same for all spots of S_t.

4. Without affecting the universality of the calculations it will be assumed that the width of S_t is equal to the width of the whole cathode.

A.2 Formation of General Equations

Here, the equations needed for the potential distribution calculation are formed. The geometry of the cathode is illustrated in Fig. A.2. The length of the electrodeposition area (window) is wl, the thickness is wt and the height is wh. The height of the whole cathode is h.

According to the assumptions made in section A.1, the potential on the cathode will only be a function of z:

$$\phi = \phi(z) \tag{A.1}$$

It is important to note at this point that ϕ corresponds to the absolute value of

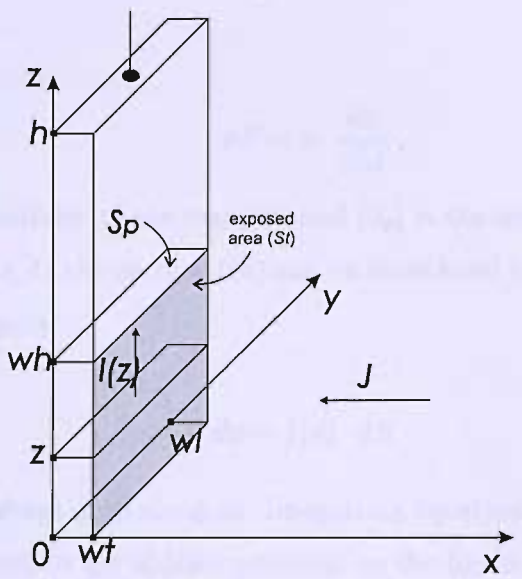

Figure A.2: *Geometry of the Si electrode. The shaded area (S_t) is exposed to the solution while the rest of the electrode's surface is isolated.*

the potential. The current density J perpendicular to the surface S_t will be a function of the potential:

$$J = f(\phi) \tag{A.2}$$

where function f : will depend on electrolysis parameters. The current flowing in the electrode will be perpendicular to the constant-potential surfaces (S_p) and will depend only on z. At a certain surface z within the surface S_t, the current will be equal to that coming into the electrode below that point:

$$I(z) = \int_{S_z} J dS \tag{A.3}$$

where the surface S_z is defined as the part of S_t under point z. Note that for $z \geq wh$, S_z coincides with S_t. Mathematically

$$S_z : \begin{cases} 0 \leq y \leq wl \vee 0 \leq z \leq Z, \ when \ 0 \leq Z < wh \\ \\ 0 \leq y \leq wl \vee 0 \leq z \leq wh, \ when \ Z \geq wh \end{cases} \tag{A.4}$$

On the other hand, along a fundamental vertical length dz, the resistance of the

cathode will be:

$$dR = \rho \cdot \frac{dz}{|S_p|} \tag{A.5}$$

where ρ is the resistivity of the material and $|S_p|$ is the area of the cross-section of the cathode. Along dz the current $I(z)$ can be considered to be constant and Ohm's law will directly apply:

$$d\phi = I(z) \cdot dR \tag{A.6}$$

where $d\phi$ is the voltage drop along dz. Integrating equation A.6, the potential of the cathode with respect to the applied potential on the top of the cathode ($z = h$) can be calculated:

$$\int_z^h d\phi = \int_z^h I(z) dR \tag{A.7}$$

Using equation A.5:

$$\phi(h) - \phi(z) = \frac{\rho}{|S_p|} \cdot \int_z^h I(z) dz \Leftrightarrow \tag{A.8}$$

$$\phi(z) = \phi(h) - \frac{\rho}{|S_p|} \cdot \int_z^h I(z) dz \tag{A.9}$$

Equation A.9 relates the potential $\phi(z)$ to the current $I(z)$. Using a modelling function for the electrolysis electrical behaviour (function f :, equation A.3) one can obtain another equation relating $\phi(z)$ and $I(z)$ using equations A.1 to A.3. The resulting differential system can be solved to give the potential and the current distribution along the cathode. For this solution, the following boundary conditions should be used:

$$I(0) = 0 \tag{A.10}$$

$$\phi(wh)^- = \phi(wh)^+ \tag{A.11}$$

In the following section a simple function f : will be used to calculate the potential and current distribution functions.

A.3 Calculation of the Potential Distribution

Here, the potential distribution along the cathode will be calculated, assuming that the electrolysis phenomenon is such that the function f : in equation A.3 is:

$$f(\phi) = \begin{cases} k(\phi - \phi_T), \ \phi > \phi_T \\ \\ 0, \ \phi \leq \phi_T \end{cases} \tag{A.12}$$

where k is a constant of $\Omega^{-1}\ cm^{-2}$ and ϕ_T is a threshold value of the potential. The potential along z, $\phi(z)$ will satisfy the following conditions:

$$\phi(z) \leq \phi(h), \ \forall \ z \ \epsilon[0, h) \tag{A.13}$$

$$if \ \phi(h) > \phi_T \ then \ \phi(z) > \phi_T, \ \forall \ z \ \epsilon[0, h) \tag{A.14}$$

The first condition is obvious while the second is derived from the demand that the derivative of the potential across the homogeneous cathode material must be continuous. Equation A.12 can now be written as:

$$f(\phi) = \begin{cases} k(\phi - \phi_T), \ \phi(h) > \phi_T \\ \\ 0, \ \phi(h) \leq \phi_T \end{cases} \tag{A.15}$$

If $\phi(h) \leq \phi_T$, there is no current flowing through the cathode. The potential is constant and equal to $\phi(h)$. This is a case where electrodeposition doesn't take place. In the following treatment, it will be assumed that $\phi(h) > \phi_T$ and, consequently (from equation A.14):

$$\phi z > \phi_T, \ \forall \ z \ \epsilon[0, h] \tag{A.16}$$

Using equations A.1 to A.3 and A.12 the following expression is derived:

$$I(z) = k \cdot \int_{S_z} \phi(z) \cdot dS - k \cdot \phi_T \cdot |S_z| \tag{A.17}$$

where $|S_z|$ is the area of S_z in cm^2. As long as ϕ : is a function of z only, the surface integral in equation A.12 can be transformed to an integral of z. Considering that S_z is defined by equation A.4 it comes out that:

$$I(z) = \begin{cases} k \cdot wl \cdot \int_0^z \phi(z) \cdot dz - k \cdot \phi_T \cdot wl \cdot z, \ 0 \leq z < wh \\ \\ k \cdot wl \cdot \int_0^{wh} \phi(z) \cdot dz - k \cdot \phi_T \cdot wl \cdot wh, z \geq wh \end{cases} \tag{A.18}$$

For $z \geq wh$ the current is constant and will be denoted with I_t:

$$I_t = k \cdot wl \cdot \int_0^{wh} \phi(z) \cdot dz - k \cdot \phi_T \cdot wl \cdot wh \tag{A.19}$$

Equations A.9 and A.18 consist a differential system of $\phi(z)$ and I(z). This system is rewritten here for easier reference:

$$I(z) = \begin{cases} k \cdot wl \cdot \int_0^z \phi(z) \cdot dz - k \cdot \phi_T \cdot wl \cdot z, \ 0 \leq z < wh \\ \\ I_t, wh \leq z \leq h \end{cases} \tag{A.20}$$

$$\phi(z) = \phi(h) - \tfrac{\rho}{|S_p|} \cdot \int_z^k I(z)dz$$

This system will be treated separately for $0 \leq z < wh$ and for $wh \leq z \leq h$:

A.3.1 For $0 \leq z < wh$

It will be:

$$\begin{aligned} I(z) &= k \cdot wl \cdot \int_0^z \phi(z) \cdot dz - k \cdot \phi_T \cdot wl \cdot z \\ \phi(z) &= \phi(h) - \tfrac{\rho}{|S_p|} \cdot \int_z^{wh} I(z)dz - \tfrac{\rho}{|S_p|} \cdot I_t \cdot (h - wh) \end{aligned} \tag{A.21}$$

Differentiating both these equations:

$$I'(z) = k \cdot wl \cdot \phi(z) - k \cdot \phi_T \cdot wl$$
$$\phi'(z) = \frac{\rho}{|S_p|} \cdot I(z) \tag{A.22}$$

The area $|S_p|$ can be substituted by the product $wt \cdot wl$. Differentiating again the first of those equations and using the second equation for $\phi'(z)$, a second order, homogeneous differential equation for $I(z)$ is derived:

$$I''(z) = \frac{k \cdot \rho}{wt} \cdot I(z) \tag{A.23}$$

Let:

$$\lambda = \sqrt{\frac{k \cdot \rho}{wt}} \tag{A.24}$$

Then, the differential equation A.23 takes the simple form:

$$I''(z) = \lambda^2 \cdot I(z) \tag{A.25}$$

The general solution of this equation will be:

$$I(z) = c_1 \cdot e^{\lambda \cdot z} + c_2 \cdot e^{-\lambda \cdot z} \tag{A.26}$$

where c_1 and c_2 are constants that can be determined using boundary conditions. Using the first of equations A.29 and equation A.27, the potential distribution for $0 \leq z < wh$ can be calculated:

$$\phi(z) = \frac{\lambda}{k \cdot wl} c_1 \cdot (e^{\lambda \cdot z} + c_2 \cdot e^{-\lambda \cdot z}) + \phi_T \tag{A.27}$$

Applying the boundary condition A.10 to equation A.27, it comes out that:

$$c_1 = -c_2 = c \tag{A.28}$$

The corresponding solution is as follows:

$$\left.\begin{array}{l} I(z) = c \cdot (e^{\lambda \cdot z} - \cdot e^{-\lambda \cdot z}) \\ \\ \phi(z) = \frac{\lambda \cdot c}{k \cdot wl} \cdot (e^{\lambda \cdot z} + e^{-\lambda \cdot z}) + \phi_T \end{array}\right| , 0 \leq z < wh \tag{A.29}$$

Next, $I(z)$ and $\phi(z)$ will be calculated for $z \geq wh$.

A.3.2 For $wh \leq z < h$

As mentioned before, the current in this region is constant:

$$I_t = I_t = k \cdot wl \cdot \int_0^{wh} \phi(z) \cdot dz - k \cdot \phi_T \cdot wl \cdot wh \tag{A.30}$$

Using equation A.29($\phi(z)$ is integrated in the interval $[0, wh]$), the value of I_t becomes:

$$I_t = c \cdot (e^{\lambda \cdot wh} - \cdot e^{-\lambda \cdot wh}) \tag{A.31}$$

From equation A.21, $\phi(z)$ can be derived:

$$\phi(z) = \frac{\rho \cdot I_t}{wt \cdot wl} \cdot (z - h) + \phi(h) \tag{A.32}$$

The corresponding solution for this case is as follows:

$$\left.\begin{array}{l} I(z) = I_t \\ \\ \phi(z) = \frac{\rho \cdot I_t}{wt \cdot wl} \cdot (z - h) + \phi(h) \end{array}\right| , wh \leq z \leq h \tag{A.33}$$

A.3.3 Constants

Before giving the general expressions for the calculated solutions, the constants c and I_t will be calculated. From the boundary condition A.11:

$$\frac{\lambda \cdot c}{k \cdot wl} \cdot (e^{\lambda \cdot wh} + e^{-\lambda \cdot wh}) + \phi_T = \frac{\rho \cdot I_t}{wt \cdot wl} \cdot (wh - h) + \phi(h) \tag{A.34}$$

Finally, from equations A.31 and A.34 it will be:

$$c = \frac{k \cdot wl \cdot wt \cdot (\phi(h) - \phi_T)}{\lambda \cdot wt \cdot (e^{\lambda \cdot wh} + e^{-\lambda \cdot wh}) - k \cdot \rho \cdot (wh - h) \cdot (e^{\lambda \cdot wh} - e^{-\lambda \cdot wh})} \tag{A.35}$$

$$I_t = \frac{k \cdot wl \cdot wt \cdot (e^{\lambda \cdot wh} - e^{-\lambda \cdot wh}) \cdot (\phi(h) - \phi_T)}{\lambda \cdot wt \cdot (e^{\lambda \cdot wh} + e^{-\lambda \cdot wh}) - k \cdot \rho \cdot (wh - h) \cdot (e^{\lambda \cdot wh} - e^{-\lambda \cdot wh})} \tag{A.36}$$

A.3.4 Summary

Here, the results of the analysis presented so far are summarised. It is noted that these results are obtained by modelling the electrolysis phenomenon with the equation A.12. The general expression for $\phi(z)$ will be:

$$\phi(z) = \begin{cases} \frac{\lambda \cdot c}{k \cdot wl} \cdot (e^{\lambda \cdot z} + e^{-\lambda \cdot z}) + \phi_T, \ 0 \leq z \leq wh \ and \ \phi(h) > \phi_T \\ \frac{\rho \cdot I_t}{wt \cdot wl} \cdot (z - h) + \phi(h), \ wh \leq z \leq h \ and \ \phi(h) > \phi_T \\ \phi(h), \phi(h) \leq \phi_T \end{cases} \tag{A.37}$$

The general expression for $I(z)$ will be:

$$I(z) = \begin{cases} c \cdot (e^{\lambda \cdot z} - \cdot e^{-\lambda \cdot z}), \ 0 \leq z \leq wh \ and \ \phi(h) > \phi_T \\ I_t, \ wh \leq z \leq h \ and \ \phi(h) > \phi_T \\ 0, \phi(h) \leq \phi_T \end{cases} \tag{A.38}$$

where c and I_t are given by the equations A.35 and A.36. I_t is also given by A.31 as a function of c. The parameters used in these expressions are summarized in the following table:

Table A.1: *Summary of Parameters.*

Parameter	Unit	Description
wt	cm	Thickness of the cathode
wl	cm	Length of the cathode
wh	cm	Height of the cathode exposed area
ρ	$\Omega\ cm$	Resistivity of the cathode
h	cm	Height of the cathode
k	$\Omega^{-2}\ cm^{-2}$	Defined by equation A.12
ϕ_T	V	Defined by equation A.12
$\phi(h)$	V	Potential at the cathode top (absolute value)
λ	cm^{-1}	Defined by equation A.24
c	A	Defined by equation A.35
I_t	A	Total cathode current (equation A.36)

A.4 Other Equations

Using the above results, some useful equations can be derived:

- Potential at the bottom of the cathode (absolute value):

$$\phi_b = \phi(0) = \frac{2 \cdot \lambda \cdot c}{k \cdot wl} + \phi_T \tag{A.39}$$

- Voltage drop along the exposed area:

$$\cdot V_{ea} = \phi(wh) - \phi(0) = \frac{\lambda \cdot c}{k \cdot wl} \cdot (e^{\lambda \cdot wh} + e^{-\lambda \cdot wh} - 2) \tag{A.40}$$

- Voltage drop along the whole cathode:

$$V_c = \phi(h) - \phi(0) = (\phi(h) - \phi_T) \cdot \frac{\lambda \cdot wt \cdot (e^{\lambda \cdot wh} + e^{-\lambda \cdot wh} - 2) - k \cdot \rho \cdot (wh - h) \cdot (e^{\lambda \cdot wh} - e^{-\lambda \cdot wh})}{\lambda \cdot wt \cdot (e^{\lambda \cdot wh} + e^{-\lambda \cdot wh}) - k \cdot \rho \cdot (wh - h) \cdot (e^{\lambda \cdot wh} - e^{-\lambda \cdot wh})} \tag{A.41}$$

- Potential at the top edge of the exposed area:

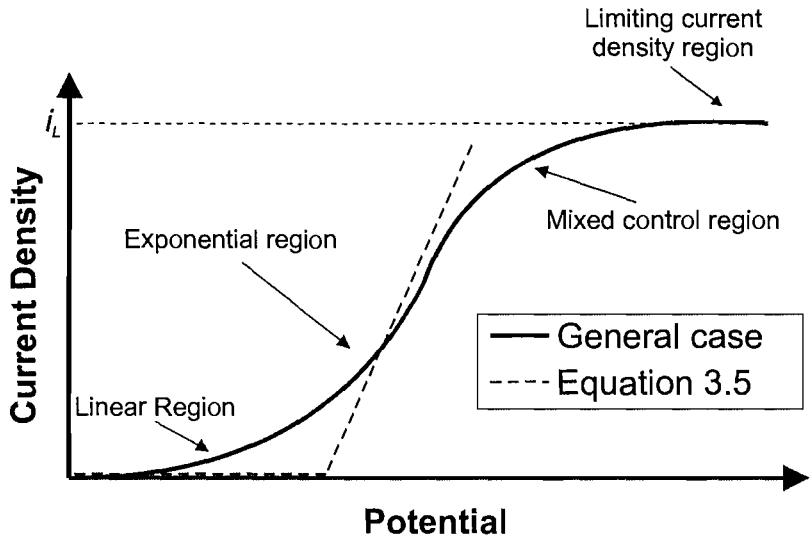

Figure A.3: *Four regions in the general current potential relationship of electrodeposition.*

$$\phi(wh) = \frac{\lambda \cdot c}{k \cdot wl} \cdot (e^{\lambda \cdot wh} + e^{-\lambda \cdot wh}) + \phi_T \tag{A.42}$$

It is noted that these equations stand only if $\phi(h) > \phi_T$. Also, $\phi(z)$ is the absolute value of the potential.

A.5 Choosing values for k and ϕ_T

Equation A.12 is an approximation of the real $I-V$ characteristic in electrodeposition. A general description of this characteristic is shown in Fig. A.3

The linear approximation corresponding to equation A.12 is shown as a dashed line in the above figure. A first approach in determining the values of k and ϕ_T would be:

$$\begin{aligned} k &= \tfrac{i_L - 0}{E_C} = \tfrac{i_L}{E_C} \\ \phi_T &= 0 \end{aligned} \tag{A.43}$$

Using just the typical order of magnitude for these parameters, the order of magnitude for k is obtained:

$$\begin{aligned} k &= \frac{10\ mA \cdot cm^{-2}}{1V} = 0.01\Omega^{-1} \cdot cm^{-2} \\ \phi_T &= 0 \end{aligned} \tag{A.44}$$

On the other hand, from early experimental results (11.02.04) for the mean electrodeposition current density, the followings experimental values for k have been obtained:

$$\begin{aligned} k_1 &= 0.00158\Omega^{-1} \cdot cm^{-2} \\ k_2 &= 0.00225\Omega^{-1} \cdot cm^{-2} \end{aligned} \tag{A.45}$$

Considering the above, the following values for k and ϕ_T will be assumed:

$$\begin{aligned} k &= 0.002\Omega^{-1} \cdot cm^{-2} \\ \phi_T &= 0\ V \end{aligned} \tag{A.46}$$

Appendix B

Lithographic Masks

B.1 Mask K989R (reticle)

A top view of the mask is shown in Fig. B.1. Its total area is $1cmx1cm$. The mask is divided into four square quarters. The exposing area is calculated to be 0.2 cm^2 per cell (1 cell includes all four quarters). The top - left quarter consists of diagonal lines and triangles. The size range of these structures is given in table B.1. The top - right quarter contains rings, circles, squares and lines of different sizes. The size ranges covered is given in table B.2. The bottom - left quarter is identical to the top - right quarter. Similarly, the bottom - right quarter is identical to the top left one. Fig. B.2 illustrates the various structures implemented by this mask.

Table B.1: *Size range for the structures of the top - left part of the mask k989r.*

Structure	Triangles		Lines
Dimension	Base	Height	Width
Minimum	10 μm	5 μm	1 μm
Maximum	40 μm	20 μm	20 μm

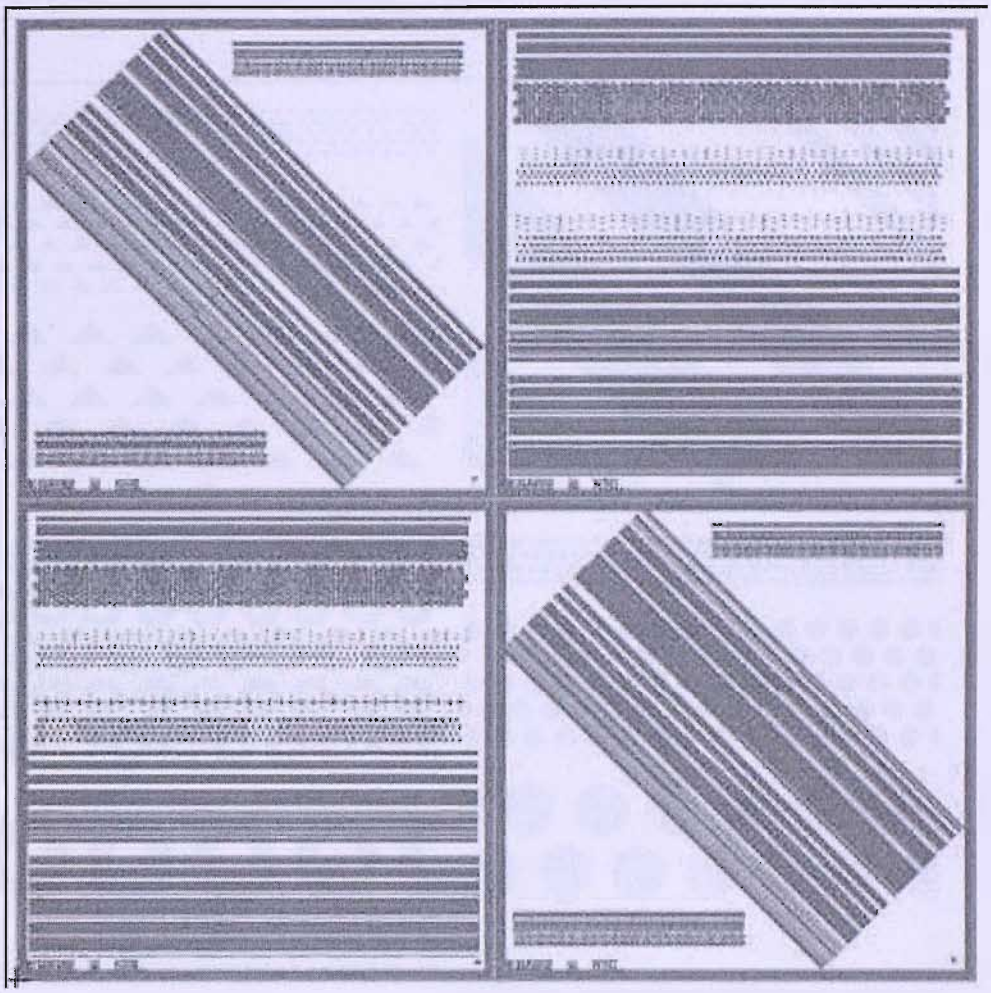

Figure B.1: *Top view of the mask k989r.*

Table B.2: *Size range for the structures of the top - right part of the mask k989r.*

Structure	Rings		Circles	Squares	Lines
Dimension	Inner Diameter	Outer Diameter	Diameter	Side	Width
Minimum	10 μm	20 μm	5 μm	5 μm	1 μm
Maximum	40 μm	80 μm	50 μm	50 μm	20 μm

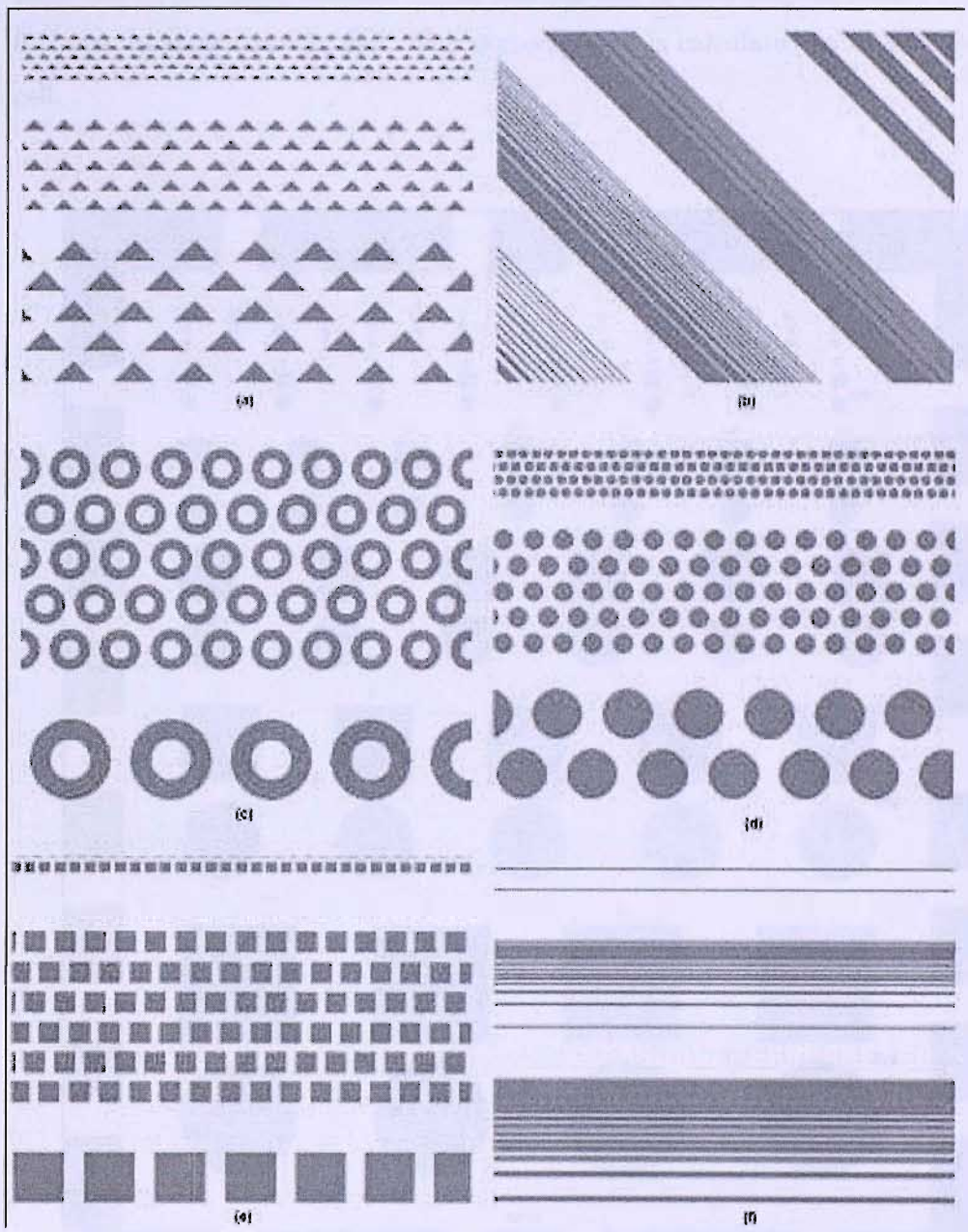

Figure B.2: *Structures of mask k989r: (a) triangles, (b) diagonal lines (c) rings, (d) circles, (e) squares, (f) horizontal lines*

B.2 Mask KA43M (reversed)

Each cell of this mask contains circles and squares of sizes varying from 1.5 mm to 0.1 mm, as shown in Fig. B.3. The exposing area is calculated to be 0.63 cm^2 per cell.

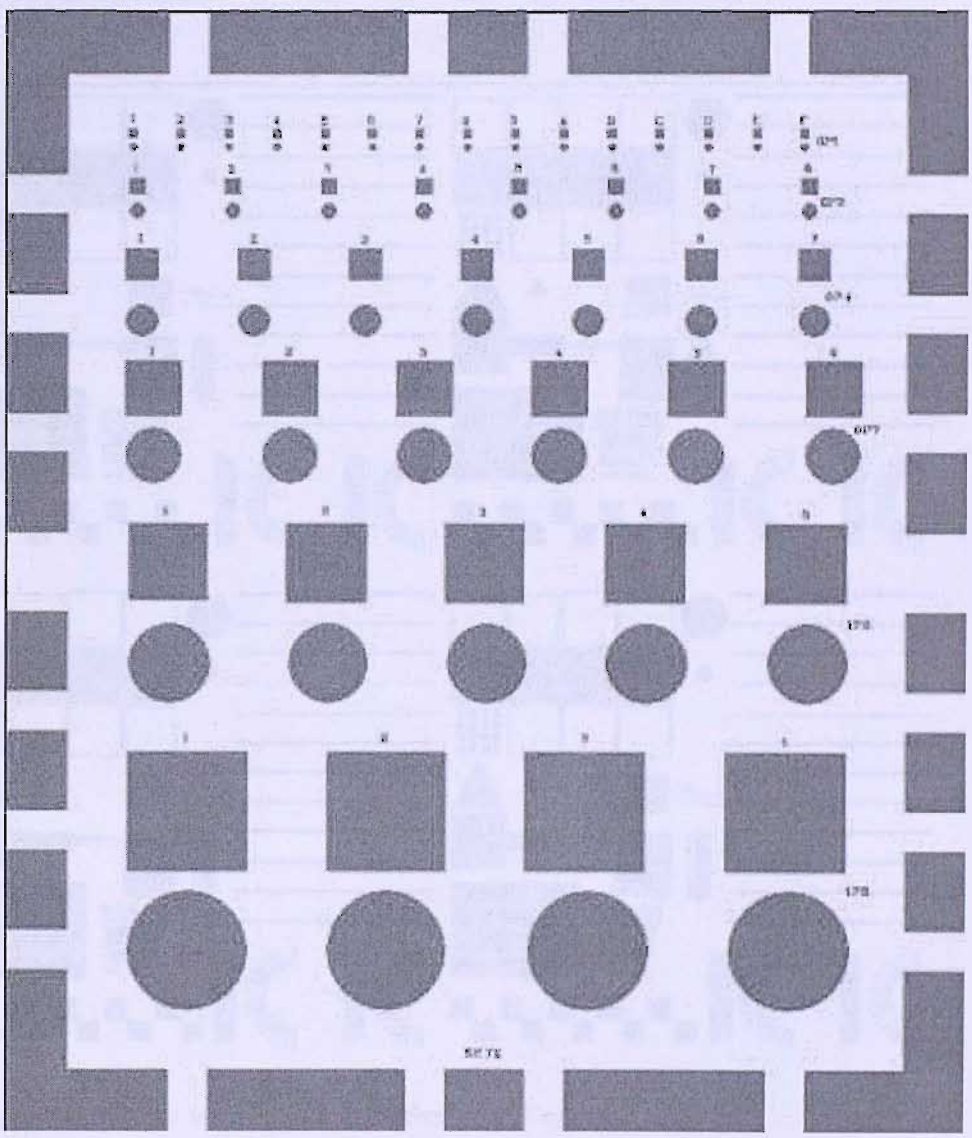

Figure B.3: *Cell of mask KA43M*

B.3 Mask KB73R (reticle)

This mask was specifically designed of latex spheres self assembly and magnetoresistance experiments. A top view of 1 cell is shown in Fig. B.4. The exposing area was calculated to be 0.03817 cm^2 per cell. The reticle consists of a 3x3 cell matrix and it is 5 times larger than the actual on-wafer dimensions. It has been specifically designed for the new STEPPER of INNOS. Fig. B.5 illustrates some specific mask parts.

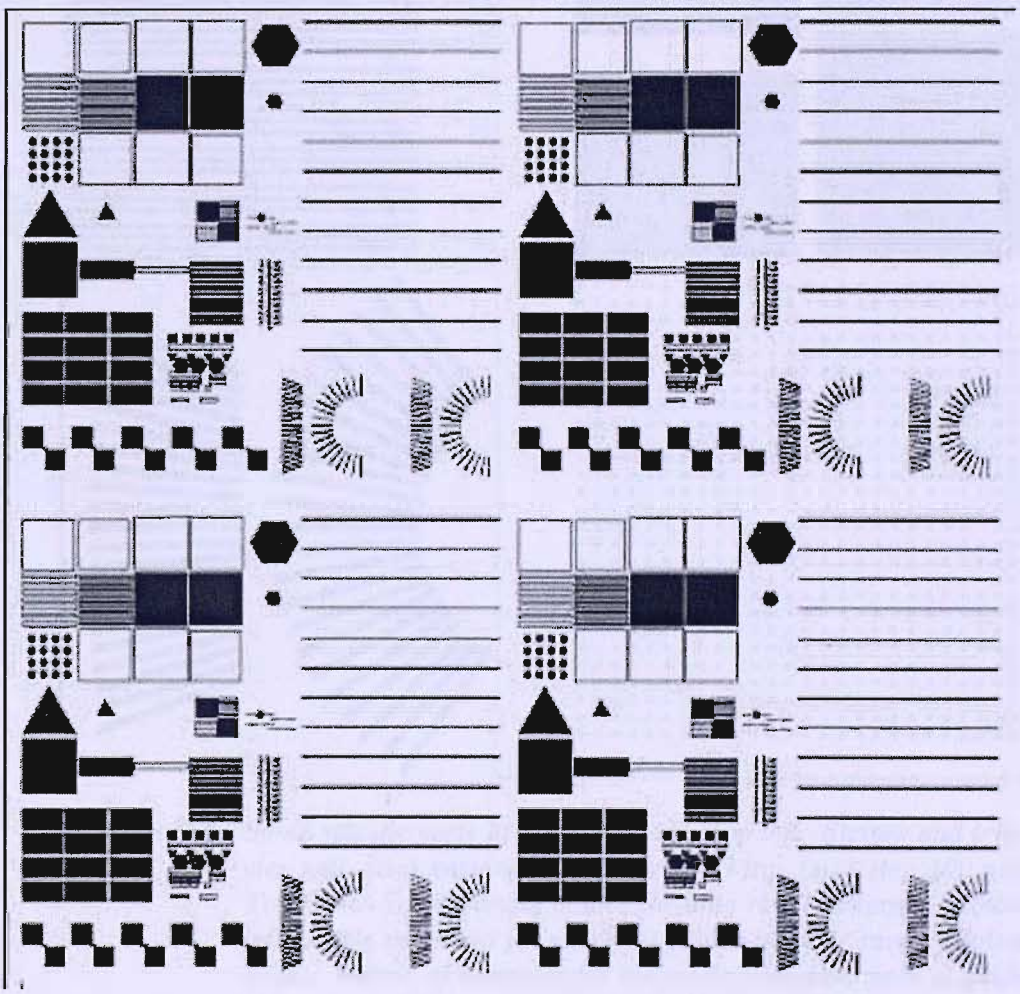

Figure B.4: *Top view of one cell (6x6 mm^2) of mask KB73R.*

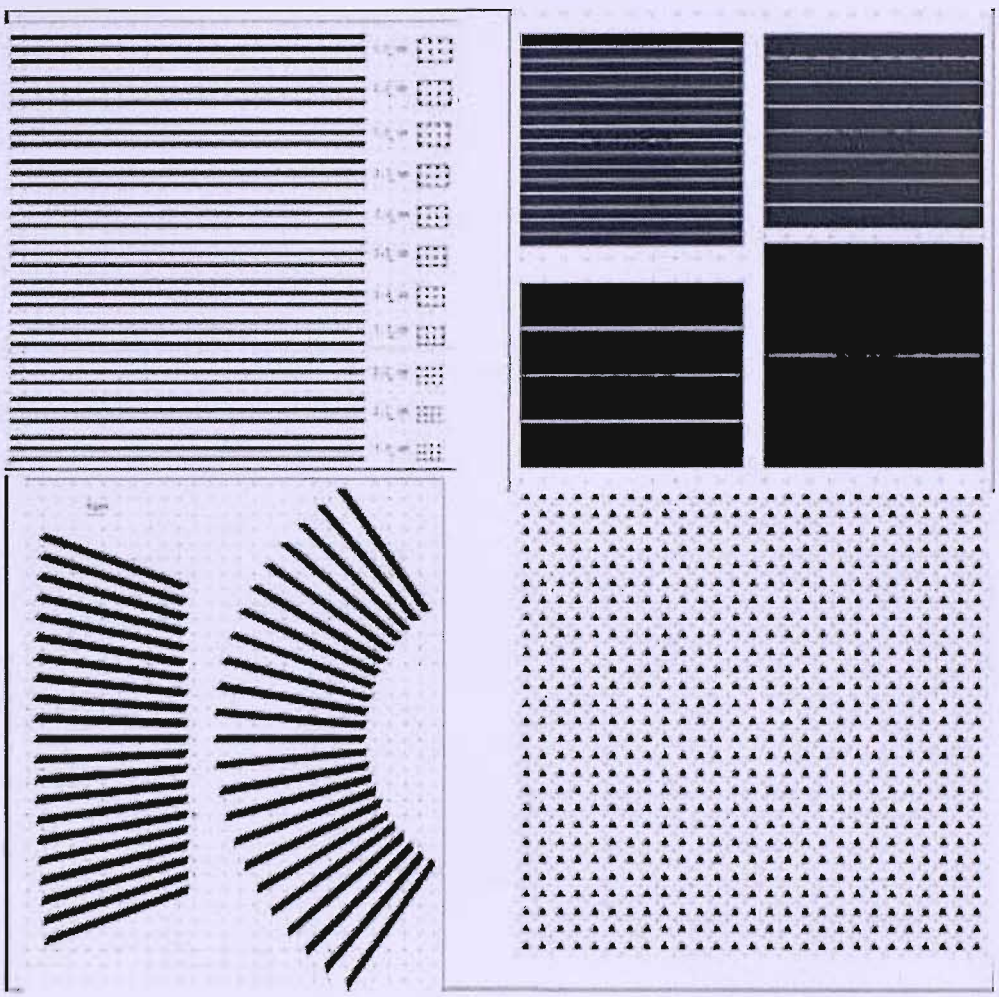

Figure B.5: *Some specific parts of mask KB73R. Top left: Stripes and triangles with sizes varying from 2 μm to 3 μm (size step 100 nm). Top right: Self assembly guides for long range ordering. Bottom left: Angle variation for checking guidance angle range. Bottom Right: Matrix of triangles for magnetic measurements of guided self - assembly.*